Sedimentology and Stratigraphy of the Shenandoah Formation, Western Fan, Jezero Crater, Mars

Kathryn M Stack, Libby R W Ives, Sanjeev Gupta, Michael P Lamb, Michelle Tebolt, Gwénaël Caravaca, John P Grotzinger, Patrick Russell, David L Shuster, Amy J Williams, et al.

JGR Planets

RESEARCH ARTICLE
10.1029/2023JE008187

Special Section:
The Perseverance Rover's Exploration of the Western Fan Front, Jezero Crater, Mars

Sedimentology and Stratigraphy of the Shenandoah Formation, Western Fan, Jezero Crater, Mars

K. M. Stack[1], L. R. W. Ives[1], S. Gupta[2], M. P. Lamb[3], M. Tebolt[1,4], G. Caravaca[5], J. P. Grotzinger[3], P. Russell[6], D. L. Shuster[7], A. J. Williams[8], H. Amundsen[9†], S. Alwmark[10], A. M. Annex[3,11], R. Barnes[2], J. Bell III[12], O. Beyssac[13], T. Bosak[14], L. S. Crumpler[15], E. Dehouck[16], S. J. Gwizd[1], K. Hickman-Lewis[17,18], B. H. N. Horgan[19], J. Hurowitz[20], H. Kalucha[3], O. Kanine[3], C. Lesh[1,6], J. Maki[1], N. Mangold[21], N. Randazzo[22], C. Seeger[3], R. M. E. Williams[23], A. Brown[24], E. Cardarelli[1,6], H. Dypvik[25], D. Flannery[26], J. Frydenvang[27], S.-E. Hamran[25], J. I. Núñez[28], D. Paige[6], J. I. Simon[29], M. Tice[30], C. Tate[31], and R. C. Wiens[19]

[1]Jet Propulsion Laboratory, California Institute of Technology, Pasadena, CA, USA, [2]Imperial College, London, UK, [3]Division of Geological and Planetary Sciences, California Institute of Technology, Pasadena, CA, USA, [4]Jackson School of Geosciences, University of Texas at Austin, Austin, TX, USA, [5]Institut de Recherche en Astrophysique et Planétologie (IRAP), UMR 5277 CNRS, UPS, CNES, Université Paul Sabatier Toulouse III, Toulouse, France, [6]UCLA, Los Angeles, CA, USA, [7]UC Berkeley, Berkeley, CA, USA, [8]Department of Geological Sciences, University of Florida, Gainesville, FL, USA, [9]Vestfonna Geophysical, Kabelvåg, Norway, [10]Department of Geology, Lund University, Lund, Sweden, [11]Morton K. Blaustein Department of Earth & Planetary Sciences, Johns Hopkins University, Baltimore, MD, USA, [12]Arizona State University, Tempe, AZ, USA, [13]Institute de Minéralogie, de Physique des Matériaux et de Cosmochimie, CNRS, Sorbonne Université, Muséum National d'Histoire Naturelle, Paris, France, [14]Massachusetts Institute of Technology, Cambridge, MA, USA, [15]New Mexico Museum of Natural History and Science, Albuquerque, NM, USA, [16]Université Lyon, UCBL, ENSL, UJM, CNRS, LGL-TPE, Villeurbanne, France, [17]Natural History Museum, London, UK, [18]Dipartimento di Scienze Biologiche, Geologiche e Ambientali, Università di Bologna, Bologna, Italy, [19]Purdue University, West Lafayette, IN, USA, [20]Stony Brook University, Stony Brook, NY, USA, [21]Laboratoire Planétologie et Géodynamique, Centrel National de Recherches Scientifiques, Université Nantes, Université Angers, Unité Mixte de Recherche 6112, Nantes, France, [22]University of Alberta, Edmonton, AB, Canada, [23]Planetary Science Insitute, Tucson, AZ, USA, [24]Plancius Research, Severna Park, MD, USA, [25]University of Oslo, Oslo, Norway, [26]School of Earth and Atmospheric Sciences, Queensland University of Technology, Brisbane, QLD, Australia, [27]Copenhagen University, Copenhagen, Denmark, [28]Johns Hopkins University Applied Physics Laboratory, Laurel, MD, USA, [29]NASA Johnson Space Center, Houston, TX, USA, [30]Texas A&M, College Station, TX, USA, [31]Cornell University, Ithaca, NY, USA

†Deceased August 2023.

Key Points:

- The Shenandoah formation is a sand-dominated, clastic, sedimentary sequence comprising the lower 25 m of Jezero's western fan
- This sequence records the transition from an alluvial fan setting to a lacustrine setting, followed by progradation of a river delta
- This sequence records evidence for a warm, wet, habitable depositional setting with the potential to preserve biosignatures

Supporting Information:

Supporting Information may be found in the online version of this article.

Correspondence to:

K. M. Stack,
kathryn.m.stack@jpl.nasa.gov

Citation:

Stack, K. M., Ives, L. R. W., Gupta, S., Lamb, M. P., Tebolt, M., Caravaca, G., et al. (2024). Sedimentology and stratigraphy of the Shenandoah formation, western Fan, Jezero crater, Mars. *Journal of Geophysical Research: Planets*, *129*, e2023JE008187. https://doi.org/10.1029/2023JE008187

Received 31 OCT 2023
Accepted 26 JAN 2024

Abstract Sedimentary fans are key targets of exploration on Mars because they record the history of surface aqueous activity and habitability. The sedimentary fan extending from the Neretva Vallis breach of Jezero crater's western rim is one of the Mars 2020 Perseverance rover's main exploration targets. Perseverance spent ~250 sols exploring and collecting seven rock cores from the lower ~25 m of sedimentary rock exposed within the fan's eastern scarp, a sequence informally named the "Shenandoah" formation. This study describes the sedimentology and stratigraphy of the Shenandoah formation at two areas, "Cape Nukshak" and "Hawksbill Gap," including a characterization, interpretation, and depositional framework for the facies that comprise it. The five main facies of the Shenandoah formation include: laminated mudstone, laminated sandstone, low-angle cross stratified sandstone, thin-bedded granule sandstone, and thick-bedded granule-pebble sandstone and conglomerate. These facies are organized into three facies associations (FA): FA1, comprised of laminated and soft sediment-deformed sandstone interbedded with broad, unconfined coarser-grained granule and pebbly sandstone intervals; FA2, comprised predominantly of laterally extensive, soft-sediment deformed laminated, sulfate-bearing mudstone with lenses of low-angle cross-stratified and scoured sandstone; and FA3, comprised of dipping planar, thin-bedded sand-gravel couplets. The depositional model favored for the Shenandoah formation involves the transition from a sand-dominated distal alluvial fan setting (FA1) to a stable, widespread saline lake (FA2), followed by the progradation of a river delta system (FA3) into the lake basin. This sequence records the initiation of a relatively long-lived, habitable lacustrine and deltaic environment within Jezero crater.

Plain Language Summary Fan-shaped deposits are important exploration targets on Mars because they record the activity of water and conditions suitable for life on the surface. The Mars 2020 Perseverance rover has been exploring an ancient impact crater, named Jezero, since landing on Mars in February 2021. One of the rover's main exploration targets is a fan-shaped deposit of sedimentary rock extending into the crater from

the western rim. One Earth year into the rover's mission, Perseverance arrived at the eroded edge of this fan, exploring several outcrops of sedimentary rock, and collecting seven rock samples. This study uses images and data from Perseverance to describe these rocks, called the "Shenandoah" formation, and to determine how they formed. The oldest rocks of the Shenandoah formation contain sand and pebbles that were likely laid down at the edge of an alluvial fan. Next, very fine-grained rocks were deposited in a lake setting. Dipping layers of alternating sand and pebbles represent a change in the local setting and the growth of a delta into a relatively long-lived lake. The rover's observations of the Shenandoah formation show that past conditions in Jezero crater were capable of hosting and preserving signs of ancient life.

1. Introduction

Sedimentary rocks on Earth and Mars preserve the primary record of paleoclimate, surface processes and environments, and habitability, and at least on Earth, they form the principle archives of the ancient biosphere. With the recognition of a diverse and widespread sedimentary rock record exposed on the surface of Mars (e.g., Malin & Edgett, 2000), came an interest in the robotic exploration of these sites to further understand the evolution of Mars as a once-habitable planet. Orbiting spectrometers have observed the mineralogy of Mars' sedimentary rock record, confirming the dominant role of liquid water in modifying the surface and near subsurface (e.g., Bibring et al., 2005, 2006; Carter et al., 2013; Ehlmann & Edwards, 2014; Ehlmann et al., 2011; Gendrin et al., 2005; Mustard et al., 2008; Poulet et al., 2005). These instruments have also revealed spatial, temporal, and stratigraphic trends that hint at both global-scale and local-scale paleoclimate evolution (Bibring et al., 2006; Ehlmann & Edwards, 2014). High-resolution and color orbiter images have revealed the Mars sedimentary rock record in unprecedented detail, leading to the identification and analysis of ancient aeolian, fluvial, deltaic, and lacustrine environments across the planet (Grotzinger & Milliken, 2012; Malin & Edgett, 2000). Finally, on-ground surface exploration by rovers, particularly the Mars Exploration Rover Opportunity and the Mars Science Laboratory Curiosity rover, have enabled the detailed study of depositional, alteration, and diagenetic processes within Mars' sedimentary rock record and insights into the planet's climate and past habitability (Arvidson et al., 2011; Grotzinger et al., 2005, 2014, 2015; Lapôtre et al., 2022; McLennan et al., 2019; Squyres et al., 2004; Vasavada, 2022; Williams et al., 2013).

The Mars 2020 Perseverance rover mission (Farley et al., 2020), which launched from Earth in July 2020 and began surface operations on Mars in February 2021, is the first leg of a multi-mission, international Mars Sample Return effort whose objective is possible return of samples from Mars to Earth in the 2030s. Mission objectives of the Perseverance rover include characterizing the geology and habitability of its exploration area, seeking signs of ancient life, collecting a cache of scientifically compelling, return-worthy samples, and preparing for future human exploration of Mars (Farley et al., 2020). Perseverance's landing site and initial exploration area are within Jezero crater, a 45-km diameter crater located along the inner western rim of the ∼3.9-billion-year (Gyr)-old Isidis impact basin (Werner, 2008) (Figure 1). Jezero crater is estimated to have formed in the late Noachian period, ∼3.8 Gyr ago (Fassett & Head, 2008), and contains within it a sequence of igneous and sedimentary rocks including a well-preserved fan extending from Neretva Vallis's breach of the western rim of the crater (Ehlmann et al., 2008; Fassett & Head, 2005; Goudge et al., 2015, 2017, 2018; Schon et al., 2012) (Figures 1a and 1b). This fan has been interpreted both from orbiter and rover images as a river delta that formed in a Late Noachian-to-Early Hesperian-aged lake within the crater (Ehlmann et al., 2008; Fassett & Head, 2005; Goudge et al., 2015, 2017, 2018; Mangold et al., 2021; Schon et al., 2012).

Perseverance spent the first Earth year of its mission in Jezero crater exploring and sampling aqueously altered igneous rocks, including basalts and an older olivine cumulate, that comprise the present-day crater floor (Farley et al., 2022) (Figure 1c). In April 2022, Perseverance arrived at the base of the western fan and carried out a ∼250-sol (martian day) exploration campaign focused on the lower 25 m of outcrop, informally named the "Shenandoah" formation, exposed within the fan's easternmost erosional scarp (Figures 2 and 3). During this exploration campaign, Perseverance collected detailed image, geochemical, and mineralogical data of the Shenandoah formation, while also acquiring long distance context images of the remaining upper ∼30 m of the succession. Perseverance also collected subsurface data with its ground-penetrating radar instrument as it traversed from the crater floor into and over the Shenandoah formation. This data set contextualized a suite of seven

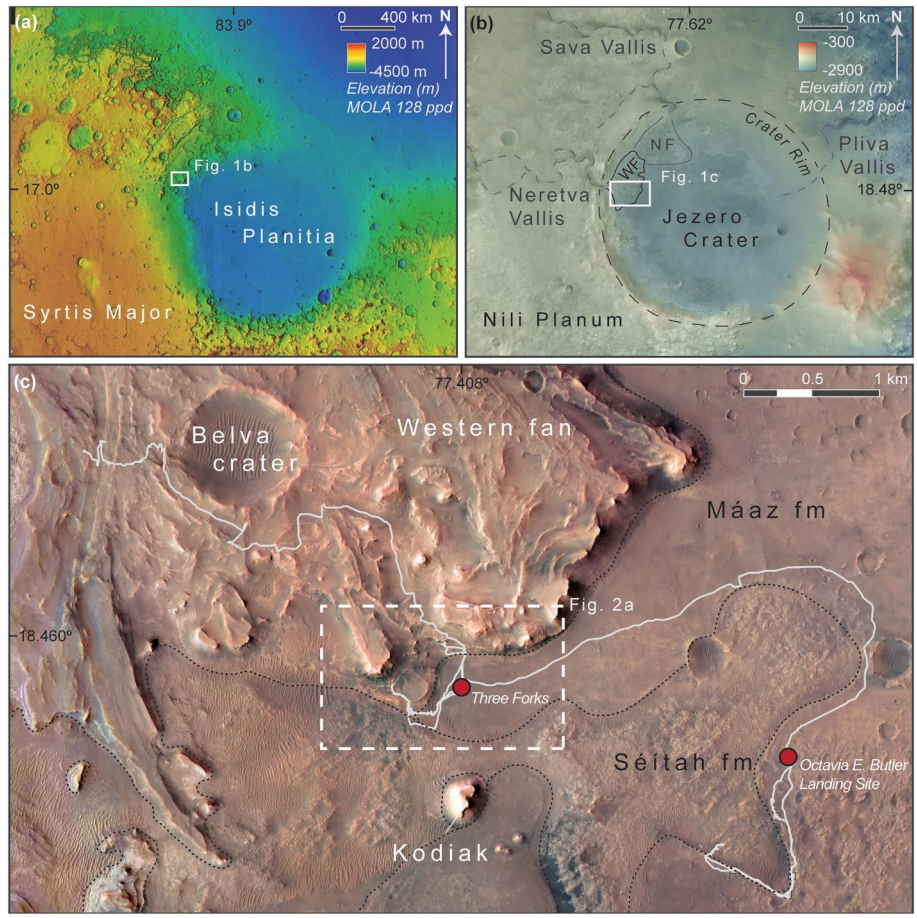

Figure 1. (a) Regional context of Jezero crater, the Mars 2020 Perseverance landing site and exploration area, shown on a Mars Orbiter Laser Altimeter (MOLA) topographic basemap. Isidis Planitia, lying within the Isidis impact basin, is adjacent to the overlying Syrtis Major igneous province. (b) MOLA topography overlain on a Context Camera (CTX) basemap of Jezero crater and surrounding Nili Planum region showing the location of the main inlet (Neretva and Sava) and outlet (Pliva) valleys, western fan (WF) and northern fan (NF) deposits, and crater rim and floor. (c) Perseverance's traverse (white line) in Jezero crater from the Octavia E. Butler Landing Site to the sol 879 rover position annotated on a High Resolution Imaging Science Experiment (HiRISE) orthophoto mosaic (Fergason et al., 2020a, 2020b). Perseverance's exploration of the Shenandoah formation and adjacent units is contained within the box showing the location of Figure 2a. Boundaries between the Séítah formation, Máaz formation, and the western fan are illustrated with a dotted black line. Noted are Octavia E. Butler Landing Site, Three Forks, the Kodiak fan remnant, and Belva crater.

rock samples, including three pairs and one single sample, along with two regolith samples (one pair) that were collected by Perseverance during this campaign (Farley & Stack, 2023).

This study describes the sedimentology and stratigraphy of the Shenandoah formation observed at and between two sections, "Cape Nukshak" and "Hawksbill Gap." We identify and describe the sedimentary facies that occur within these sections, interpreting depositional processes and setting. We also develop a depositional framework for the Shenandoah formation, providing context for Perseverance's first suite of sedimentary samples.

2. Geologic Setting and Mission Context

2.1. Sedimentary Fans in Jezero Crater

Jezero crater, located on the inner western rim of the Noachian-aged Isidis impact basin (Fassett & Head, 2005, 2008; Werner, 2008), is notable for the presence of two inlet valleys breaching its rim, Neretva Vallis to the west and Sava Vallis to the north, and an outlet valley, Pliva Vallis, which incises across its eastern rim. The presence of Pliva Vallis indicates that Jezero was once an overfilled lake basin (Fassett & Head, 2005) (Figure 1b). A

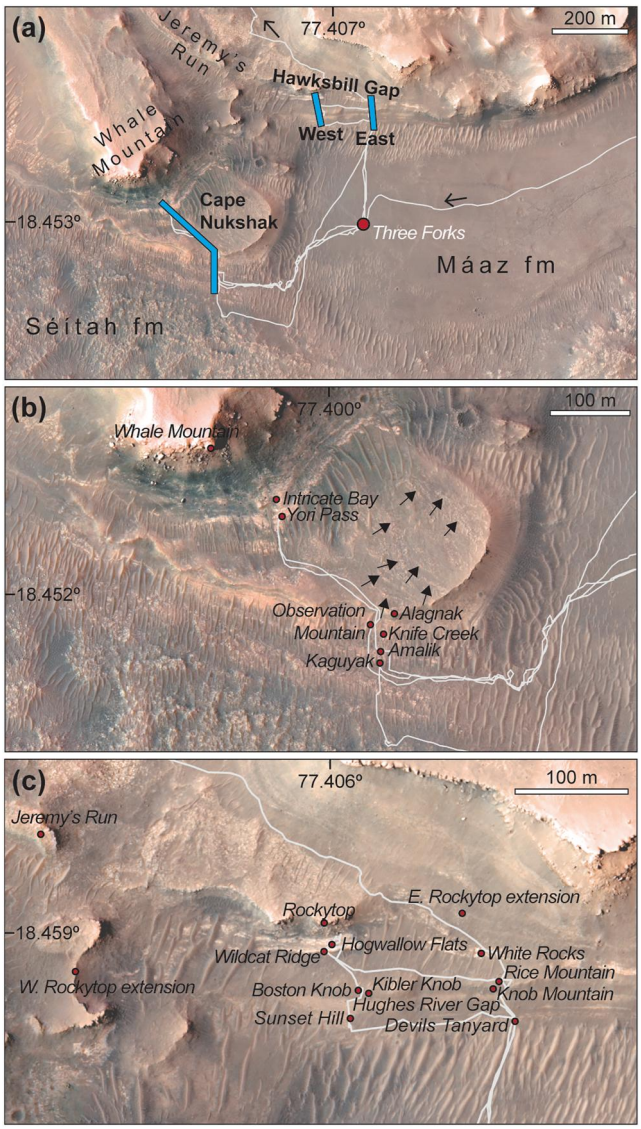

Figure 2. (a) The fan front explored by Perseverance between sols 410–709. The Cape Nukshak, Hawksbill Gap West, and Hawksbill Gap East sections of Figure 12 are annotated in yellow. Note that sections extend only up to the strata currently designated by the Mars 2020 Science Team as the Shenandoah formation. Terrains inferred to be the igneous Máaz and Séítah formation are noted, along with the Three Forks location. Whale Mountain and Jeremy's Run, outcrops north and higher in the section than the Shenandoah formation, are also annotated. Black arrows indicate the direction of Perseverance's traverse into and out of the fan front campaign. (b) Main outcrops visited or observed by Perseverance at Cape Nukshak including Kaguyak, Amalik, Knife Creek, Observation Mountain (aeolian bedform), Alagnak, Yori Pass, Intricate Bay, and Whale Mountain. Black arrows point to bedrock ridges on the top surface of the Cape Nukshak plateau. (c) Main outcrops visited or observed by Perseverance at Hawksbill Gap including Devils Tanyard, Hughes River Gap, Sunset Hill, Kibler Knob, Boston Knob, Hogwallow Flats, Wildcat Ridge, Rockytop, W. Rockytop extension, E. Rockytop extension, White Rocks, Rice Mountain, and Knob Mountain.

well-preserved sedimentary fan within Jezero extends into the crater from Neretva Vallis and a more degraded deposit located south of the Sava Vallis breach (Fassett & Head, 2005; Goudge et al., 2015; Jodhukupar et al., 2023) (Figure 1b).

The sedimentary fans within Jezero were first interpreted to represent fluvial and deltaic deposition into a crater-filling lake by Fassett and Head (2005) given the similarity in elevation between the fans and the Pliva Vallis outlet. A well-preserved, distributary network of cross-cutting ridges on the western fan surface inferred to be exhumed fluvial channels and layering exposed within the fan's erosional scarp enhanced the fluvio-deltaic interpretation (Ehlmann et al., 2008; Goudge et al., 2015, 2017, 2018; Schon et al., 2012). Curvilinear bed sets observed on the upper surface of the western fan have been interpreted as migrating point bar sequences within a meandering river (Ehlmann et al., 2008; Goudge et al., 2018; Schon et al., 2012). An alluvial fan origin for the western fan was rejected because the western fan does not exhibit a semi-conical shape, convex cross-profile, or high slopes typical of alluvial fans observed elsewhere on Earth and Mars (Schon et al., 2012). Both Schon et al. (2012) and Goudge et al. (2015) favored a delta plain setting characterized by fluvial distributary channels for the currently preserved western fan, inferring that delta front and prodelta sediments were deposited further out into the basin and have nearly entirely eroded away.

In a subsequent analysis, Goudge et al. (2017) used variably inclined strata measured from orbiter data along the scarp of the western fan to argue for the preservation of topset, foreset, and bottomset strata formed in delta plain, delta front, prodelta, and lacustrine settings. Goudge et al. (2018) further developed a depositional model for the formation of the western fan that involved initial progradation of a fluvial-deltaic system into a standing body of water, followed by relatively continuous lake level rise and backstepping of the system as the crater filled with water. Breach of the lake via the Pliva Vallis outlet and subsequent lake level fall would have led to a last episode of delta progradation. Erosion of the western fan over time would have exposed delta front foreset, prodelta, and lacustrine deposits within the present-day scarp of the western fan, while fluvial meandering and coastal avulsive channel deposits were interpreted on the upper surface of the fan (Goudge et al., 2018). The interval of the western fan interpreted by Goudge et al. (2017, 2018) as bottomset to foreset deltaic deposits includes the Shenandoah formation, which is below the fan strata interpreted by Goudge et al. (2018) as fluvial meandering and coastal avulsive channel deposits.

Images acquired early in the Mars 2020 mission by Perseverance's Mastcam-Z and SuperCam Remote MicroImager (RMI) cameras of an eroded fan remnant named "Kodiak" (Figure 1c) revealed stratal geometries consistent with at least two sets of topset, steep foreset, and bottomset strata (Mangold et al., 2021). This architecture was interpreted to represent the southward progradation of Gilbert-style deltas into an ancient lake during lake level fall (Mangold et al., 2021). The occurrence of these deposits at an elevation of −2,490 m, about 100 m below that of the Pliva Vallis outlet, indicates that these strata were deposited in a closed-system basin that had a minimum water depth of 10 m based on the thickness of the clinoform sequence (Mangold et al., 2021). Coarse-grained, boulder-rich deposits imaged in the upper fan scarp, stratigraphically above the level of the delta clinoforms, provided evidence for a transition from deltaic to higher-energy fluvial deposition (Mangold et al., 2021).

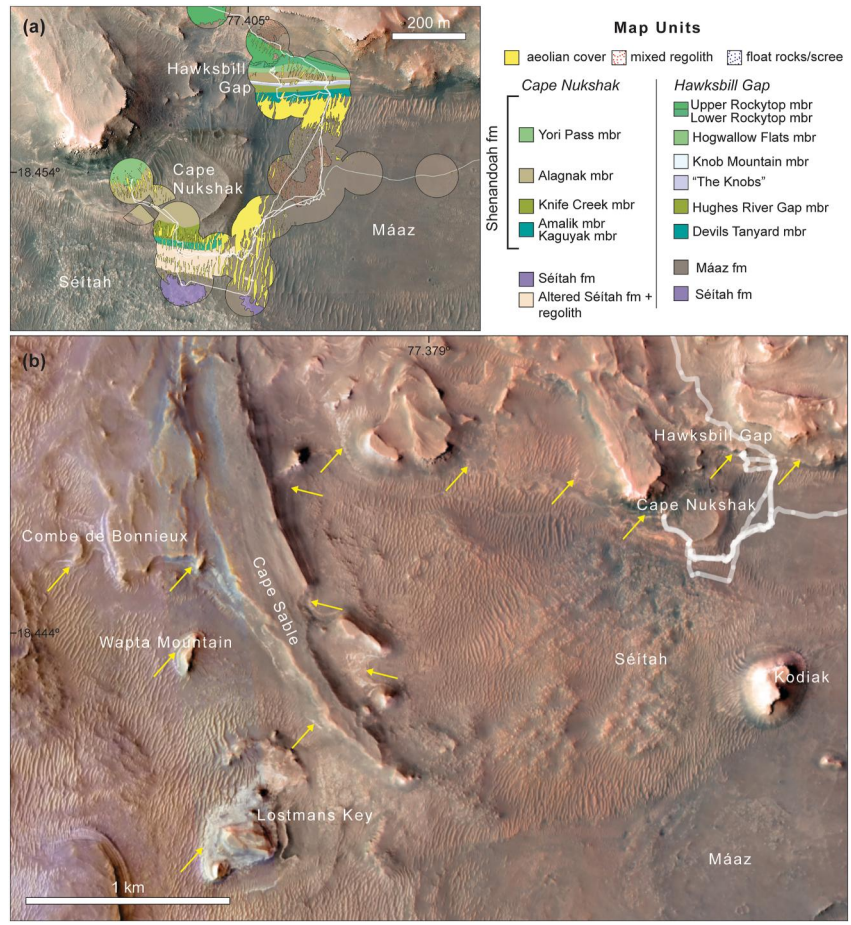

Figure 3. (a) Members of the Shenandoah formation at Cape Nukshak and Hawksbill Gap displayed on a color HiRISE basemap (Calef et al., 2013) using the geologic context mapping methods of Crumpler et al. (2023). (b) Light-toned outcrops similar to and traceable from Hogwallow Flats/Yori Pass-like extend east and west along the fan front (yellow arrows). White line denotes Perseverance's traverse.

Estimates of the duration of the aqueous activity in Jezero crater have varied considerably. Deposition of the fans was estimated initially by Fassett and Head (2005) to have taken between 10 and 10^3 years. However, Schon et al. (2012) used the presence of a stable delta plain environment, coupled with the extensive fill within the crater, to estimate that the Jezero lake system was active over 10^6–10^7 years. Salese et al. (2020) favored a shorter duration for fan formation—90–550 years at a minimum—not accounting for intermittency or evaporation, but suggested a longer duration for the breach and draining of the ancient Jezero lake. Lapôtre and Ielpi (2020) determined a minimum duration of 19–37 years for the construction of the fan, spanning across a total time period of ∼380,000 years, based on calculated channel lateral migration rates.

The absolute age and timing of fan formation within Jezero is not well constrained. Based on cross-cutting relationships between Hargraves crater ejecta and the distal reaches of the valley network feeding Jezero, Fassett and Head (2008) estimate a Late Noachian age (3.83–3.74 Gyr) for aqueous activity within Jezero. Mangold et al. (2020) questioned the relationship between the Jezero valley network and Hargraves ejecta, instead favoring a younger, early Hesperian age for the Jezero western fan and the river system feeding Jezero. An age of 3.6–3.2 Gyr was obtained from crater counts on the western fan (Mangold et al., 2020), and an early Hesperian age was further supported by morphological distinctions and volume estimates for the upper and lower reaches of the Neretva Vallis inlet channel. Mangold et al. (2020) proposed that formation of the western fan resulted from Hesperian-aged reactivation of the lower section of Neretva Vallis. Samples collected from the western fan and returned to Earth would resolve many of the questions about the timing and duration of aqueous activity within Jezero crater (Farley & Stack, 2023).

2.2. Perseverance Mission Narrative (Sols 410–700)

After touching down at Octavia E. Butler (OEB) landing site on the floor of Jezero crater, the Perseverance rover spent the first year of its surface mission exploring and sampling altered igneous rocks of the crater floor, including a series of basaltic lava flows, informally named the "Máaz" formation (Farley et al., 2022; Horgan, Udry, et al., 2023; Udry et al., 2023), that unconformably overlie an igneous olivine cumulate named the "Séítah" formation (Beyssac et al., 2023; Farley et al., 2022; Liu et al., 2021; Wiens et al., 2022) (Figure 1c). Following the successful completion of the Crater Floor Campaign (Sun et al., 2023), on sol 372, Perseverance embarked on a ∼5 km "rapid" traverse toward the eroded scarp of the western fan, so named because of the mission's priority to achieve maximum drive distance each sol. Perseverance arrived at the base of the western fan at a location named "Three Forks" on sol 410 (Figures 1c and 2a), officially beginning a science campaign to explore the eroded scarp of the western fan.

From Three Forks, Perseverance continued its traverse to the southwest, crossing the transition between regolith-covered Máaz formation and Séítah formation to the base of a promontory of the western fan named "Cape Nukshak" (Figures 2a and 2b). Perseverance had its first close encounter with clastic sedimentary rocks at the base of Cape Nukshak between sols 422–426, employing its remote sensing instruments to survey the "Kaguyak" and "Amalik" outcrops (Figure 2b). Perseverance then traversed ∼700 m northeast to an area of the western fan named "Hawksbill Gap" (Figures 2a and 2c). After encountering difficulties finding abradable or sampleable rock in the outcrop exposure at "Devils Tanyard," Perseverance traversed west, ascending the "Sunset Hill" exposure and passing by rocks at "Boston Knob" and "Kibler Knob" (Figure 2c). Perseverance then arrived at the base of an outcrop named "Hogwallow Flats" on sol 461 (Figure 2c). Perseverance remained in the vicinity of Hogwallow Flats until sol 535, acquiring a pair of samples at the base of the "Rockytop" outcrop (Swift Run and Skyland) and another pair at the "Wildcat Ridge" outcrop ("Hazeltop" and "Bearwallow") of Hogwallow Flats. A witness tube, one of five such tubes carried by Perseverance designed to record the contamination state within the adaptive caching assembly at the time of concurrent sample collection (Farley et al., 2022), was also sealed. The rover team then commanded Perseverance to return to Cape Nukshak to sample at Amalik. A pair of samples ("Shuyak" and "Mageik") and another witness tube were acquired at Amalik, but challenges sealing the Mageik sample tube led the team to drive Perseverance further up-section while awaiting completion of tube sealing activities. Perseverance traversed through the "Knife Creek" interval and "Alagnak" outcrops, on sol 606 arriving at "Yori Pass," the apparent lateral equivalent of Hogwallow Flats at Hawksbill Gap (Figures 2b and 3a). While at Yori Pass, Perseverance collected a single sample "Kukaklek," before driving downsection to a meter-scale aeolian ripple named "Observation Mountain," where a pair of regolith samples ("Atmo Mountain" and "Crosswind Lake") was collected. Perseverance then drove back to Three Forks, where it began the construction of a sample depot containing 10 samples on sol 652. Following the completion of sample depot construction activities on sol 693, Perseverance began its re-ascent of Hawksbill Gap, marking the official end of the Fan Front Campaign, and the beginning of the Uupper Fan Campaign, upon passing north of the Rockytop outcrop on sol 709 (Figures 1c and 2c).

3. Data and Methods

3.1. Naming Convention

Prior to Perseverance's landing in Jezero crater, the Mars 2020 Science Team divided the landing area into 1.2 km by 1.2 km quadrangles, each given an informal name inspired by an Earth-based national park or preserve (Stack et al., 2020). Perseverance explored the Shenandoah formation in two quadrangles: "Katmai" named for Katmai National Park and Preserve located in southern Alaska, and "Shenandoah" named for Shenandoah National Park in the Blue Ridge Mountains of Virginia. While the rover was in each quadrangle, respectively, the Science Team named areas, outcrops, rocks, and instrument targets after place names (e.g., cities, lakes, rivers, mountains, trails, and notable landmarks) located in and around these national parks on Earth. These names were then used to designate formation and member names for the rocks explored on Mars, often using the type-example rock or target name as the inspiration for the member name. Thus, some names are used for a particular outcrop or area explored by the rover, as well as the associated member of the stratigraphic succession (e.g., Hogwallow Flats outcrop and Hogwallow Flats member). These names are informal and have not been recognized by the International Astronomical Union, but follow similar informal naming conventions adopted by the Mars Science Laboratory Curiosity rover mission (Vasavada et al., 2014) and previous Mars surface missions.

3.2. Perseverance Rover Instruments and Data

The sedimentary facies of the Shenandoah formation were characterized using image data from Perseverance's Navigation cameras (Navcam, Maki et al., 2020), Mast Camera Zoom (Mastcam-Z, Bell et al., 2021), SuperCam's Remote Micro-Imager (RMI, Maurice et al., 2021), and the Scanning Habitable Environments with Raman and Luminescence for Organics and Chemicals (SHERLOC) Wide Angle Telegraphic Sensor for Operations and eNgineering (WATSON) and Autofocus Context Imager (ACI) cameras (Bhartia et al., 2021). The Navcam, Mastcam-Z and SuperCam RMI cameras are located on the rover's Remote Sensing Mast at a height ∼2 m above the surface and the SHERLOC WATSON and ACI cameras are mounted on the rover's robotic arm.

Stereo meshes derived from Navcam images were used to measure the cm- to m-scale dimensions of individual outcrops and to aid in the placement and sizing of scale bars in Mastcam-Z images. Image frames and mosaics from Mastcam-Z were used for geologic and stratigraphic context, as well as outcrop-scale characterization, including bed thickness and geometry, sedimentary bedform identification, and vertical and lateral facies relationships. Grain size characterization for coarser-grained rocks was possible with Mastcam-Z, which can resolve <1 mm-sized features in the nearfield and features ∼3 cm across at a distance of about 100 m (Bell et al., 2021). Mastcam-Z images were white-balanced, contrast stretched, and gamma-corrected to improve viewability (Bell et al., 2021). SuperCam's RMI is a high-resolution, color, telescopic imager with a small field of view (18.8 microradians) capable of resolving features between 160 (fine sand) and 560 (coarse sand) μm in its typical observing range between 2 and 7 m from the rover's mast (Maurice et al., 2021). In addition to imaging targets in the immediate area around the rover, RMI was used to acquire multi-frame mosaics of long-distance targets (e.g., Mangold et al., 2021). RMI images used in this study were processed with a Gaussian stretch to enhance the colors. WATSON, a copy of the Mars Science Laboratory Curiosity rover's MAHLI Camera (Edgett et al., 2012), is a color camera that operates at working distances between 1.8 cm and infinity (Bhartia et al., 2021). Pixel scales from WATSON range from 13.3 μm/pixel at a 1.8 cm working distance to 17.7 μm/pixel at 3 cm, 31 μm/pixel at 6.6 cm, and 100 μm/pixel at 25.5 cm range (Bhartia et al., 2021). Typical closest range images had pixel scales between 16 and 18 μm/pixel, allowing resolution of silt-sized grains under favorable viewing conditions (Bhartia et al., 2021; Weitz et al., 2018; Yingst et al., 2016). SHERLOC's ACI camera operates at a standoff distance from the surface of ∼50 μm and achieves a pixel scale of 10.1 μm/pixel, allowing the resolution of features ∼30 μm (silt) (Bhartia et al., 2021).

The Radar Imager for Mars' Subsurface Experiment (RIMFAX) antenna is located at the back of the rover, ∼60 cm from the ground (Hamran et al., 2020). RIMFAX is a ground-penetrating radar with a frequency range between 150 and 1,200 MHz that is operated in surface, shallow, and deep modes, both while stationary and during rover drives. Subsurface structure beneath the rover is imaged to depths of at least 10 m (Hamran et al., 2020). Two way travel time and depth as a function of rover traverse distance from RIMFAX were used to determine relationships between stratigraphic formations and members via the identification and tracing of prominent radar reflectors and their correlation with known units at the surface. Decimeter- to meter-scale structures observed in RIMFAX data internal to the sedimentary sequence were also used to inform depositional process and setting.

3.3. Lithologic Characterization and Stratigraphic Analysis

Qualitative estimates of lamination thickness (e.g., mm-scale or cm-scale) were derived from non-stereo Mastcam-Z images whose scale was determined with the aid of Navcam stereo meshes. For outcrops imaged by SuperCam RMI, more quantitative lamination thickness measurements were possible (Figures S1–S5, Table S1 in Supporting Information S1). An effort made to use images offering perpendicular or near-perpendicular viewing geometries of outcrop exposures for which an assumption of horizontal bedding orientation was reasonable (e.g., Figures 8b and 9b; Figures S1–S5, Table S1 in Supporting Information S1). Grain size was measured in SuperCam's RMI images when grains were coarse enough to resolve, and in grayscale, flat-fielded, contrast-enhanced SHERLOC ACI focus merge products or WATSON images for abraded and natural surface targets (Figures S6–S13, Table S2 in Supporting Information S1). Grains measured in Supercam RMI were usually scarce enough, or rock exposure limited enough, that a grid-based point count method could not be used. Instead, individual long-axis measurements were made for visible grains using the ImageJ program (Schneider et al., 2012), and grains were categorized via the grain size scale of Wentworth (1922) and Lazar et al. (2015). For

rock targets imaged by the SHERLOC ACI whose grain size is at or below the spatial resolution of the camera (i.e., comprised predominantly of fine and very fine sand and finer grains), a modified grid method was used in ImageJ whereby the most confidently resolved grain near each grid intersection was measured, with the major axis of an ellipse fitted to the outline of the grain reported as the grain diameter. As such, grain size measurements were biased toward larger grains and those with the highest tonal contrast. Shape, rounding, and sorting were classified for resolvable grains using the schemes of Blatt et al. (1972), Powers (1953), Harrel (1984), and Lazar et al. (2015), respectively.

Vertical stratigraphic columns were constructed at three places along the Shenandoah formation exposure explored by Perseverance, coinciding generally with the rover's main traverse routes up and down the succession (Cape Nukshak, Hawksbill Gap West, Hawksbill Gap East) (Figure 2a). Key outcrops and facies observed by the rover were localized on a High Resolution Imaging Science Experiment (HiRISE, McEwen et al., 2007) basemap of the exploration area (Fergason et al., 2020a, 2020b), and the thickness, dimensions, and vertical elevation ranges of each exposed facies or outcrop location were extracted from a HiRISE digital elevation model (Fergason et al., 2020a, 2020c) and verified with rover stereo Navcam mosaics (Maki et al., 2020) to construct vertical profiles through the stratigraphy.

4. Subsurface Context of the Shenandoah Formation

Figures 4 and 5 show RIMFAX radargrams constructed from radar soundings acquired during the rover's traverse across the Hawksbill Gap and Cape Nukshak sections. The Cape Nukshak radargram reveals a distinct change in reflection pattern and a dominant reflector that corresponds at the surface to the transition between igneous rocks of the Séítah formation and sedimentary clastic rocks of the Shenandoah formation (Figure 4). In the subsurface, the Séítah-Shenandoah contact appears to dip to the north before flattening out, revealing at least ∼10 m of antecedent topography along this contact (Paige et al., 2024) (Figure 4d). Radar reflections within the Shenandoah formation appear horizontal to subhorizontal and appear to terminate against the underlying Séítah formation contact in an onlap relationship (Figure 4d). The presence of these onlapping layers in the subsurface reveals that a sedimentary sequence at least 10 m thick was deposited prior to the lowermost exposure of Shenandoah formation observed by Perseverance at the surface (Figure 4d). There is no sign of the Máaz formation in this radar profile (Figure 4), which overlies the Séítah formation in other parts of the crater floor (Farley et al., 2022). Within the Shenandoah formation sequence at Cape Nukshak, subtle concave up structures between ∼2 and 4 m in width can be distinguished (Figure 4d).

Radargrams of the Hawksbill Gap section show distinct reflectors between the Séítah formation and the base of the Shenandoah formation section (Figure 5). The low reflectivity interval between the upper Séítah contact and the Shenandoah basal reflector is inferred to be the Máaz formation (Paige et al., 2024) (Figure 5). The Séítah, Máaz, and Shenandoah formation contacts at Hawksbill Gap, unlike at Cape Nukshak, appear horizontal to subhorizontal (Figure 5). A series of m-scale, north-dipping reflectors are observed within the basal subsurface projection of the Shenandoah formation and could represent cross-bedding and/or barform geometries (Figure 5). Several prominent horizontal reflectors are observed within the Shenandoah sequence, including decimeter-scale concave-up features, similar to those observed in the subsurface at Cape Nukshak (Figures 5c and 5d).

5. Sedimentary Lithofacies of the Shenandoah Formation

The sedimentary rock types observed within the Shenandoah formation can be classified as one of five lithofacies distinguished on the basis of grain size, bed thickness and geometry, and sedimentary structures (Figures 6–11, Table 1). Diagenetic textures and mineralogy with unique or defining characteristics were also used to characterize facies. Lithofacies descriptions, presented in order of increasing grain size in this section, are followed by an outcrop-by-outcrop review of the sedimentary successions observed at Cape Nukshak and Hawksbill Gap in Section 6. To describe these successions, we use the previously-defined lithofacies as the basis for outcrop characterization and the definition of stratigraphic members in which these facies occur (Section 6 and Tables 2 and 3). In Section 7, the lithofacies are used together with their stratigraphic context to define facies associations for which depositional processes and settings are interpreted.

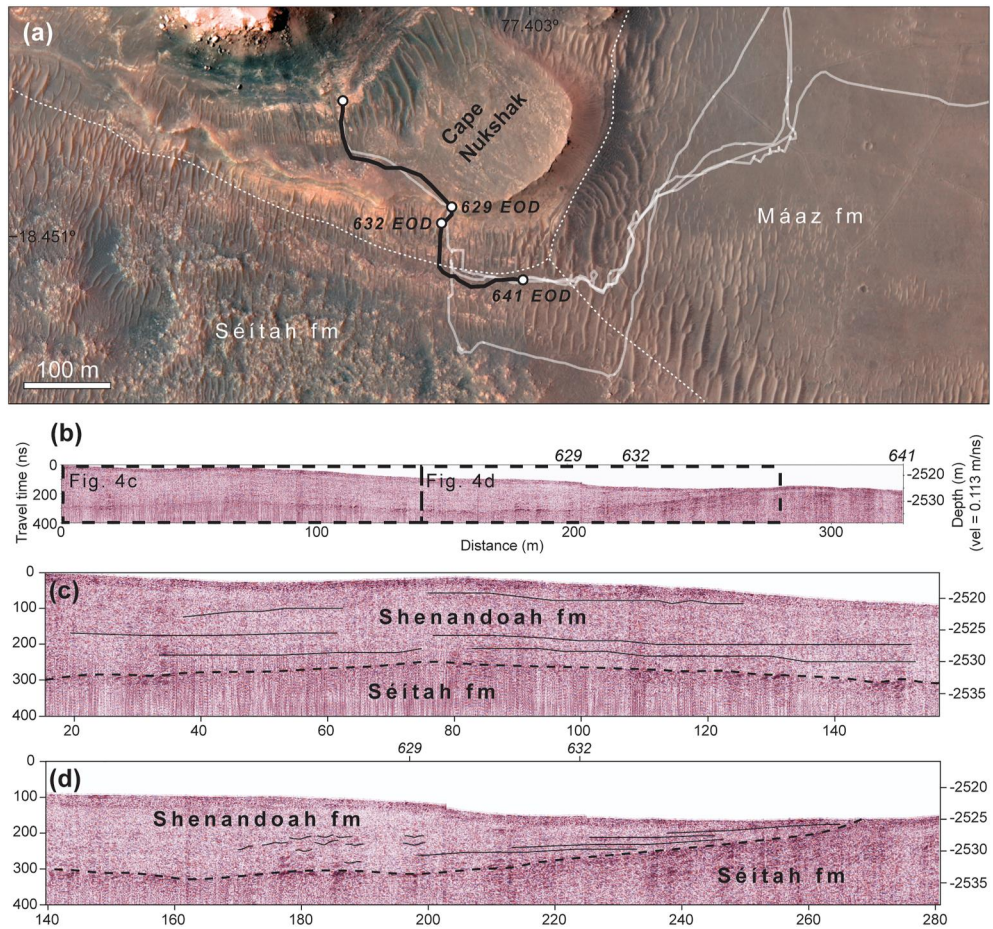

Figure 4. RIMFAX radargram showing two-way travel time and depth as a function of distance constructed from soundings acquired on sols 629, 632, and 641 during the traverse of Cape Nukshak. (a) Drive path for sols 629, 632, and 641 along which the radargram in (b) was collected. The solid white line represents that rover's traverse through the area; the dotted white line marks the contacts between the Séítah formation, Máaz formation, and Shenandoah formations. (c) Zoom-in on horizontal strata within the Shenandoah formation overlying a distinct reflector that represents the Shenandoah-Séítah formation contact. (d) Zoom-in on the Shenandoah-Séítah formation contact. Reflectors representing strata within the Shenandoah formation are observed to onlap the dipping Shenandoah-Séítah contact. Subtle m-scale concave up structures occur in the subsurface within the Shenandoah formation.

5.1. Laminated Mudstone (M_l)

The laminated mudstone facies is characterized predominately by plane parallel, mm-scale laminations (Figure 6). Laminations are sometimes subtly expressed (Figure 6c), likely the result of diagenetic overprinting and the effects of cementation, resulting in apparently structureless intervals that can usually be traced laterally into parallel laminated beds (Figure 6a). Laminations are typically between ~1 to several mm thick (Figure 6c; Figure S1, Table S1 in Supporting Information S1). Neither ripple cross-laminations, dune cross-stratification, nor low-angle truncation surfaces have been observed within this facies. The plane parallel laminations exhibit lateral and vertical contacts with deformed laminations of the same lithology (Figures 7a and 7b). Deformation includes small folds (Figure 7a) and fluid escape structures (Figure 7b).

Resolvable grains observed in SHERLOC ACI images of abraded or non-coated natural surfaces at the Pignut Mountain, Berry Hollow, Amalik, and Uganik Island targets have average diameters (long axis) in the coarse silt to very fine sand range (between ~70 and 100 μm) (Figures 6e and 6f; Table S2 in Supporting Information S1). The largest grains observed are in the coarse sand range, although these are rare. Resolvable grains exhibit moderate to high sphericity and are subrounded to well-rounded (Figure 6). A substantial proportion (>50%–

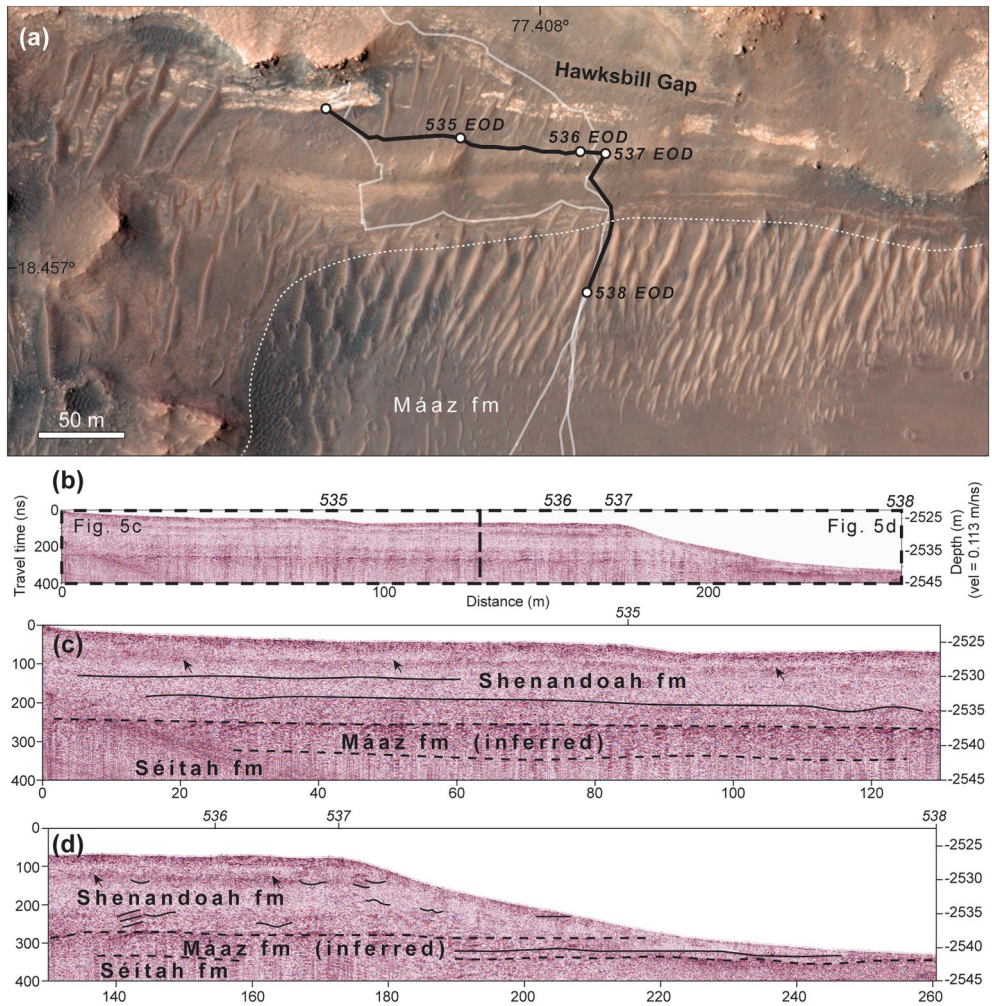

Figure 5. RIMFAX radargram showing two-way travel time and depth as a function of distance constructed from soundings acquired on sols 535, 536, 537, and 538 during Perseverance's east- and southward traverse from the Shenandoah formation onto the inferred Máaz formation at Hawksbill Gap. (a) Drive path for sols 535–538 along which the radargram in (b) was collected. The solid white line represents the rover's traverse through the area; the dotted white line marks the contacts between the Máaz and Shenandoah formations. Pronounced dipping events recorded between 0 and 40 m distance are caused by radio waves propagating in the air and reflecting off the overlying escarpment. (c) Zoom-in on horizontal strata within the Shenandoah formation overlying reflections representing the subsurface Máaz and Séítah formation contacts. Black arrows in (c) and (d) point to a distinct horizon in the subsurface that correlates with the elevation of the "Knobs." (d) Zoom-in on the contact between the Shenandoah and inferred Máaz formations. Strata within the Shenandoah formation at Hawksbill Gap are generally horizontal with some subtle concave-up structure within the subsurface.

75%) of these rocks are made up of grains that are not resolvable in the rover's highest resolution images, and are likely coarse silt-sized and finer.

This facies contains ~10–30 wt% hydrated Fe/Mg sulfate within its clastic portion as observed by PIXL (Hurowitz et al., 2023), SuperCam LIBS (Dehouck et al., 2023), and SHERLOC (Farley & Stack, 2023). Diagenetic features including Ca-sulfate veins and veinlets (<1 mm thick), irregularly-shaped, mm-scale blebs of Ca-sulfate (Lopez-Reyes et al., 2023; Nachon et al., 2023; Roppel et al., 2023), and concretions measuring mm- to several cm in diameter (Broz et al., 2023) occur throughout this facies. Most concretions are spherical, with larger concretions exhibiting internal concentric layering when exposed in cross-section (Figure 6d). There is no conclusive evidence for deformation of laminations around the concretions, so they are interpreted to have formed after the sediments were already lithified. The distribution and diversity of diagenetic textures within this facies is noteworthy since such features are rare throughout the rest of the Shenandoah formation.

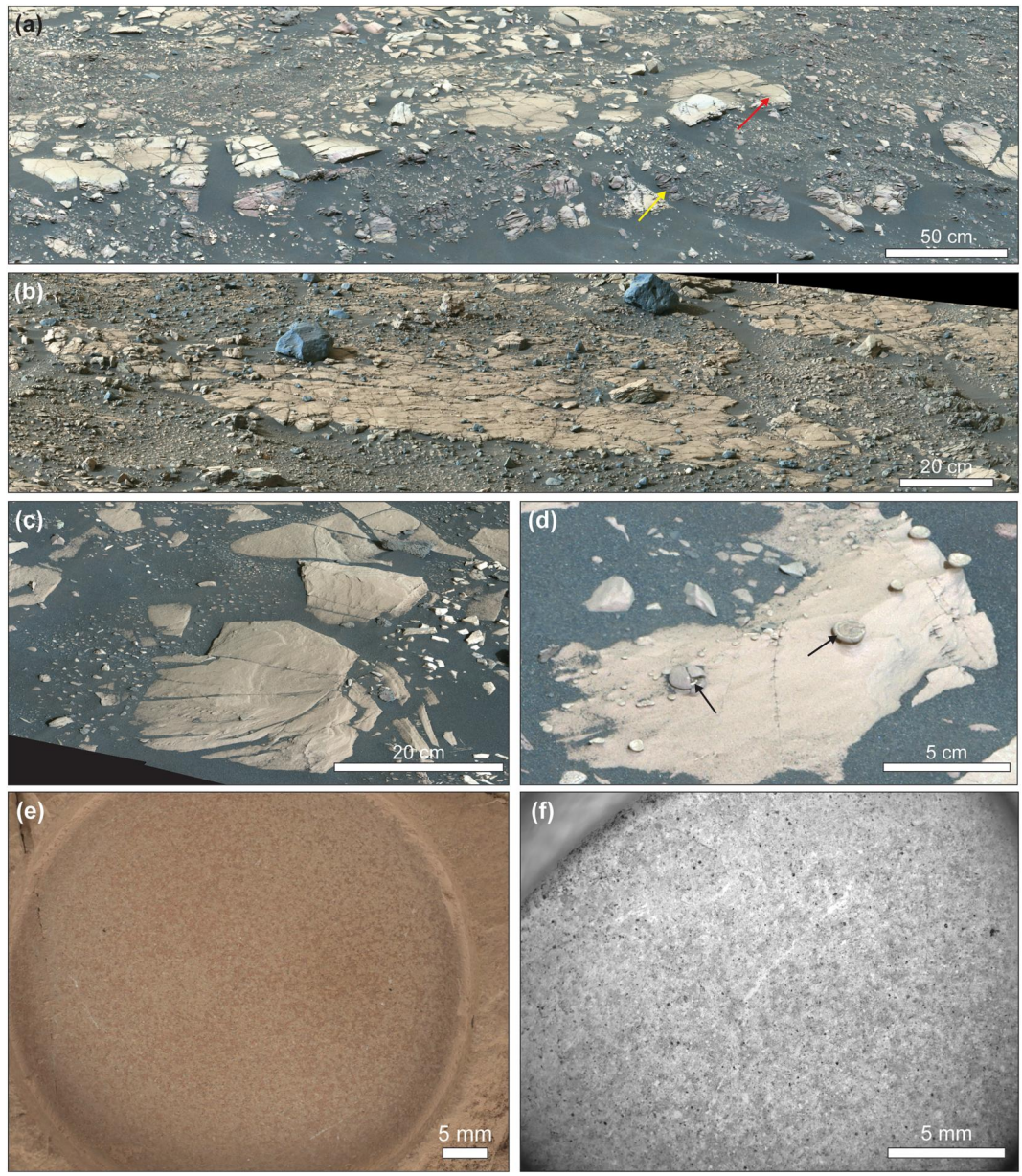

Figure 6. Laminated mudstone (M_l) facies. (a) Laminated mudstone at the base of the Hogwallow Flats outcrop observed in the "Smith Mountain" Mastcam-Z 110 mm mosaic acquired on sol 461 during rover sequence zcam08482. Yellow arrow points to purple laminations; red arrow points to tan, apparently massive outcrop with laminations visible on its eroded edge. (b) Laminated mudstone at the Yori Pass outcrop within the Mastcam-Z 110 mm mosaic acquired on sols 606 and 607 (zcam08616). (c) Planar, parallel laminations at the Hogwallow Flats outcrop within an Mastcam-Z 110 mm mosaic acquired on sol 467 (zcam08488). (d) Concentric concretions in the laminated mudstone facies at Hogwallow Flats within an Mastcam-Z 110 mm mosaic acquired on sol 467 (zcam08488). Black arrows point to concretions with bright white interior layers, presumed to be Ca-sulfate. (e) WATSON 7 cm standoff of the Berry Hollow abrasion acquired on sol 504. (f) SHERLOC ACI of the Berry Hollow abrasion acquired on sol 513.

5.2. Laminated Sandstone (S_l)

This facies is characterized by mm-scale plane parallel laminations (Figure 8; Figure S2, Table S1 in Supporting Information S1), although deformed layering is common (Figures 7c–7f). The rare mm-scale concretions observed in this facies do not appear to deform surrounding laminations (Figure 8b), so likely formed after initial sediment lithification. Weathered outcrops show a subtle decrease in competence (resistance to erosion) within individual laminations, which is a phenomenon consistent with normal grading (Figure 8d). This facies consists of

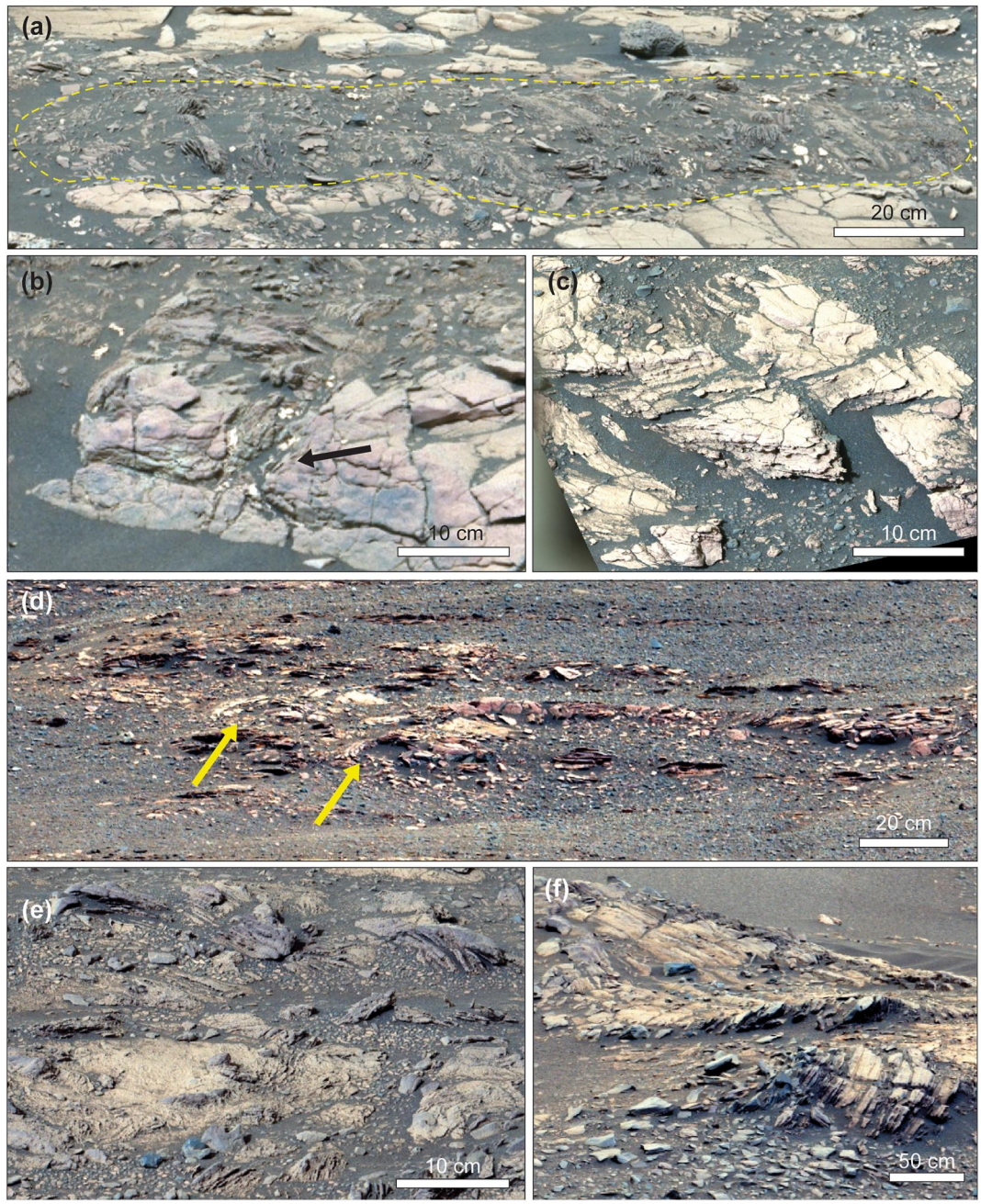

Figure 7. Deformation in the laminated mudstone (M_l) and laminated sandstone (S_l) facies. (a) Deformed laminations within laminated mudstones of the Hogwallow Flats member and (b) possible dewatering structure in the Hogwallow Flats within the Smith Mountain Mastcam-Z 110 mm mosaic (zcam08482) acquired on sol 461. (c) Z-shaped deformation structure at the "Brown Mountain" target in the Hughes River Gap member in a Mastcam-Z 63 mm mosaic (zcam08471) acquired on sol 456. (d) Circular deformation features in laminated sandstones of the Devils Tanyard member in a Mastcam-Z 110 mm mosaic (zcam08457) acquired on sol 439. (e) Deformed laminated sandstone at the "Trident Volcano" target near the transition between the Amalik and Knife Creek members at Cape Nukshak in a Mastcam-Z 110 mm mosaic (zcam08585) acquired on sol 565. (f) Steeply-dipping, deformed laminations at the base of the Knife Creek member at Cape Nukshak in a Mastcam-Z 110 mm mosaic (zcam08603) acquired on sol 588.

moderately to well-sorted, very fine- to very coarse-grained sandstone (Figure 8; Table S2 in Supporting Information S1). The partial "Rose River Falls" abrasion shows a population of white, gray, and black grains set in a reddish-brown ground mass/matrix below the resolution of the WATSON camera (Figure 8e). Most resolvable

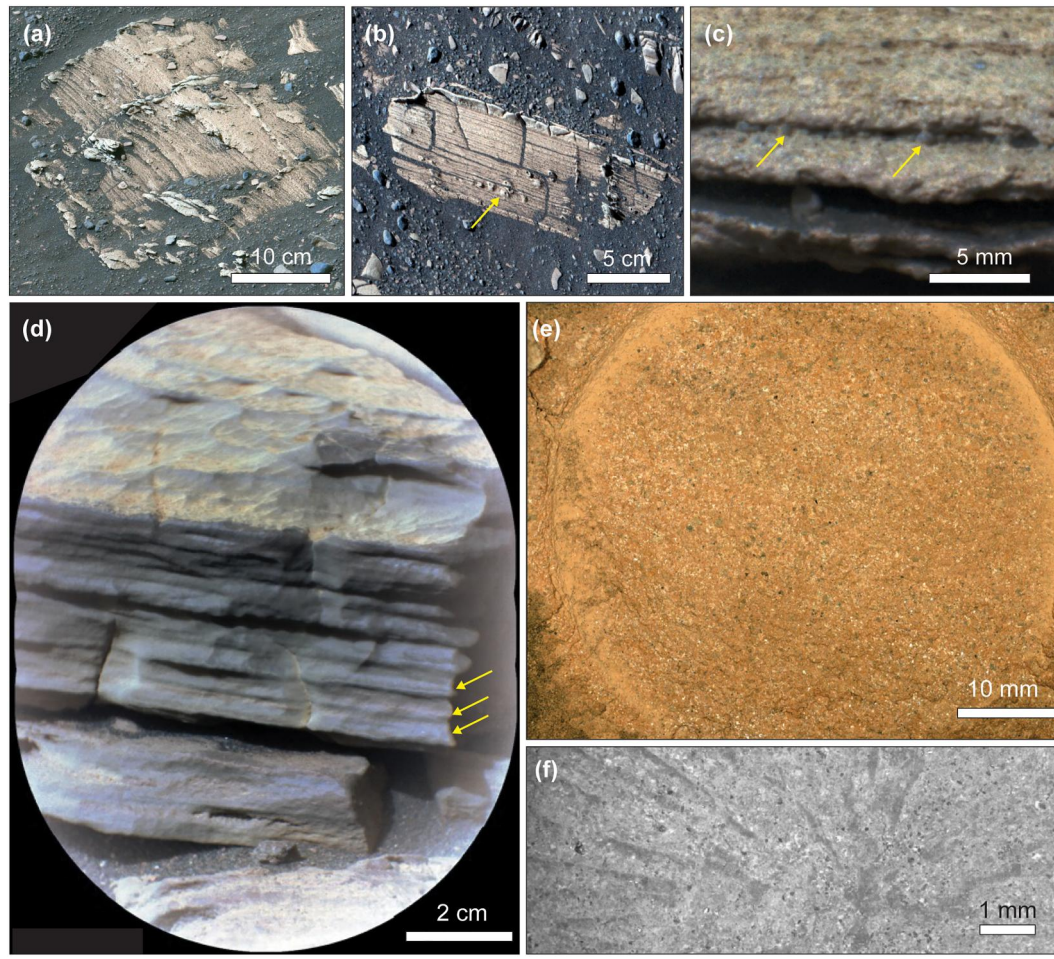

Figure 8. Laminated sandstone (S_l) facies. (a) Thinly laminated sandstone at the "Little Devil's Stairs" target imaged by Mastcam-Z 110 mm (zcam08456) on sol 441. (b) Concretions within thinly laminated sandstone near Little Devil's Stairs in the Devil's Tanyard member in a Mastcam-Z 110 mm mosaic (zcam08694) acquired on sol 695. (c) Coarse sand grains (yellow arrows) within laminations in the sol 443 SuperCam RMI target "Moody Creek." (d) "Hook Glacier" Supercam RMI target acquired on sol 424 at the Amalik outcrop showing thin laminations. Erosional edges suggestive of fining-upwards trends (inferred very fine to fine sanstone to mudstone based on RMI pixel scale) within bundles of laminations. (e) Rose River Falls partial abrasion at the transition between the Devils Tanyard and Hughes River Gap members imaged by WATSON on sol 452. (f) SHERLOC ACI image of the Novarupta abrasion patch at the Amalik outcrop acquired on sol 570.

grains in Rose River Falls are fine sand-sized, with grains ranging from coarse silt (near the limit of WATSON resolution; no ACI images were acquired of this target) up to very coarse sand (>1 mm diameter). Grains measured in SuperCam RMI images range from very fine sand to very coarse sand (e.g., Figure 8c), with grains in the medium sand range being most common (Figure S10, Table S2 in Supporting Information S1).

Some occurrences of this facies (e.g., at Devil's Tanyard) show a relatively high Fe/Mg sulfate content (up to ~20 wt. % sulfate), although another occurrence of this facies (e.g., Amalik) is distinguished by the presence of serpentine and minor carbonate as observed by PIXL, SuperCam, and SHERLOC (Dehouck et al., 2023; Hurowitz et al., 2023; Roppel et al., 2023). This facies preserves some of the strongest local variations in rock color and oxide spectral signatures (e.g., Amalik, Rose River Falls), which are attributed to variable oxidation and/or bleaching by diagenetic fluids (Mandon et al., 2023).

5.3. Low-Angle Cross Stratified Sandstone (S_x)

The low-angle cross stratified sandstone (S_x) facies is characterized by platy-weathering mm-scale laminations and cm-scale thin beds (up to ~4 cm thick, Figures S3–S5, Table S1 in Supporting Information S1) that form a

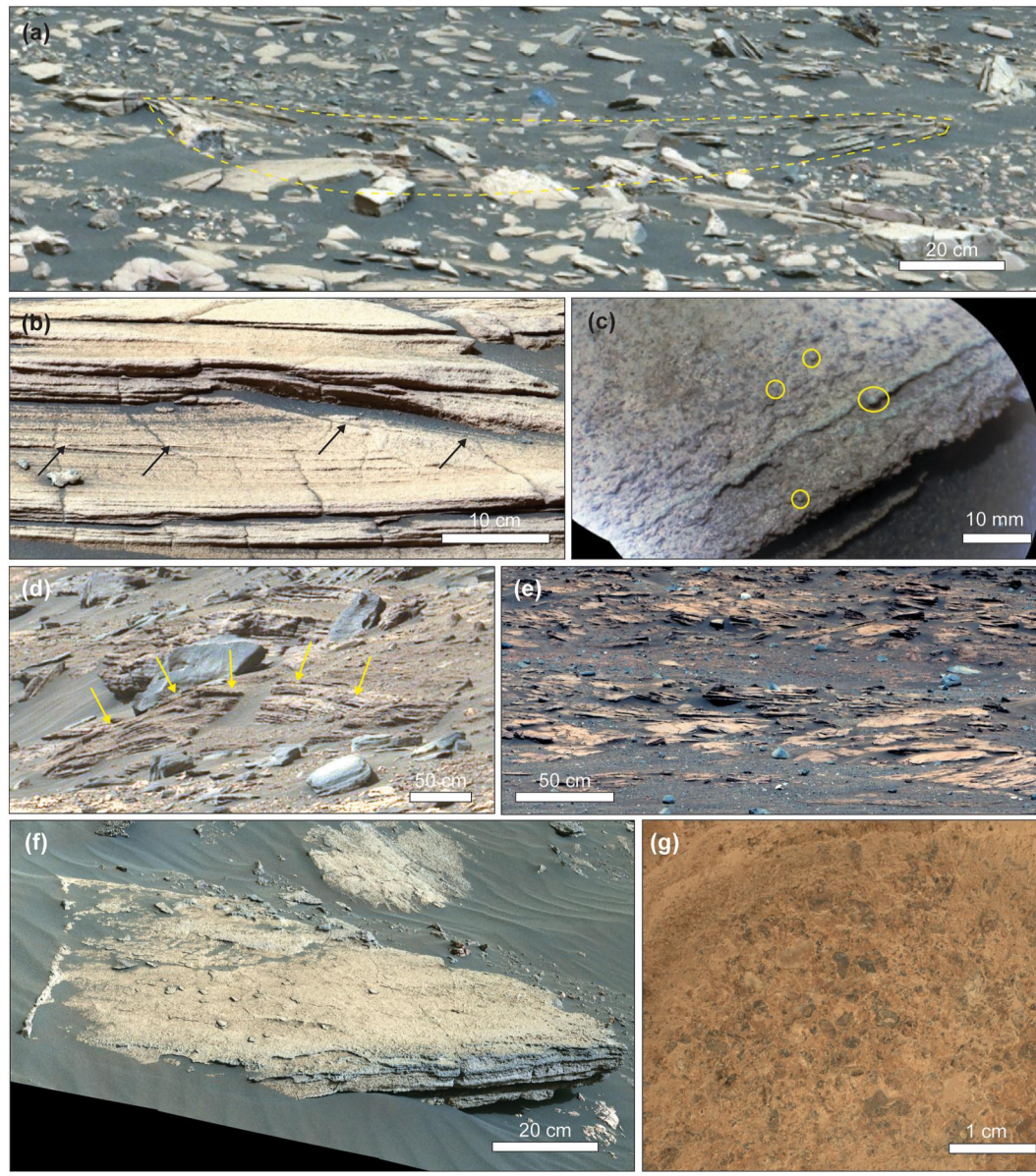

Figure 9. Low-angle cross-stratified sandstone (S_x) facies. (a) Low-angle scour (traced by yellow dashed line) visible in the middle interval of the Hogwallow Flats member in the Smith Mountain Mastcam-Z 110 mm mosaic (zcam08482) acquired on sol 461. (b) Low-angle truncations visible in the Kaguyak outcrop in a Mastcam-Z 110 mm mosaic (zcam08442) acquired on sol 422. (c) Medium sand-sized grains visible in the "Cape Gull" SuperCam RMI mosaic acquired at the Kaguyak outcrop on sol 424. (d) Convex-up low-angle structure within the lower Rockytop member above Hogwallow Flats in the Smith Mountain Mastcam-Z 110 mm mosaic (08482) acquired on sol 461. (e) Cross-stratified sandstone in the eastern extension of the lower Rockytop member in a Mastcam-Z 110 mm mosaic (zcam08555) acquired on sol 536. (f) Mastcam-Z 110 mm mosaic (zcam08498) acquired on sol 477 of the Skinner Ridge outcrop within the lower Rockytop member. (g) WATSON image of the Thornton Gap abrasion acquired on sol 485.

variety of geometries including dm-scale shallow troughs with low-angle margins, dm-scale low-relief, convex-up bedsets, and truncated sets of low-angle dipping planar laminations and beds (Figure 9). The rarity of resolvable granule or pebble-sized clasts in Mastcam-Z and SuperCam RMI images suggests that this facies consists predominantly of well- to moderately-sorted, sand-sized and finer grains. This inference is supported by measurements in several SuperCam RMI images that show resolvable grains ranging from fine to very coarse sand (Figure 9c; Figures S11, S12, and Table S2 in Supporting Information S1). WATSON and ACI images of the Thornton Gap abrasion show a predominance of well- to moderately-sorted medium to coarse sand grains

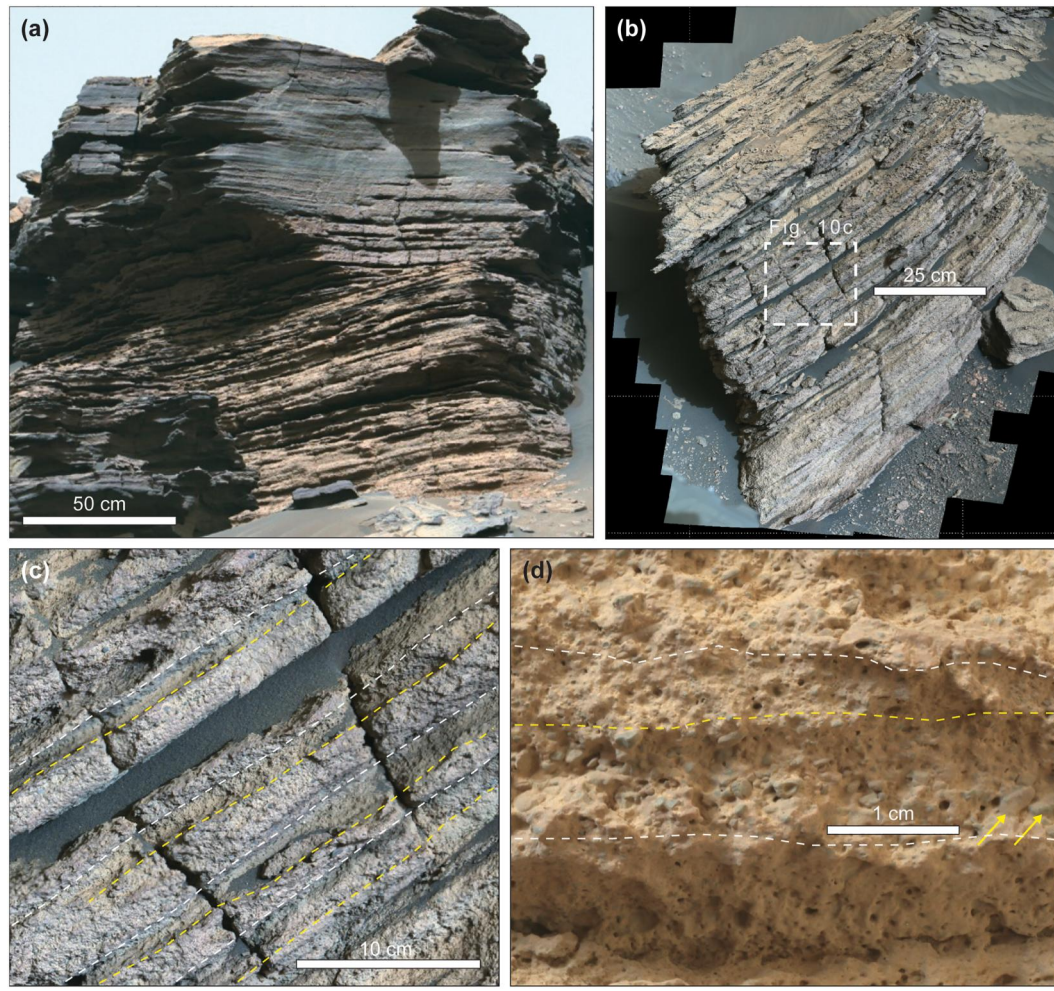

Figure 10. Thin-bedded granule sandstone (S_{tn}) facies. (a) Thin-bedded planar beds and laminations in upper Rockytop within an Mastcam-Z 110 mm mosaic acquired on sol 507 (zcam08529) showing apparent amalgamation of laminations near the top of the outcrop. (b) Mastcam-Z 110 mm mosaic (zcam08498) acquired on sol 477 of Betty's Rock, a float block of the Upper Rockytop member. (c) Zoom-in to coarse-fine couplets within Betty's Rock in a Mastcam-Z 110 mm mosaic (zcam08498) acquired on sol 477. Yellow dashed lines mark the upper boundary of coarser-grained intervals; white dashed lines mark the upper boundary of finer-grained intervals. (d) Subscene of the "Blackrock" target on Betty's Rock imaged on sol 476 with WATSON illustrates grain shape as well as the clast supported configuration and clast stacking in the coarser beds. Yellow arrows point to imbricated clasts in grain-to-grain contact. Yellow dashed lines trace the upper contact of granule beds, white dashed lines trace the upper contact of sandier intervals.

(Figure 9g; Figure S12 in Supporting Information S1). Sphericity of grains is variable, ranging from low to high, and grains are generally sub-rounded to well rounded (Figures 9c and 9g).

Some occurrences of this facies (e.g., middle Hogwallow Flats locality) fall within the sulfate-bearing class of rocks described by Hurowitz et al. (2023) and Dehouck et al. (2023), and are distinguished by the presence of ~20–30 wt % Fe/Mg sulfate. Other examples of this facies, such as lower Rockytop (e.g., Thornton Gap abrasion) and Kaguyak, were classified within the carbonate-bearing class of Shenandoah formation rocks (Dehouck et al., 2023; Hurowitz et al., 2023; Roppel et al., 2023). Diagenetic veins are rare (Nachon et al., 2023).

5.4. Thin-Bedded Granule Sandstone (S_{tn})

This facies is characterized by tabular, thin beds (~1–5 cm thick) of medium to very coarse-grained sandstone alternating with thin beds of granule conglomerate (Figure 10; Figure S5, Table S1 in Supporting Information S1).

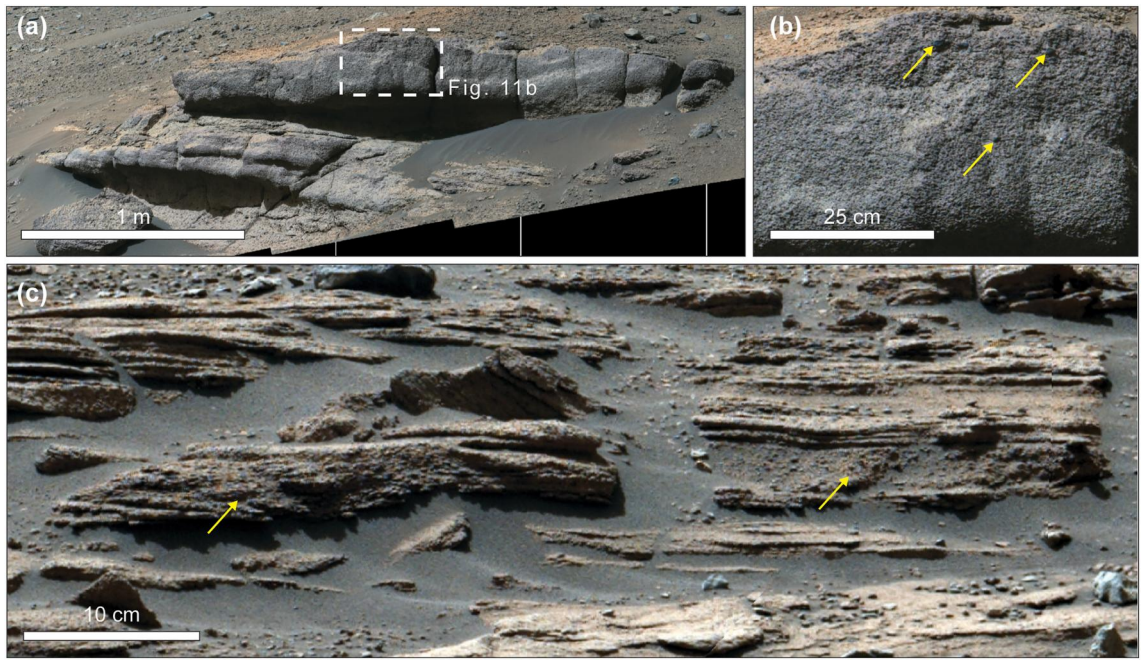

Figure 11. Thick-bedded pebbly sandstone and conglomerate (G_{th}). (a) The Knob Mountain outcrop within a Mastcam-Z 110 mm mosaic (zcam08559) acquired on sol 538. (b) Zoom in to granules and pebbles (yellow arrows) in the upper layer of Knob Mountain within Mastcam-Z 110 mm mosaic (zcam08559) on sol 538. (c) A thick bed of pebbly sandstone/conglomerate (yellow arrows) interbedded with low-angle cross-stratified sandstone at the Rainbow River outcrop near the base of Cape Nukshak in a Mastcam-Z 110 mm mosaic (zcam08580) acquired on sol 563.

The conglomerate clasts are inferred to represent diverse lithologies based on their variation in tone and color (Figure 10d). Planar bedding dominates this facies and no ripple- or high-angle cross-stratification have been definitively identified (Figures 10a and 10b).

Clasts within this facies were imaged by the remote sensing mast cameras and with the WATSON camera on the rover's turret. Within the coarser-grained beds, clasts are equant to tabular in form, sub-rounded to sub-angular in shape (Figure 10d). Thin sandstone and granule conglomerate beds are clast supported, with clast imbrication common (Figure 10d). Thicker beds appear normally graded (Figure 10c).

The mineralogy of the conglomerate is consistent with detrital clasts of pyroxene, feldspar, and lithic fragments displaying diverse compositions (Dehouck et al., 2023). Fe/Mg-carbonate cement and secondary Ca- and Mg-sulfate, Cl salts, and phosphates are also present (Hurowitz et al., 2023).

5.5. Thick-Bedded Granule-Pebble Sandstone and Conglomerate (G_{th})

The thick-bedded granule-pebble sandstone and conglomerate (G_{th}) facies is characterized by planar to sub-planar, cm to dm-scale structureless beds (Figure 11). Beds are comprised of poor to moderately-sorted coarse sand to pebbles with abundant vugs that likely represent voids left behind by eroded or plucked clasts (Figure-11b). These coarser-grained beds sometimes alternate with moderately to well-sorted cm to dm structureless or crudely layered beds comprised of coarse to very-coarse sand-sized grains (Figures 11a and 11c). Thick beds do not appear to be graded, and no sedimentary structures such as ripple cross-laminations or cross-bedding were observed within the thick beds. This facies is devoid of diagenetic concretions.

6. Sedimentary Successions

In order to understand the stratigraphic distribution of facies in outcrop context, the sedimentary successions exposed at Cape Nukshak and Hawksbill Gap are described in detail below (Figure 12). On Earth, sedimentological analysis is typically conducted on pre-defined stratigraphic nomenclature. For the Shenandoah formation, stratigraphic division of the succession and facies analysis were conducted simultaneously as the rover collected observations. Since stratigraphic and depositional correlations between successions were not always

Journal of Geophysical Research: Planets

10.1029/2023JE008187

Table 1
Sedimentary Facies of the Shenandoah Formation

Facies	Texture (grain size)	Sedimentary structures	Interpretation	Key outcrops	Members	Abrasions	Samples	Other relevant target names
Laminated mudstone (M_l)	Silt to very fine sands, locally rare coarse sands Subrounded to well-rounded grains	Planar, horizontal laminations; deformed laminations	Settling from suspension in a low energy, subaqueous environment	Wildcat Ridge (lower Hogwallow Flats), Amalik, Hidden Harbor (Yori Pass)	Cape Nukshak: Amalik, Yori Pass Hawksbill Gap: Hogwallow Flats	Berry Hollow, Elkwallow Gap (partial), Uganik Island	Hazeltop, Bearwallow, Kukaklek	Pignut Mountain, Smith Mountain, Moraine Creek
Laminated sandstone (S_l)	Fine to very coarse sands	Planar horizontal laminations; deformed laminations	Upper flow regime plane beds or setting from suspension in a subaqueous environment	Devils Tanyard, Sunset Hill, Knife Creek, Alagnak	Cape Nukshak: Amalik, Knife Creek, Alagnak, Yori Pass, Hawksbill Gap: Devils Tanyard, Hughes River Gap	Novarupta, Rose River Falls (partial)	Shuyak, Mageik	Lake Coville, Little Devils Stairs, Brown Mountain
Low-angle cross stratified sandstone (S_x)	Very fine to very coarse sands, locally up to pebbles	Low-angle cross stratification	Lower flow regime three-dimensional bedforms, scour fills in a subaqueous environment	Lower Rockytop, Middle Hogwallow Flats, Kaguyak	Cape Nukshak: Kaguyak, Yori Pass (Intricate Bay), Hawksbill Gap: Hogwallow Flats, Lower Rockytop	Thornton Gap	Swift Run, Skyland	–
Thin-bedded granule sandstone (S_{tn})	Medium to very coarse sand matrix with granule-sized clasts	Variably horizontal to inclined planar bedding, local grading	High density, bedload transport in a subaqueous environment	Upper Rockytop, Betty's Rock (float block)	Cape Nukshak: Alagnak Hawksbill Gap: Upper Rockytop, Knob Mountain	N/A	N/A	Kakhonak, Hagelbargers Pass
Thick-bedded granule-pebble sandstone and conglomerate (G_{th})	Medium to very coarse sand matrix with granule to pebble-sized clasts	Horizontal bedding; no grading	High density, bedload transport in a subaqueous environment	Knob Mountain, Alagnak, Rainbow River	Cape Nukshak; Kaguyak, Alagnak Hawksbill Gap: Knob Mountain	N/A	N/A	–

Table 2
Members of the Shenandoah Formation Observed at Cape Nukshak

Member name	Description	Facies	Geochemical class	Key outcrops	Abrasions	Samples
Kaguyak	Reddish-tan-colored, low angle cross-stratified, medium-grained sandstone with decimeter-scale lenses of granule to pebble-sized clasts interbedded near the member's base	S_l, S_x, G_{th}	Sulfate-silicate	Kaguyak (type locality), Rainbow River	N/A	N/A
Amalik	Erosion-resistant, grayish, purple-coated planar laminated mudstone-sandstone that transitions laterally into highly deformed soft sediment deformed laminations	M_l, S_l, G_{th}	Carbonate-silicate	Amalik (type locality), Trident Volcano	Novarupta	Shuyak, Mageik
Knife Creek	Recessively-weathering planar laminated mudstone and sandstone with pervasive soft sediment deformation	M_l, S_l	Sulfate-silicate	Knife Creek (type locality)	N/A	N/A
Alagnak	Sandstone bodies composed predominantly of thin-bedded granule sandstone, with some occurrences of planar laminated sandstone and low-angle cross-stratified sandstone. Member has a scoured, channelized base	S_l, S_{tn}, G_{th}	Unknown	Alagnak (type locality), Heidelberger Pass	N/A	N/A
Yori Pass	Recessively-weathering, sulfate-bearing, laminated sandstone and mudstone that transitions upward into cross-stratified sandstone bodies	M_l, S_l, S_x	Sulfate-silicate	Hidden Harbor, Intricate Bay	Uganik Island	Kukaklek

Table 3
Members of the Shenandoah Formation Observed at Hawksbill Gap

Member name	Description	Facies	Geochemical class	Key outcrops	Abrasions	Samples
Devils Tanyard	Discontinuous and mechanically disaggregated outcrops of predominantly plane parallel, flat-lying to shallowly dipping laminated sandstone, with rare low-angle truncations and several concretions	S_l	Sulfate-silicate	Devils Tanyard (type locality)	N/A	N/A
Hughes River Gap	Plane parallel, flat-lying to shallowly-dipping laminated sandstone with several intervals of deformed laminations, and a more continuous and uniform weathering expression	S_l	Sulfate-silicate	Hughes River Gap (type locality), Sunset Hill, Brown Mountain	N/A	N/A
Knob Mountain	Discontinuous, broad lens-like outcrops of recessively-weathering, poorly sorted pebbly sandstone interbedded with an erosion-resistant, moderately sorted, granule to pebble sandstone with crude cm-scale layering	S_{tn}, G_{th}	Sulfate-silicate	Knob Mountain (type locality)	N/A	N/A
Hogwallow Flats	Basal tan-colored, laminated mudstone that exhibits reddish-purple mottling and lenses of highly deformed and contorted laminations, a middle interval of platy-weathering, low-angle cross stratified sandstone, overlain by tan to purple laminated mudstone with occasional soft sediment deformation	M_l, S_x	Sulfate-silicate	Hogwallow Flats (type locality), Wildcat Ridge, White Rocks	Berry Hollow	Bearwallow, Hazeltop
Rockytop	Lower interval of planar, low-angle cross-stratified sandstone; upper interval of planar stratified, thin-bedded granule sandstones. Member thins laterally east and west	S_x, S_{tn}	Carbonate-silicate	Rockytop (type locality), Skinner Ridge	Thornton Gap	Swift Run, Skyland

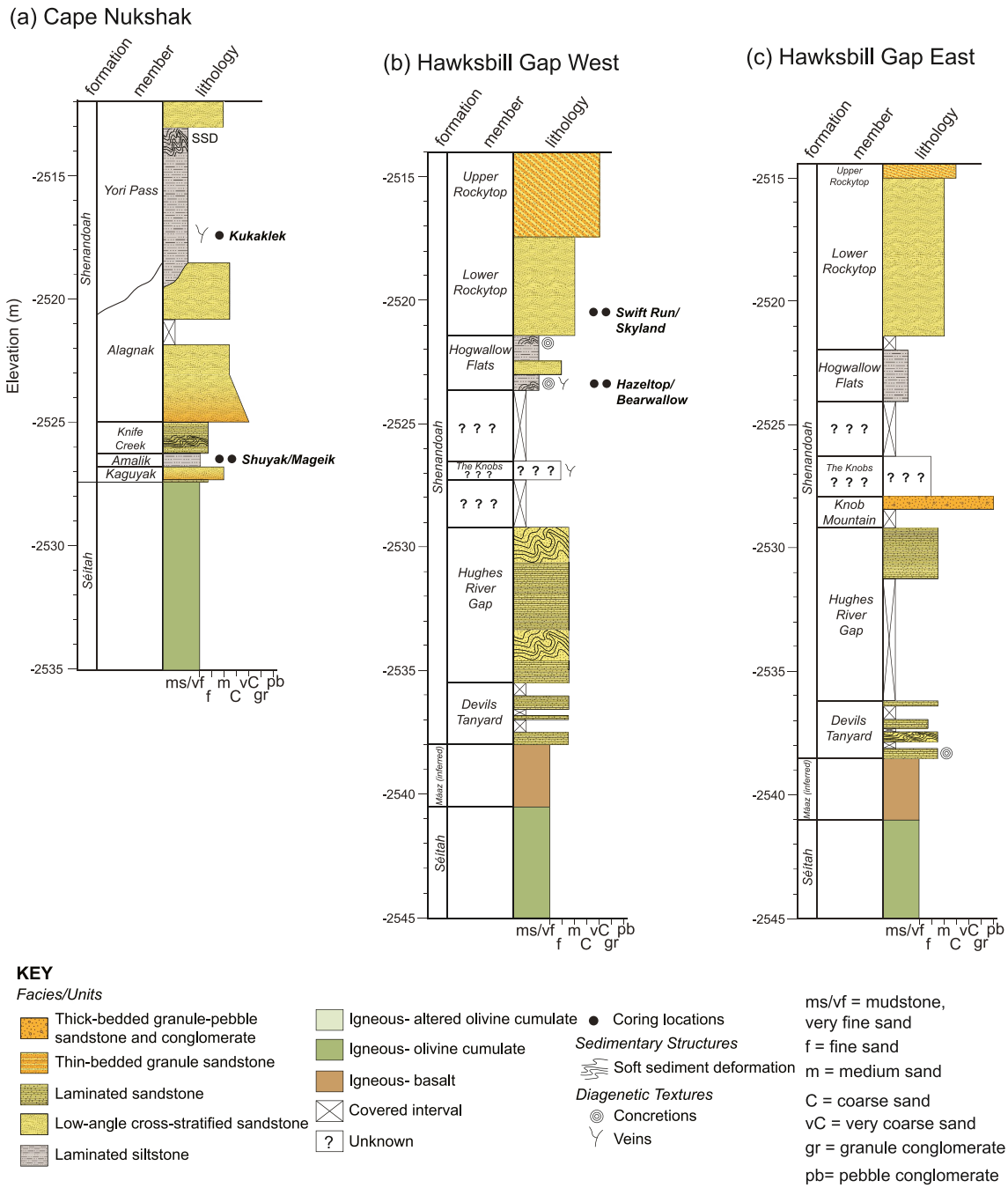

Figure 12. Stratigraphic columns for the Shenandoah formation at (a) Cape Nukshak, (b) Hawksbill Gap West, and (c) Hawksbill Gap East. The columns correspond to the locations annotated in Figure 2a. These columns include only those strata of the western fan front that have been designated Shenandoah formation by the Mars 2020 Science Team. These columns do not include strata exposed in the fan front exposures above the Shenandoah formation (e.g., Gupta et al. (2023) and Mangold et al. (2023)).

obvious or agreed upon by the team at the time of exploration, and to enable different interpretations of the stratigraphy in the future using the nomenclature presented here, we have chosen to split rather than lump members between and within the successions. Below we describe the stratigraphic succession and facies encountered at Cape Nukshak and Hawksbill Gap in the context of member designations to aid readers in following where observations were made (e.g., Figure 3a). This is important because interpretations of the depositional environment are highly context dependent. Stratigraphic members were defined and distinguished

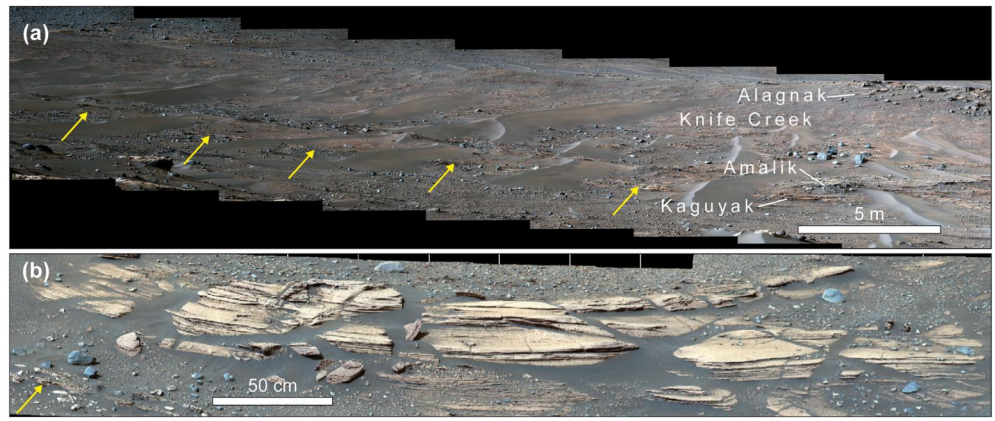

Figure 13. Kaguyak member at Cape Nukshak. (a) Mastcam-Z 110 mm mosaic (zcam08439) acquired on sol 420 of the base of Cape Nukshak showing the location of the Kaguyak outcrop and nearby lateral equivalents of the Kaguyak member (yellow arrows). (b) The Kaguyak outcrop within a Mastcam-Z 110 mm mosaic (zcam08442) acquired on sol 422. Note the thinly laminated, fine-grained facies underlying Kaguyak (yellow arrow).

primarily by major facies changes with elevation, and in some cases, by morphological characteristics and spatial distribution observed in orbiter images, and often correspond with the main outcrop exposures traversed and observed by Perseverance (Figures 3 and 12).

6.1. Cape Nukshak Section

6.1.1. Kaguyak Member

The basal member of the Shenandoah formation is a ~0.6 m-thick interval designated as the Kaguyak member (Figures 3, 12a, and 13). The contact between the underlying Séítah formation and the base of the Shenandoah formation was not observed at the surface due to the extent of sand and regolith cover in the area. The Kaguyak member crops out intermittently beneath modern aeolian bedforms over a lateral distance of ~40 m in the vicinity of the rover traverse (Figure 13a), although laterally equivalent strata can be traced in HiRISE orbiter images ~475 m to the northwest of Cape Nukshak, and ~200 m around the southeastern end of Cape Nukshak (Figures 2 and 3). Several ~decimeter-thick lenses of granule to pebble-sized clasts (G_{th}) are interbedded with sandstone near the base of the member (Figure 11c). At the namesake Kaguyak outcrop (Figure 13b), a ~10 cm-thick interval of laminated sandstone (S_l) transitions upward into an ~50 cm-thick distinctly reddish-tan-colored, low angle cross-stratified sandstone (S_x) (Figure 13b). The Kaguyak member is dominantly a medium-grained sandstone as determined by SuperCam RMI observations (Figure 9c; Figure S11, Table S2 in Supporting Information S1).

6.1.2. Amalik Member

Overlying the Kaguyak member is a ~0.5 m-thick interval designated the Amalik member (Figure 14). The Amalik member crops out laterally over a similar range as the underlying Kaguyak member (Figure 14a), and is defined at its base by a distinct change in color from the reddish-tan Kaguyak member to the dark-gray, erosion-resistant Amalik member (Figure 14a). Initial Mastcam-Z and SuperCam RMI observations of natural, weathered surfaces in the Amalik member suggested that this member was uniformly very fine-grained and composed of grains below the resolution of the rover's cameras (Figures 8d and 14b). However, the Novarupta abrasion revealed that a grayish, purple coating on the rocks was obscuring a grain size predominantly in the coarse silt to very fine sand range (Figure 8f). Patchy exposures of granule-pebble conglomerate (G_{th}) were observed at the northeastern base of the main Amalik exposure (Figures 14c and 14d), although most of the member appears much finer-grained. The Amalik member consists primarily of planar laminated mudstone-sandstone (M_l and S_l) (Figure-14b) that commonly shows lateral transition into highly deformed laminations (Figures 7e and 7f). Both the Amalik and Trident Volcano outcrops show strong variations in color from gray to red along fractures and in discrete zones (Figures 7e and 14b), suggesting late diagenetic alteration by oxidizing fluids (Mandon et al., 2023).

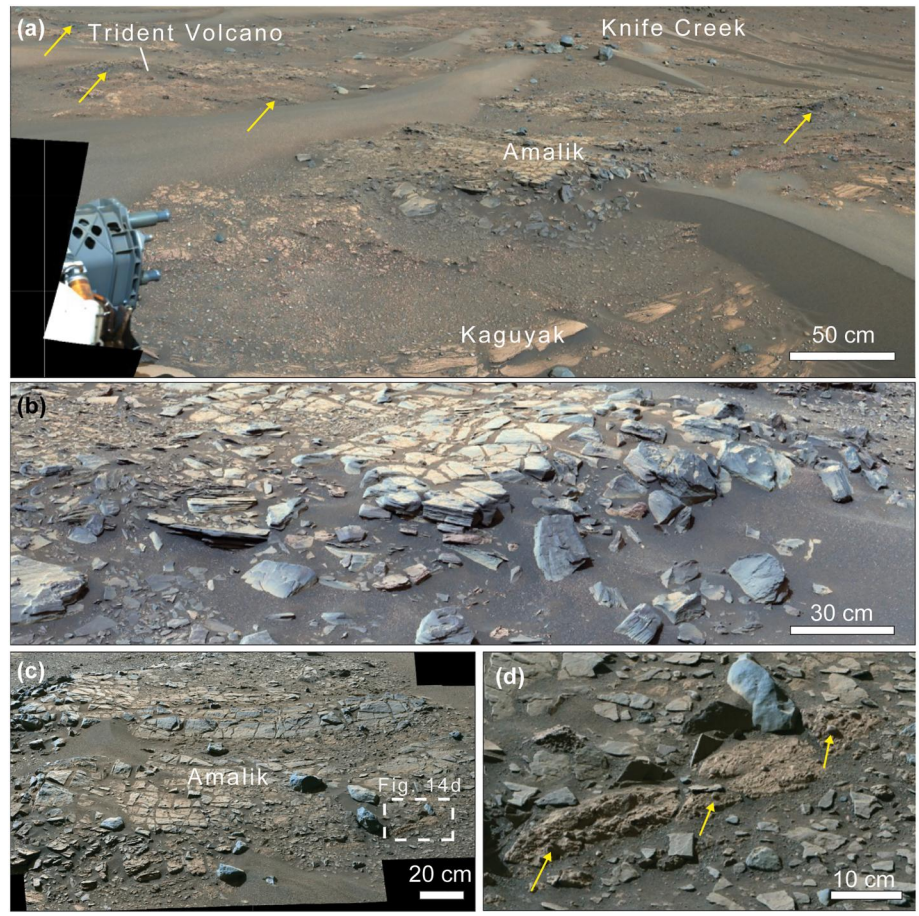

Figure 14. The Amalik member at Cape Nukshak. (a) The Amalik member at the namesake outcrop imaged by Mastcam-Z 34 mm (zcam08450) on sol 425. Yellow arrows show lateral extension of the Amalik member to the east and west of the namesake outcrop. (b) Gray, laminated blocks of the Amalik member imaged by Mastcam-Z 110 mm (zcam08444) on sol 423. (c) North side of the Amalik outcrop showing the location of granule-pebble conglomerate in (d) imaged by Mastcam-Z 110 mm (zcam08450) on sol 557.

6.1.3. Knife Creek Member

The Knife Creek member overlies the Amalik member (Figure 3a) and was only investigated with Mastcam-Z and Supercam. It is ∼1.5–2 m thick and comprised of recessively-weathering planar laminated mudstone and sandstone (M_l and S_l) (Figures 12a and 15). Grains were not readily resolvable with SuperCam RMI (∼60–100 μm diameter grains resolvable in an image with ∼20 μm/pixel resolution as in Figure 15c), indicating mud to very fine sand grain size unless these rocks are coated. The mudstones (M_l) and sandstones (S_l) at Knife Creek appear fissile and erode to form small thin plates (Figure 15b). Deformed laminations are pervasive throughout this interval (Figures 7e and 7f). It is difficult to trace this member laterally due to its recessive nature and extensive sand and regolith cover, but it appears to crop out discontinuously around Cape Nukshak section over a distance of ∼50 m (Figure 3a).

6.1.4. Alagnak Member

The ∼6 m thick Alagnak member overlies the Knife Creek member (Figures 3a, 12a, and 16). The contact between the two members is largely covered, although the base of ledge-forming sand bodies that comprise the Alagnak member appear irregular, with 0.25–0.5 m of relief locally (Figure 16a). This relief suggests that the lower Alagnak contact is erosional since the planar laminations of the Knife Creek member are unlikely to create such topography through a depositional process.

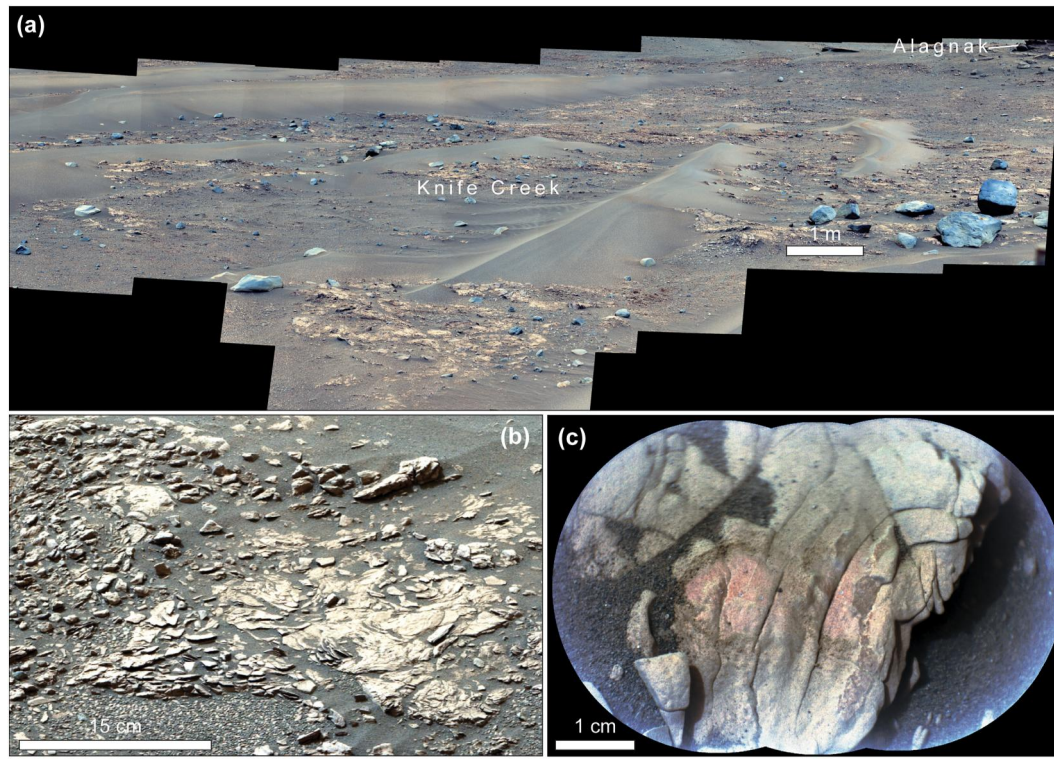

Figure 15. Knife Creek member at Cape Nukshak. (a) Recessively-weathering outcrop of the Knife Creek member at Cape Nukshak within a Mastcam-Z 110 mm mosaic (zcam08603) acquired on sol 588. (b) Platy, thin, deformed laminations of the Knife Creek member in a Mastcam-Z 110 mm mosaic (zcam08607) acquired on sol 593. (c) SuperCam RMI image of the Knife Creek target imaged on sol 593 showing the general fine-grained nature of the Knife Creek member.

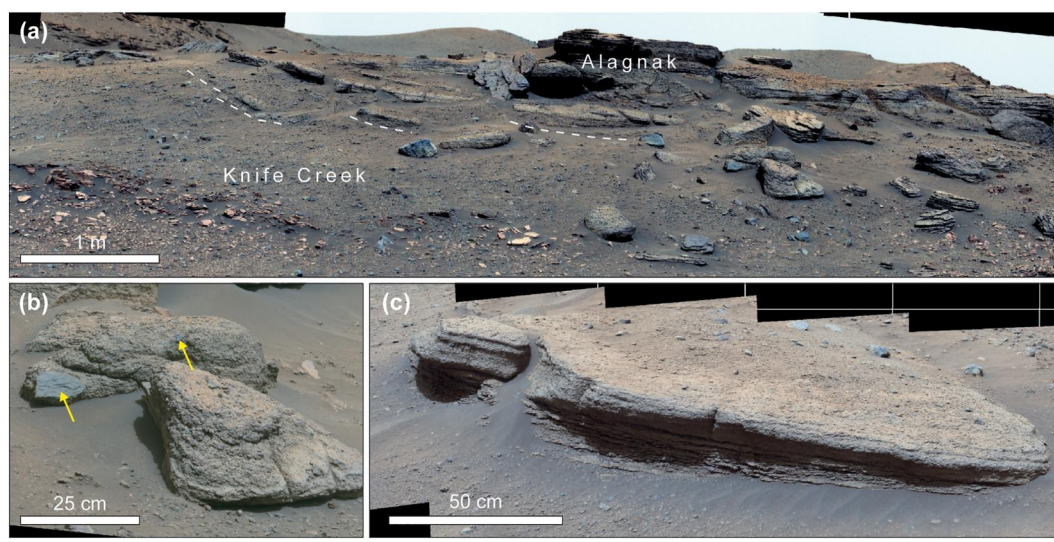

Figure 16. Alagnak member at Cape Nukshak. (a) Resistant, planar laminated sandstones (S_l) and thin-bedded granule-pebble sandstones (S_{tn}) of the Alagnak member within a Mastcam-Z 110 mm mosaic (zcam08613) acquired on sol 604. Dashed white lines trace the curvilinear, scoured base of several sandstone bodies. (b) Large, out-sized clasts up to 20 cm (yellow arrows) embedded within a sandstone matrix at Alagnak within a Mastcam-Z 110 mm mosaic (zcam08631) on sol 632. (c) Planar laminated sandstone S_l) within the "Hagelbargers Pass" block from the Alagnak member within a Mastcam-Z 110 mm mosaic (zcam08630) on sol 632. Grains fine upward from the base to the top of the block.

At the namesake Alagnak outcrop, the lowermost ∼2 m of this member is ledge-forming and exposed along the southern edge of Cape Nukshak (Figures 2b and 3a). In orbiter image-derived digital elevation products, the Alagnak ledge that defines Cape Nukshak can be traced 400 m to the west and 120 m northeast of Alagnak before it appears to pinch out (Figures 2b and 3a). The upper surface of Cape Nukshak provides a plan-view expression of the Alagnak member in orbiter images on which subtle, NW-SE-oriented bedrock ridges branch and superpose each other (Figure 2b). The Alagnak ledge was documented from multiple vantage points at a cm-scale by MastcamZ and SuperCam RMI, although no abraded or natural proximity science was acquired for this member. Rover observations of the upper ∼4 m of the Alagnak member were limited to engineering images acquired mid-drive.

The Alagnak member is composed of thin-bedded granule sandstone (S_{tn}), planar laminated sandstone (S_l), and thick-bedded granule-pebble sandstone and conglomerate (G_{th}) (Figure 16). At the base of the Alagnak member, coarse-grained facies occur as sandstone bodies, sometimes with a channelized base that scours the underlying Knife Creek member (Figure 16a). The sand bodies range in thickness from 0.25 to 0.5 m, are ∼0.25–4 m wide, and are amalgamated with multistory-multilateral stacking patterns (Figure 16a). The largest clasts within the Alagnak member generally range from 1 to 3 cm in diameter as observed with Mastcam-Z, although several larger pebbles and cobbles up to ∼20 cm were observed near the base of the member (Figure 16b). Most images of the Alagnak member are not high enough resolution to enable the recognition of grain-size trends within individual beds. However, images of inclined planar parallel beds at the site "Heidelberger Pass" show a clear fining upward trend, and gradual changes in bed thickness through the block (Figure 16c).

6.1.5. Yori Pass Member

The Yori Pass member overlies the Alagnak member. The elevation of this contact appears variable, with the Yori Pass member appearing to thin where the underlying Alagnak member extends to higher elevations (Figure 3a). This suggests an onlap relationship between the Yori Pass member and the underlying Alagnak member. The Yori Pass member consists of ∼10 m of recessively-weathering, sulfate-bearing, laminated sandstone and mudstone (M_l and S_l) (Figures 3a, 12a, and 17). The uppermost ∼3 m of the member includes cross-stratified sandstone (S_x) at an outcrop called "Intricate Bay" (Figure 17d). The Yori Pass member has a scree-covered, upper contact with an outcrop of sandstone called "Whale Mountain" that caps the Cape Nukshak section and is grouped with the overlying Tenby formation (Figure 17a) (Gupta et al., 2023; Ives et al., 2023; Mangold et al., 2023). In orbiter images, the Yori Pass member appears light-toned, possibly due to the accumulation of dust on continuous outcrop exposure, and can be traced laterally northwest around Cape Nukshak several kilometers to the northwest (Figure 3b), and ∼300 to the northeast toward Hawksbill Gap, where it appears to transition into the Hogwallow Flats member (Figures 2a and 3b).

The Intricate Bay outcrop consists of cross-stratified sandstone ∼0.5 m thick and ∼10 m wide (Figure 17d). The upper and lower contacts of this sandstone is covered, and it is difficult to tell whether its base incises or scours the underlying Yori Pass member mudstone. Bedding sets contain planar parallel and planar cross-stratified thin beds (S_l and S_x) (Figure 17d).

6.2. Hawksbill Gap Section

6.2.1. Devils Tanyard Member

The Devils Tanyard member is ∼2.5 m thick and composed of discontinuous and mechanically disaggregated outcrop exposed laterally ∼250 m along the base of Hawksbill Gap (Figures 2, 3, and 18). This member is bounded to the south by modern aeolian bedforms and inferred, regolith-covered Máaz formation, and to the north by the overlying Hughes River Gap member (Figures 2 and 18a). The Devils Tanyard member is interpreted based on RIMFAX reflectors to unconformably overlie Máaz formation igneous rocks (Paige et al., 2024; Figure 5).

In-place exposures of the Devils Tanyard member exhibit predominantly plane parallel, flat-lying to shallowly dipping laminated sandstone (S_l) (Figures 8a–8c). No significant scour, ripple, or dune cross stratification were observed. Deformed laminations are largely concentrated within a several decimeter-thick interval (Figure 7d). Diagenetic concretions are rare, with only several, mm-scale spherical concretions observed near the base of the member (Figure 8b); however, the member shows color variations from red to tan on the ∼meter scale as well as

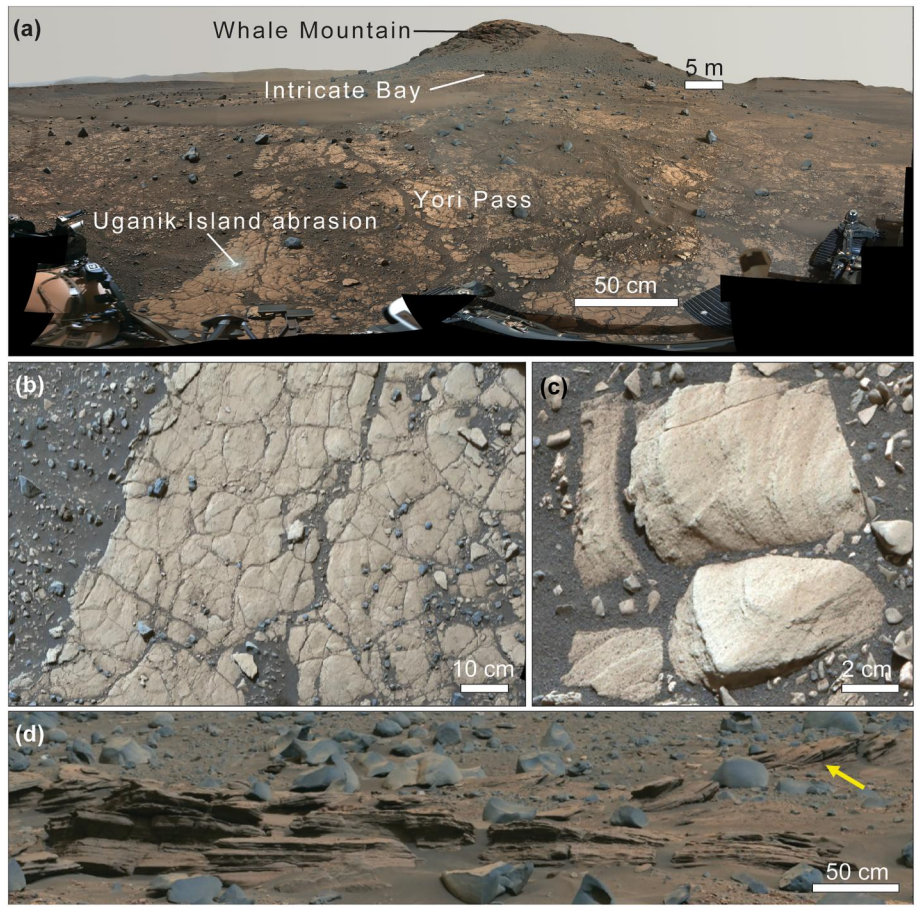

Figure 17. Yori Pass member and above at Cape Nukshak. (a) Mastcam-Z 34 mm left-eye mosaic (zcam08621, zcam08622, zcam08623) acquired between sols 615–619 showing the Yori Pass member, the Hidden Harbor outcrop where the rover abraded (Uganik Island), and overlying strata of Whale Mountain. (b) Representative bedrock of the Yori Pass member at the Hidden Harbor workspace imaged by Mastcam-Z 110 mm (zcam07101) on sol 610. (c) Thin laminations in the mudstones and sandstones of the Yori Pass member imaged by Mastcam-Z 110 mm (zcam08617) at the "Moraine Creek" target on sol 608. (d) Planar bedded and cross-stratified (yellow arrow) sandstones of the Intricate Bay outcrop near the top of the Yori Pass member imaged by Mastcam-Z 110 mm (zcam08618) on sol 610.

Mn-oxide coatings and fracture fills that likely indicate interactions with variable oxidizing and reducing diagenetic fluids (Mandon et al., 2023).

6.2.2. Hughes River Gap Member

The Hughes River Gap member overlies the Devils Tanyard member and is exposed ~370 m laterally in the Hawksbill Gap area of the western fan scarp. It ranges in apparent thickness between ~6.5 m (Sunset Hill outcrop, Hawksbill Gap West section) and ~7 m (Hawksbill Gap East section, mostly covered) (Figures 3a, 12b, and 12c). The contact between the Hughes River Gap and underlying Devils Tanyard member is largely obscured by sand and regolith, but near-continuous outcrop exposure at "Sunset Hill" reveals a likely conformable relationship between the two members (Figure 18b).

The Sunset Hill outcrop within the Hawksbill Gap West section represents the most vertically extensive section of the Hughes River Gap member observed by the rover (Figure 18b). At Sunset Hill, the Hughes River Gap member appears similar to Devils Tanyard, and is comprised predominantly of plane parallel, flat-lying to shallowly-dipping laminated sandstone (S_l) with two prominent intervals of deformed laminations, including at an area called "Brown Mountain" (Figure 7c). Although the Hughes River Gap member has similar sedimentary structures to the Devils Tanyard member, the Hughes River Gap member can be distinguished by its distinctive

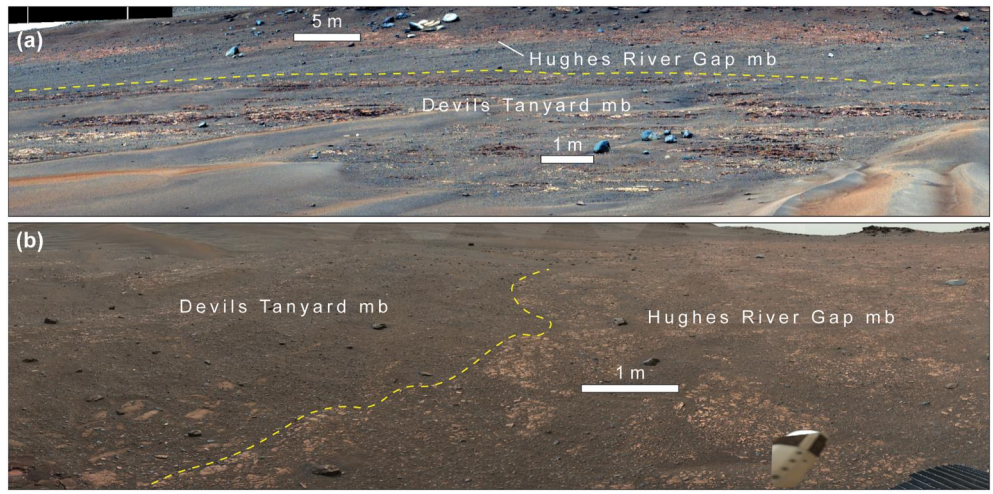

Figure 18. Devils Tanyard and Hughes River Gap members at Hawksbill Gap. (a) Mastcam-Z 34 mm mosaic (zcam03363) acquired on sol 439 showing the color distinction between the tan-colored Devil's Tanyard member and the distinctly red Hughes River Gap member. (b) A westward-looking perspective on the transition between Devil's Tanyard (to the south, left of the image) and Hughes River Gap (to the north, right of the image) members at the Sunset Hill outcrop in a Mastcam-Z 34 mm mosaic (zcam08468) acquired on sol 454, highlighting the subtle difference in outcrop continuity between the two members.

consistent reddish color observed in color HiRISE images and on the ground (Figures 2c and 18a), and its more continuous and uniform weathering expression compared to the Devils Tanyard member (Figure 18b).

6.2.3. Knob Mountain Member

The Knob Mountain member includes a series of discontinuous, resistant outcrops of thick-bedded granule-pebble sandstone and conglomerate (G_{th}) and thin-bedded granule sandstone (S_{tn}) (Figure 19a). It spans laterally ~30 m west to ~250 m east of the Hawksbill Gap East section (Figures 2 and 3a). Bedrock exposures of this member range in thickness from ~1 m at the namesake Knob Mountain outcrop (Figure 19a) to <10 cm where cover is extensive, with the resistant sandstone ledges disappearing beneath cover altogether to the west and east. The true thickness of this member is unknown given the covered intervals that underlie and overlie it (Figures 3, 12, and 19a). Patchy outcrop and float rocks of highly degraded sedimentary bedrock containing granule and pebble sized clasts above and below the resistant Knob Mountain member ledges suggest that this member may be up to several meters thick and has experienced strong mechanical fragmentation (Figure 11a).

The Knob Mountain member shows internal variability in layer thickness from fine laminations to decimeter-thick layers, and variable resistance to erosion (Figure 11a). At the namesake Knob Mountain outcrop within the Hawksbill Gap East section, the basal ~50 cm consists of a recessively weathering, poorly sorted, structureless pebbly sandstone (G_{th}) (Figure 11a). The dominant grain size is inferred to be in the sand size range, although resolving these grains is difficult because they are close to the limit of available RMI and Mastcam-Z image resolution (Figure 11a). This recessively-weathering, poorly sorted pebbly sandstone alternates with an erosion-resistant, moderately sorted, granule to pebble sandstone (Figure 11b).

6.2.4. The Knobs (Boston Knob, Kibler Knob, and Rice Mountain)

Three accumulations of decimeter- to meter-scale blocks informally known as "the Knobs" (Figures 3a and 19) occur along the same elevation contour above the Hughes River Gap member in the Hawksbill Gap West section, and above the Knob Mountain member in the Hawksbill Gap East section (Figures 12b and 12c). The Rice Mountain and Boston Knob blocks exhibit crude, cm-scale layering and appear dark in tone and aphanitic or fine-grained (Figure 19c). These blocks exhibit strong pyroxene signatures in SuperCam and Mastcam-Z spectra and appear unaltered (Dehouck et al., 2023; Horgan, Duflot, et al., 2023). These blocks are oriented in a way that is

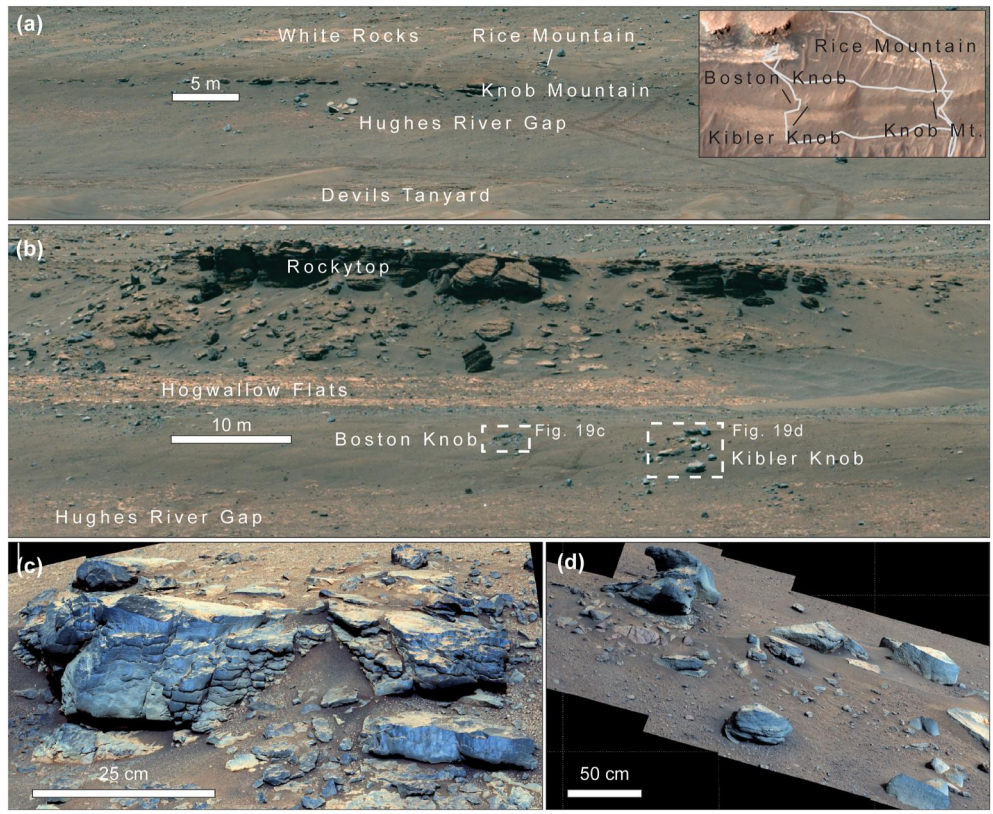

Figure 19. Knob Mountain member and the Knobs at Hawksbill Gap. (a) Outcrop context of the Knob Mountain member and Rice Mountain in a Mastcam-Z 110 mm mosaic (zcam03518 and zcam03519) acquired on sol 676. Inset shows the location of Rice Mountain and Knob Mountain relative to Boston Knob and Kibler Knob in (b). Center longitude/latitude coordinates for the inset are (77.407°, 18.458°). (b) Outcrop context for Boston Knob and Kibler Knob shown in a Mastcam-Z 110 mm mosaic (zcam03518 and zcam03519) acquired on sol 676. (c) Boston Knob imaged in a mosaic (zcam08480) by Mastcam-Z 110 mm on sol 459. (d) Kibler Knob blocks imaged in a mosaic (zcam08481) by Mastcam-Z 110 mm on sol 459.

consistent with in-place outcrop, however, the abundance of sand and regolith surrounding these blocks and their limited lateral exposure make it difficult to confirm in-place positioning versus float.

Kibler Knob (Figure 19d) consists of blocks located ∼6 m to the east of Boston Knob (Figure 19b). The 10+ blocks of Kibler Knob appear to be a similar lithology, including the namesake block that is dark-toned and massive to crudely layered (Figure 19d). The Kibler Knob blocks exhibit strong olivine and moderate carbonate signatures in SuperCam and Mastcam-Z spectra (Dehouck et al., 2023; Horgan, Duflot, et al., 2023). Kibler Knob sensu stricto may be embedded in the outcrop, but the other related blocks are interpreted as floats sitting on the surface.

The occurrence of these prominent blocks along the same elevation contour raises the possibility that the Knobs are in place, as large blocks embedded along the same horizon within a matrix of highly disaggregated bedrock. RIMFAX profiles also appear to show a distinct horizon above the Knob Mountain member, at the elevation of the Knobs, suggesting that this could be a laterally extensive and distinct unit. However, the limited outcrop exposure in this interval and the ∼3 m thick covered interval overlying the Knobs in which no other large blocks are observed, largely preclude an interpretation of the origin or stratigraphy of the Knobs with any certainty.

6.2.5. Hogwallow Flats Member

The Hogwallow Flats member (Figures 12b, 12c, and 20) overlies a 3–4 m thick covered interval that begins just above the Knobs (Figures 2c, 3a, 12b, and 12c). The namesake Hogwallow Flats outcrop exposes this member

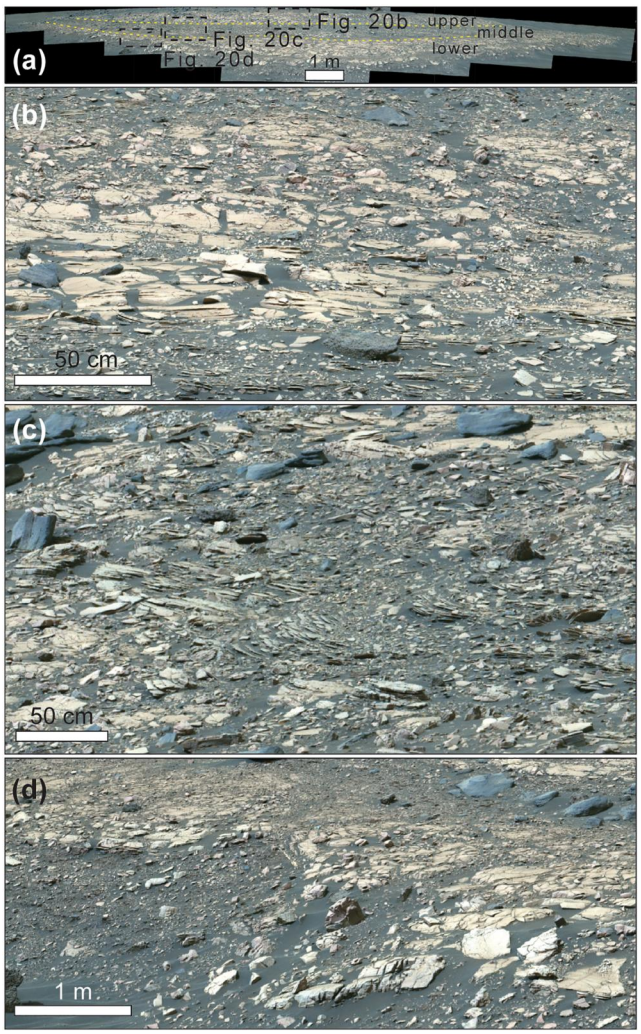

Figure 20. (a) Smith Mountain Mastcam-Z 110 mm mosaic (zcam08482) acquired on sol 461 showing the Hogwallow Flats member at the Hawksbill Gap type locality. (b) Upper, (c) middle, and (d) lower intervals of the Hogwallow Flats outcrop.

nearly continuously over a lateral distance of ~215 m, and is distinguished from other Shenandoah formation exposures by its brightness in HiRISE orbiter images (Figure 2c). The Hogwallow Flats member also extends discontinuously over ~330 m to the east, cropping out again at "White Rocks" within the Hawksbill Gap East section (Figures 2c and 3a).

At its base, the Hogwallow Flats member has an ~20 cm thick interval of tan-colored, laminated mudstone (M_l) that exhibits reddish-purple mottling (Figures 6a and 20d). Several lenses of highly deformed laminations occur within this interval (Figure 7b). This lower interval is overlain by an ~50 cm thick interval of tan flagstones that appear massive with hints of lamination (Figure 20d). WATSON and ACI images of the Berry Hollow abrasion at the Wildcat Ridge outcrop confirm a grain size of predominantly coarse silt and finer (Figures 6e and 6f; Figure S6, Table S2 in Supporting Information S1). The middle 50–70 cm-thick interval of Hogwallow Flats consists of platy-weathering, low-angle cross stratified sandstone (S_x) that appears distinctly dark in HiRISE orbiter images compared to the outcrop above and below it (Figures 2c and 20c). Individual grains are unresolvable in SuperCam RMI and Mastcam-Z images, although its erosional resistance suggests a slightly coarser grain size than the Hogwallow Flats strata above and below. Overlying the middle interval of Hogwallow Flats is a tan to purple laminated mudstone (M_l) with occasional deformed laminations like those observed in the lower part of outcrop (Figure 20b).

The Hogwallow Flats member is distinguished within the Shenandoah formation for both its composition and for its diversity of diagenetic and surface weathering textures (Broz et al., 2023). Geochemical and mineralogical analyses of the Hogwallow Flats member indicate the presence of phyllosilicates and ~20–30 wt % Fe/Mg sulfates (Dehouck et al., 2023; Hurowitz et al., 2023). Diagenetic features within the member include red and gray mottling (Figures 6a and 7b), Ca-sulfate fracture/vein fill (Figure 6f), spherical and concentrically layered concretions (Figure 6d), and manganese-rich coatings and fracture fill (Broz et al., 2023; Lanza et al., 2023; Nachon et al., 2023).

6.2.6. Rockytop Member

In the Hawksbill Gap area, a locally prominent, resistant unit named the Rockytop member overlies the Hogwallow Flats member and is comprised of an outcrop spanning ~200 m in width and ~10 m relief (Figures 2c and 21). The contact with the underlying Hogwallow Flats member is poorly constrained due the presence of regolith. Outcrop exposures of the Rockytop member appear to be the southernmost extent of a large ~60–70 m-thick set of strata, named "Jeremys Run" dipping ~3–5° to the south (toward azimuth ~170°) (Figures 2a, 21a, and 21b). The Rockytop member at its namesake outcrop in Hawksbill Gap is a plano-convex shape, pinching out at its eastern and western margins (Figure 21a).

This member is subdivided into upper and lower intervals (Figures 21d–21g). The lower Rockytop member, although not well-exposed, appears to be comprised largely of planar, low-angle cross-stratified sandstone (S_x) (Figures 9d–9f and 21g). Several decimeter-scale, low-angle convex barforms are observed at the base of lower Rockytop (e.g., Figure 9d). The upper Rockytop member is comprised of a set of planar stratified, thin-bedded granule sandstones up to 4 m thick within the Hawksbill Gap West section, thinning to <1 m in the Hawksbill Gap East section (Figures 10, 12b, 12c, and 21e–21g. At "Bettys Rock," a float block dislodged from the upper Rockytop member that was imaged by WATSON, cm-scale granule beds alternate with fine-grained sandy layers to form repeating couplets (Figure 10). A single decimeter-wide scour filled with pebbly conglomerate is observed within the planar sets (Figure 21f). Although the planar beds observed along the south-facing exposure at the namesake Rockytop outcrop appear sub-horizontal to shallowly-dipping, a

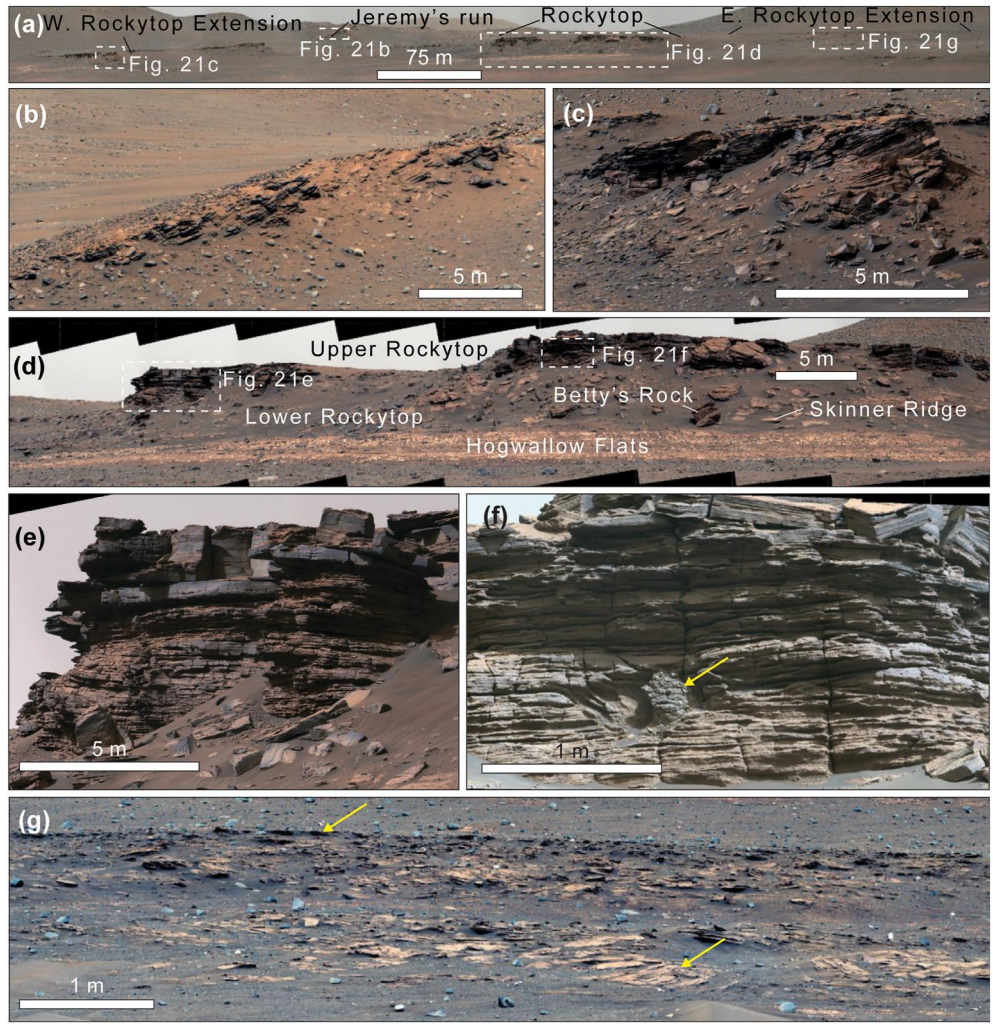

Figure 21. The Rockytop member at Hawksbill Gap. (a) Discontinuous outcrops of the Rockytop member are present at Hawksbill Gap and include the southern extension of Jeremy's Run, unnamed ledges (image left and right), and an area named Rockytop that was examined from multiple vantage points. These laterally confined outcrops exhibit a southward-dipping, broad convex form. The Rockytop member was imaged by Mastcam-Z 110 mm (zcam08427) on sol 411. (b) South-dipping beds within the southern extension of Jeremy's Run. Mastcam-Z 110 mm (zcam08702) acquired on sol 708. (c) Decameter-scale sets of asymptotic, south-dipping beds in an unnamed ledge west of Rockytop. Mastcam-Z 110 mm mosaic (zcam08479) acquired on sol 459. (d) Upper Rockytop is a ledge-forming unit comprised of horizontal to sub-horizontal tabular beds overlying slope-forming, light-toned Lower Rockytop and the Hogwallow Flat sulfate-cemented mudstone imaged by Mastcam-Z 110 mm (zcam08479) on sol 459. (e) Enlargement of Upper Rockytop where dark coating masks the centimeter-scale bedding at top of outcrop. Mastcam-Z 110 mm mosaic (zcam08528) acquired on sol 507. (f) A scour within Upper Rockytop defined by inclined beds, a concave base, and infilled with a distinct pebbly conglomerate imaged by Mastcam-Z 110 mm (zcam08549) on sol 526. (g) Eastern extent of the Rockytop outcrop and member showing thinning of resistant upper Rockytop member (upper arrow) and cross-stratified sandstone of lower Rockytop (lower arrow) in a Mastcam-Z 110 mm mosaic (zcam08555) on sol 536.

cross-sectional view through the upper Rockytop member along a nearby N-S trending outcrop exposure to the west shows several m-thick sets of asymptotic, parallel beds dipping ∼15–20° that shallow to near horizontal to the south (Figure 21c).

The mineralogy and geochemistry of the Rockytop member, as observed in the Thornton Gap abrasion from the lower Rockytop member, is notable for abundant (10's of wt %) Fe/Mg-carbonate present as coatings on igneous clasts, within altered clasts, dispersed within the matrix, possibly as a cement, and as lithic carbonate clasts (Hurowitz et al., 2023).

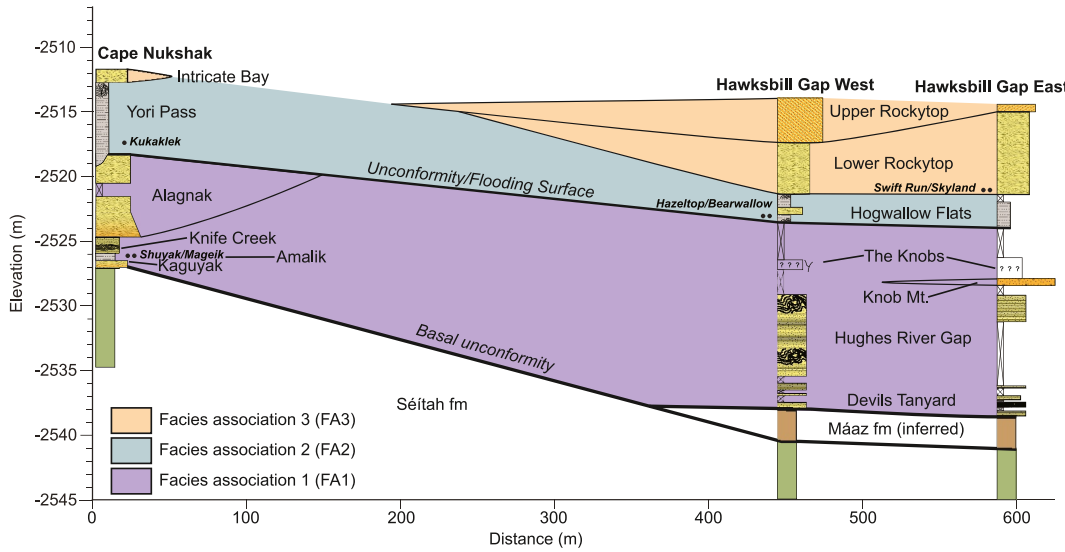

Figure 22. Stratigraphic columns from Cape Nukshak, Hawksbill Gap West, and Hawksbill Gap East plotted relative to each other in distance and elevation with vertical exaggeration, showing proposed correlations and facies associations.

6.3. Lateral Correlations Between Cape Nukshak and Hawksbill Gap

Direct correlations between the lower members of the Cape Nukshak and Hawksbill Gap sequences (e.g., Amalik, Kaguyak, Knife Creek, Alagnak, Devils Tanyard, Hughes River Gap, Knob Mountain) are challenging given the discontinuity of outcrop between the two sections, the lateral variation in facies on the order of 10–100s of meters, and the difference in elevation between the members (Figures 3a and 22). The low-angle cross-stratified sandstones observed at Kaguyak and the gray, coated laminated facies observed at Amalik are distinctive within the lower part of the Shenandoah formation, and do not have obvious lateral equivalents in the exposed Devils Tanyard or Hughes River Gap members at Hawksbill Gap. However, the laminated, deformed sandstones of the Knife Creek member at Cape Nukshak are similar to those observed in the lower members of the Hawksbill Gap sections. We note, though, that the Knife Creek member is thinner and occurs at a higher elevation than the Devils Tanyard and Hughes River Gap members at Hawksbill Gap (Figure 22). The Alagnak member at Cape Nukshak is potentially a lateral equivalent to the Knob Mountain member at Hawksbill Gap, but the discontinuity of outcrop and the covered interval above Knob Mountain make such a direct correlation uncertain. Rather than invoking direct correlations between members within this lowest part of the Shenandoah formation, we propose a facies association (Facies Association 1, FA1), described in detail in the following section (Section 7), that includes the Kaguyak through Alagnak members at Cape Nukshak and the Devils Tanyard through Knob Mountain at Hawksbill Gap (Figure 22).

The abrupt transition from the lower members of the Shenandoah formation to the fine-grained mudstones and sandstones of the Yori Pass member at Cape Nukshak and the Hogwallow Flats member at Hawksbill Gap is distinct and correlative across both areas (Figures 2 and 22). The Yori Pass and Hogwallow Flats members share a distinctive brightness observed in orbiter images, and although the two members differ slightly in elevation and local thickness, the presence of small outcrops with a similar morphology and erosional expression intermittently exposed between the two members makes a correlation reasonable (Figures 2, 3, and 22). These two members also share similar geochemistry and mineralogy (Dehouck et al., 2023; Hurowitz et al., 2023), and predominance of fine-grained laminated sandstone and mudstone facies (Figures 17 and 20). Thus, the facies observed within Yori Pass and Hogwallow Flats form Facies Association 2 (FA2).

The Rockytop member and its namesake outcrop, whose facies comprised Facies Association 3 (FA3), pinch out to the east and west within the Hawksbill Gap area. Although the Rockytop member does not appear to have a clear lateral equivalent within the Cape Nukshak section, the cross-stratified sandstones of Intricate Bay at Cape Nukshak are similar to that of the lower Rockytop member.

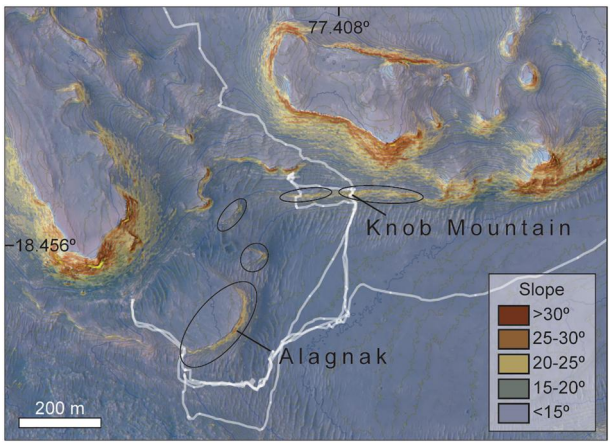

Figure 23. Slope map and 1 m elevation contours derived from HiRISE stereo data overlaid on a HiRISE basemap of Cape Nukshak and Hawksbill Gap area highlighting the laterally discontinuous coarse-grained lenses within Facies Association 1 (FA1) including Alagnak and Knob Mountain outcrops, circled in black.

7. Discussion

7.1. Shenandoah Formation Facies Associations and Depositional Interpretations

We identify and interpret three facies associations, groups of facies thought to have formed in a single sedimentary depositional environment, within the Shenandoah formation based on lithology, sedimentary structures, lateral extent, and stratigraphic position and stratal relationships.

7.1.1. Facies Association 1 (FA1): Distal Alluvial Fan Deposition

FA1 consists of laterally extensive, horizontal to subhorizontal laminated, plane parallel and deformed fine to coarse sandstones interbedded with broad, high aspect ratio (maximum ~250:1) lenses of granule to pebble sandstone. The lower Shenandoah formation at Cape Nukshak, including the Kaguyak, Amalik, Knife Creek, and Alagnak members, as well as the Devils Tanyard, Hughes River Gap, and Knob Mountain members at Hawksbill Gap exhibit FA1 (Figure 22). These members represent the stratigraphically lowest and oldest interval of the Shenandoah formation observed by Perseverance, and the overall lowest and oldest sedimentary rocks exposed at the fan front (Figures 12 and 22). This facies association appears to be in direct onlap relationship with the underlying igneous units of the Máaz and Séítah formations (Figures 4 and 5).

The most common lithofacies in FA1 is laminated sandstone (S_l), often deformed. We interpret the deformed laminations observed throughout FA1 as ductile soft-sediment deformation on the basis of folds consistent with small-scale slumps (e.g., Figure 7a), the presence of possible water escape structures (e.g., Figure 7b), and geometries inconsistent with those expected for depositional sedimentary bedforms (Figure 7). The laminations themselves could have been deposited as upper flow regime plane beds or through settling from suspension. Laminated sandstone (S_l) intervals up to 10 m thick are exposed in the Devils Tanyard and Hughes River Gap members at Hawksbill Gap. The same lithofacies is ~2 m thick in outcrops of the Amalik and Knife Creek members at Cape Nukshak (Figure 12). The deposition of plane parallel laminated sandstones can occur in both unconfined sub-aerial (e.g., North & Davidson, 2012) and unconfined sub-aqueous (e.g., Stow & Smillie, 2020; Talling et al., 2012) settings, and cannot alone be used as a diagnostic indicator for a specific depositional environment.

Although laminated sandstones are not diagnostic alone, the relationship of these laminated sandstones with stratified granule and pebble (S_{tn} and G_{th}) facies in the Alagnak and Knob Mountain members can help constrain their depositional setting. The granule- and pebble-bearing strata of FA1 are typically sub-horizontally, planar bedded and ungraded (Figures 11 and 16). The sorted nature of this lithofacies indicates that it was likely current transported. Therefore, the dominantly planar stratification of these facies is likely due to grain size being sufficiently coarse to suppress the formation of bedforms in favor of deposition in the lower plane bed regime (Lamb et al., 2012; Southard & Boguchwal, 2023). The creation of laterally extensive, planar laminated and soft-sediment deformed sandstone adjacent to and intercalated with channelized granule and pebbly sediments most likely reflects deposition by an unconfined sedimentary system that segregated grain sizes. The organization of these coarser-grained lithofacies into 50–250 m wide, high aspect ratio elements (Figure 23) is consistent with broadly channelized flowing water. Below, we consider two settings–a proximal prodelta and a distal alluvial plain–as possible explanations for Perseverance's observations of FA1.

In a sub-aqueous, pro-delta setting, distal or off-axis deposition in lobes created through hyperpycnal flows could have deposited laminated sandstones like those observed in FA1 (e.g., Grundvåg et al., 2023; Jackson & Johnson, 2009; Lamb et al., 2010; Plink-Björklund & Steel, 2004; Zavala, 2020). Hyperpycnal flows can be instigated by, or as, any type of sediment gravity flow, including as river-generated turbidity currents plunging down the front of a delta (e.g., Plink-Björklund & Steel, 2004) or cohesive debris flows derived from a fan delta. On Earth, quasi-steady, sand-rich, hyperpycnal flows are most commonly associated with river systems and often, specifically, with flooding events (e.g., Grundvåg et al., 2023). If FA1's planar laminated, soft sediment-deformed sandstones were deposited by subaqueous sediment gravity flows, they are most characteristic of laminae

deposited through rapid sediment fall-out from a high-density, sand-rich, turbidity current under quasi-steady (not surging) flow conditions (Bouma T_B, Kneller & Branney, 1995; Talling et al., 2012). Rapid deposition and slumping would have contributed to the common occurrence of soft-sediment deformation within this interval of the Shenandoah succession (Kneller & Branney, 1995).

While deposition via turbidity currents can easily explain the laminated sandstone facies and soft sediment deformation, such a process is difficult to reconcile with the deposition of the coarser-grained facies of FA1 as small, channelized, gravel-transporting systems. The capacity of turbidity currents to transport grains larger than sand-sized requires subaqueous flow depths of hundreds of meters (e.g., Amy & Dorrell, 2022). On Earth, gravel transport via turbidity currents is typically limited to very deep settings, like submarine canyons, that can accommodate such deep or thick flows. Given current constraints on the depth of the lake that might have occupied Jezero crater based on the thickness of nearby delta clinoform sets within the Kodiak butte (~10 m, Mangold et al., 2021), it seems unlikely that this setting could have accommodated subaqueous flow depths required for gravel transport. Additionally, the clear onlap relationship observed in the RIMFAX data in the subsurface at Cape Nukshak is inconsistent with very thick turbidity currents. Owing to their relatively low density and high momentum, turbidity currents are capable of running up opposing slopes and over obstacles many times their thickness, depositing sediments that drape topography (Lamb et al., 2004). Such thick currents, if responsible for depositing FA1 of the Shenandoah formation, likely would have been agnostic to the local antecedent topography of the underlying Séítah formation, and a draping rather than onlap relationship would be expected. Although slopes steep enough to transport coarser-grained clasts certainly can exist in subaqueous deltaic settings, the generally horizontal to subhorizontal orientation of the strata of FA1 is inconsistent with a depositional setting characterized by proximal steep slopes. Therefore, we find a pro-deltaic setting a less compelling explanation for FA1.

The facies within FA1 are more consistent with a sand-dominated distal alluvial plain (e.g., Marconato et al., 2022; Nichols, 2007). In this setting, the laminated sandstone facies would have been deposited as upper plane beds (Braat et al., 2023; Lapôtre & Ielpi, 2020) or settling from suspension from channel overbank processes (Best & Bridge, 1992; Fielding, 2006), or near the downstream terminus of a fluvial system where channelized flow ceases (North & Davidson, 2012; Tooth, 1999). The coarser-grained, broadly channelized deposits of FA1 would represent the extension or lateral migration of coarser-grained barforms. The cross-bedding and erosional scour between sand bodies observed throughout the Alagnak member of Cape Nukshak (e.g., Figure 16a), as well as the hint of channel body geometries on the top surface of the Cape Nukshak plateau (Figure 2b) and in the m-scale concave up structures in the subsurface RIMFAX data (Figures 4 and 5), lend additional support to an interpretation of channelized flow in a distal alluvial setting. Since soft-sediment deformation can occur in fluvial and alluvial systems with high discharge (van Loon, 2006, 2009), the presence of soft-sediment deformation is not out of place in our proposed depositional interpretation.

Of the proposed depositional environments, we favor the alluvial interpretation. While the relatively thick sequences of upper plane beds and the near-horizontal stratal dips of these beds could be reconciled with both hypothesized settings, several characteristics of FA1 are inconsistent with a prodeltaic, turbiditic setting. First, the channelized portions of FA1 transported coarse sediment, but are also relatively small both in their width (as small as 50 m) and potential flow depths (rare cross-bed sets up to 25 cm thick). Since turbidity currents are relatively dilute, their density is typically only slightly greater than the ambient fluid. Thus, the currents need to be very large, in Earth tens to hundreds of meters thick, or occur on very steep slopes, to generate enough boundary stress to transport coarse material like gravel (e.g., Amy & Dorrell, 2022). Rivers are readily capable of transporting this coarse sediment in relatively shallow flows due to their much greater fluid density relative to the ambient air. Second, the onlapping relationship between FA1 and the underlying Séítah formation is inconsistent with turbiditic deposition since that relationship indicates that deposition of FA1 was controlled by the underlying topography. A distal alluvial interpretation for FA1, dominated by relatively shallow, unconfined deposition of sand and the occasion gravel barform, is the best explanation for both its lithologic and stratigraphic character.

Within Jezero crater, a distal alluvial plain could represent either an alluvial fan or delta top setting. This distinction could have important implications for the amount and longevity of water in Jezero crater at the time of FA1 deposition. Given the spatial and temporal proximity of FA1 to deltaic deposits at Kodiak and higher up in the Shenandoah section, a delta top setting could be reasonable for an alluvial facies association if fluctuations in lake level or sediment supply resulted in progradation and retrogradation of the fluvial deltaic system over time.

However, FA1 is in direct onlap contact with underlying igneous Máaz and Séítah formations, the latter of which has up to tens of meters of topography on its upper surface, including at elevations higher than the FA1 exposures, directly to the east of the fan front (Farley et al., 2022). Although we cannot rule out the possibility that a delta and lake system existed basinward of FA1, it seems unlikely that sufficient accommodation space existed for such a contemporaneous system, at least directly east of Cape Nukshak and Hawksbill Gap. Therefore, we favor an alluvial fan setting for FA1.

7.1.2. Facies Association 2 (FA2): Lacustrine Deposition

Facies association 2 (FA2) consists of laminated mudstone to fine sandstone interbedded with intervals of low-angle scoured, laminated sandstone and is observed within the Yori Pass member at Cape Nukshak and the Hogwallow Flats member at Hawksbill Gap. Given the fine grain size and predominance of thin, horizontal to subhorizontal laminations within this facies association, we proposed that FA2 was likely deposited predominantly through settling from suspension with a minor component of traction deposition in a relatively low-energy subaqueous environment. The strata exhibiting FA2 can be traced laterally ∼530 m between the Yori Pass and Hogwallow Flats outcrops. It is likely that FA2 is even more laterally extensive given that a morphologically similarly unit can be traced nearly continuously in HiRISE orbiter images over ∼6 km along the fan front to the east (Figure 3b). The apparent continuity of FA2 along the western fan front further supports the interpretation of a low energy, laterally extensive depositional environment for FA2.

Depositional environments considered plausible for FA2 include settling from suspension in a lacustrine setting or as overbank deposits in an alluvial floodplain, both of which would be consistent with a sequence dominated by laterally extensive, fine-grained, horizontally laminated mudstone and sandstone. Bottom currents in a lacustrine setting or higher energy traction transport during overbank flooding events could have formed the low-angle, scoured facies observed within the middle interval of Hogwallow Flats. Although the depth of the standing body of water in which FA2 was likely deposited is not well-constrained, we do not observe features typical of intermittent subaerial exposure such as desiccation cracks, tepee structures, or breccias (i.e., Flannery et al., 2016). The absence of clear evidence for persistent or intermittent subaerial exposure and the great km-scale lateral extent of FA2 lead us to favor a lacustrine depositional setting, with water depths sufficient that intermittent subaerial exposure did not occur, over an alluvial floodplain interpretation.

The abundance of Fe-Mg sulfate (∼20–30 wt %) within FA2 at Hogwallow Flats and Yori Pass member has potentially important implications for the depositional conditions in which these sediments were deposited and initially lithified (Dehouck et al., 2023; Hurowitz et al., 2023). The presence of hydrated Fe-Mg sulfates within FA2, if representing a relatively early diagenetic lake precipitate, suggests that the lake or flood plain setting in which these sediments were deposited and initially lithified was anoxic and hypersaline. The abundance of Fe/Mg-sulfate distributed throughout the matrix of the Yori Pass and Hogwallow Flats members is perhaps easiest to explain as an early diagenetic cement. This explanation can be tested by observations of subaqueous evaporite textures, such as bottom-growth or crystal cumulates. Such textures have not been conclusively observed within FA2.

7.1.3. Facies Association 3 (FA3): Deltaic Deposition

Facies association 3 (FA3) is comprised of cross-stratified and sub-horizontal plane parallel, medium sandstone to granule conglomerate. The presence of cross-stratification and grain imbrication (e.g., Figure 10d) is evidence of deposition by tractive current flow. FA3 is observed at the Rockytop and upper Yori Pass (Intricate Bay) outcrops at Hawksbill Gap and Cape Nukshak, respectively, and occurs as laterally discontinuous convex lenses, with sharp, low-relief (<1 m) erosional contacts with underlying, fine-grained FA2 of the Hogwallow Flats and Yori Pass members. As there is no evidence for structural features such as faults or significant erosional contacts that could explain the laterally discontinuous exposure (e.g., Figure 21), we interpret these outcrops to be spatially distributed and restricted individual bodies rather than laterally extensive, continuous deposition like FA1 and FA2.

The plano-convex geometry of the Rockytop outcrop suggests that it may represent a cross-section through a lobe-like deposit possibly formed by sediment gravity flows (e.g., Giacomone et al., 2020). Alternating coarse-fine-grained couplets are consistent with event beds deposited from high density, bedload transport with tractional reworking as evidenced by clast imbrication (Figure 10d). This facies represents the best evidence for alternating,

episodic event beds within the Shenandoah formation section. The spatial occurrence of FA3 west of Rockytop (Figures 21b and 21c) at the southern toe of ~60-m-tall set of southward-inclined (~10–30°) beds at Jeremys Run provides contextual evidence that FA3 could represent deposition within the distal portion of a deltaic foreset (Gupta et al., 2023; Mangold et al., 2023). This is also supported by the asymptotic character of the couplets, exhibiting southward dips ~15° gently shallowing over meter length scales (Figure 21b). The similarity in elevation and proximity of FA3 to the Kodiak outcrop (Figure 1), interpreted as a deltaic sequence (Caravaca et al., 2023; Mangold et al., 2021) provides further contextual support for a deltaic interpretation.

Although the deltaic interpretation for FA3 is consistent with previous interpretations by Mangold et al. (2021) as well as the general depositional model proposed by Goudge et al. (2017, 2018), there remains some uncertainty about where the transition to predominantly fluvial deposition predicted by Schon et al. (2012) and Goudge et al. (2018), based on orbiter image observations of the upper surface of the western fan, might occur within the mid- to upper fan front sequence. Thus, an alternative interpretation of FA3 would place it in a fluvial setting, although it is important to note that FA3 does not exhibit any evidence for lateral accretion in a meandering fluvial environment as interpreted for fluvial strata on the top surface of the fan (e.g., Goudge et al., 2018; Schon et al., 2012). However, origins as either tabular, distal alluvial fan deposits or mid-channel fluvial bar forms may be more reasonable. The coarse-grained facies that comprise FA3, as well as the plano-convex geometry of the outcrops in this association, could be consistent with an origin as mid-channel bars in a braided river or as delta mouth bars (e.g., Cardenas et al., 2022). Alternatively, couplets of coarse sand and granule conglomerates could represent laterally extensive (on the scale of 10s to ~100 m), unconfined tabular beds deposited within an alluvial fan. Alluvial fan analogs from the Cenezoic Teruel and Ebro basins in Spain (e.g., Ventra & Nicholas, 2014) show such laterally extensive stacked tabular sheets, similar to those observed within upper Rockytop, with poorly developed cross stratification and no evidence for obvious channel incision, deposited within closed basins settings dominated by aggradation. An alluvial fan setting for FA3 could be consistent with the distal alluvial fan interpretation favored for FA1, although it would be harder to reconcile with deltaic interpretations for nearby strata in the upper fan front and at Kodiak. Thus, given the present state of knowledge we favor a deltaic interpretation for FA3, though do not fully reject alternate interpretations for these strata.

7.2. Depositional Model for the Shenandoah Formation

The integration of local geologic and geomorphic context, subsurface stratigraphy, and sedimentological analysis of lithofacies enables us to construct a depositional model for the Shenandoah formation that involves a temporal transition from initial distal alluvial deposition to development of lacustrine conditions followed by a transition to deltaic deposition within Jezero crater (Figure 24).

We propose that during a period initially dominated by wind erosion and non-deposition, several tens of meters in amplitude of antecedent topography was created on the top surface of the previously emplaced igneous Séitah formation in Jezero crater (Farley et al., 2022; Liu et al., 2021) (Figure 24a). Next followed the deposition of Máaz formation lava flows filling in local topographic lows of the antecedent Séítah formation topography (Farley et al., 2022; Horgan, Udry, et al., 2023; Figure 24b). The basal sequence of the Shenandoah formation was then deposited unconformably upon and directly overlying these igneous units as an alluvial fan system sourced from Neretva Vallis built out into the crater. Fan sediments locally onlapped this antecedent topography (Figure 24c). Where the underlying Máaz formation lava flows were completely eroded, or at elevations high enough on the paleotopography that the flows never reached, the Shenandoah formation was deposited directly on the Séítah formation, as at Cape Nukshak. Planar laminated sandstones were deposited rapidly as unconfined, upper flow regime plane beds or settling from suspension with the occasional higher energy flow depositing the coarser intervals at Kaguyak, Knob Mountain, and Alagnak.

Given the variation in elevation of the basal contact of FA2 at Hogwallow Flats and Yori Pass, we infer that the upper surface of FA1 prior to FA2 lacustrine deposition represents a sequence boundary characterized by subaerial exposure between the steps outlined in Figures 24c and 24d. There is sparse geologic context for the Knobs above the Knob Mountain outcrop, but this population of isolated blocks, particularly Boston Knob, could be an erosional lag deposit within the stratigraphy representing this period of subaerial exposure, or could represent high-energy flood deposition. A relative rise in base level within the crater, perhaps due to a substantial increase in water discharge through the Neretva Vallis system and/or a rise in groundwater level, resulted in transgressive flooding of a lake in the area of Perseverance's fan exploration, leading to deposition of the Yori Pass and

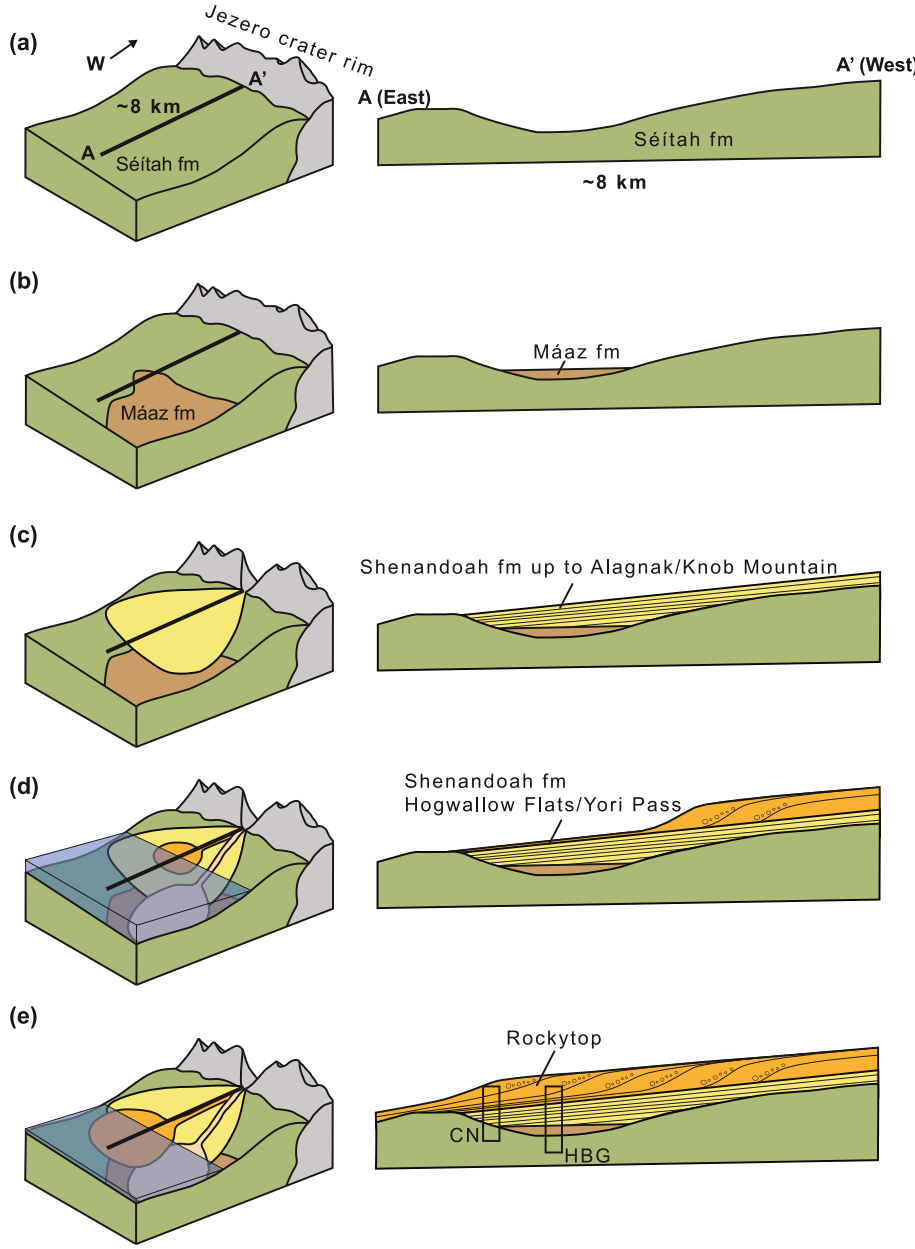

Figure 24. Schematic depositional model for the Shenandoah formation. (a) Emplacement and erosion of the igneous Séítah formation within Jezero crater to create antecedent topography (Farley et al., 2022) on which, (b) the lava flows of the Máaz formation were deposited (Farley et al., 2022; Horgan, Udry, et al., 2023). Emplacement of the Máaz formation was apparently topographically controlled by the Séítah antecedent topography. (c) Emplacement of the lower Shenandoah sequence up to Alagnak (Cape Nukshak) and Knob Mountain (Hawksbill Gap) in a distal alluvial fan entering Jezero via Neretva Vallis. (d) Filling of the crater and lake level rise result in a lacustrine setting in which the Yori Pass and Hogwallow Flats were deposited. These members are the distal equivalents of a developing river delta. (e) Subsequent progradation of the river delta leads to the deposition of the Rockytop strata. The meandering river deposits interpreted by Schon et al. (2012), Goudge et al. (2018), and Lapôtre and Ielpi (2020) on the upper surface of the fan could be part of a more proximal topset sequence contemporaneous with deltaic deposition at Rockytop. Deposition of the boulder deposits within the upper fan front described in Mangold et al. (2021) is presumed to have occurred sometime after (e) and is not illustrated here.

Hogwallow Flats members of FA2, as well as similar, laterally extensive units in a hypersaline lacustrine setting (Figure 24d). The laminated mudstones of FA2 suggest relatively low energy deposition, although the lenses of scoured and low-angle cross stratification within the middle interval of Hogwallow Flats suggest a nearshore environment in which deposition was occasionally influenced by current-driven traction transport. The

subsequent progradation of the Neretva Vallis river and delta system into the lake resulted in the deposition of FA3 as a series of delta clinoforms, via repeated episodic, density currents near the river-lake transition zone (Figure 24e). Boulder deposition in the upper strata of the fan interpreted by Mangold et al. (2021) to represent younger, high energy, flood deposition within the crater is presumed to have occurred sometime after the Shenandoah formation.

Because the elevation range of the Shenandoah formation is entirely below the lowest incision elevation of the Pliva Vallis outflow channel that erodes on the eastern rim of Jezero (−2,395 m), we infer that the deposition of this sequence occurred entirely within a closed basin system, consistent with the interpretation of Mangold et al. (2021) based on the Kodiak delta remnant and upper fan exposures to the east. It is unclear whether the deposition of the Shenandoah formation occurred prior to or during the filling of the Jezero paleolake that ultimately breached the crater rim, or whether Shenandoah formation deposition occurred after the Pliva Vallis breach.

7.3. Implications for the Aqueous History and Paleoclimate of Jezero Crater

Our favored interpretation of the paleoenvironmental evolution of the Shenandoah formation proposes a transition from initial fluvial deposition in an alluvial fan setting (FA1) to development of a lake system (FA2). Above the basal lacustrine unit, an interval indicative of progradation of a river delta (FA3) is observed. This succession implies a transition from an environment in which surface water may have been intermittent and relatively ephemeral to conditions capable of supporting and sustaining a lake setting and progradation of a river delta into the lake basin. This model is in partial agreement with previous interpretations by Goudge et al. (2017, 2018). Goudge et al. (2017, 2018) interpreted the strata of the Shenandoah formation to represent delta foreset and bottomset beds. Similarly, we interpret FA3 to represent delta deposition as foresets or mouth bar deposits. Additionally, the lacustrine deposits of the Hogwallow Flats and Yori Pass members (FA2) may represent a laterally extensive, several-m-thick interval of bottomset beds deposited basinward of the delta system. Where our model diverges from previous interpretations is in the interpretation of FA1. Rather than bottomset beds in a lacustrine setting (Goudge et al., 2017, 2018), we interpret the lower Shenandoah formation to record deposition in a distal alluvial fan setting. From a contextual perspective, this interpretation is sensible as there likely must have been water input via rivers into the crater before it flooded and created a lake; an early alluvial fan environment would seem inevitable. We do not observe evidence for meandering fluvial deposition within the Shenandoah formation, which Schon et al. (2012) and Goudge et al. (2018) interpreted for the strata exposed on the upper surface of the fan, although this transition may occur further upsection than the succession examined here.

Our data provide strong support for an active hydrological cycle during the time of Shenandoah formation deposition, and a record of possible local or regional paleoclimate evolution. The sedimentary character of the lower Shenandoah sequence (FA1) with deposition in an alluvial fan setting does not necessitate persistent flow of liquid water at the surface. Rather, sediment transport and deposition in such a setting could have resulted from intermittent and relatively short-lived surface flow in an arid climate. The transition from an alluvial fan setting to a lake and prograding delta indicates an increase in water flux to the crater leading to drowning of the basal alluvial deposits due to lake level rise as indicated by the transition from FA1 to FA2. The lacustrine deposits of FA2, which can be mapped along-strike for kilometers, and the overlying river delta deposits indicate establishment of a crater lake system in Jezero. While growth of the lake was due to water discharge from fluvial systems of the western fan, it is likely that the rise and maintenance of the groundwater table, and a regional change in humidity, likely contributed to a sustained lake setting capable of supporting the progradation of the river delta system observed within the upper Shenandoah formation.

Observations of the Shenandoah formation in Jezero crater, coupled with Curiosity's observations of a long-lived lake in Gale crater (Grotzinger et al., 2015), provide compelling evidence that the paleoclimate of ancient Mars was capable of sustaining habitable aqueous environments at its surface. If geochronology of the Shenandoah samples upon return to Earth shows that aqueous activity in Jezero crater is older than that in Gale, as has been previously estimated based on crater counts (Fassett & Head, 2008; Grant & Wilson, 2019; Grant et al., 2014; Le Deit et al., 2013; Palucis et al., 2016; Thomson et al., 2011), the Shenandoah formation rocks would further extend and constrain the window of surface habitability and aqueous activity on Mars.

7.4. Implications for Habitability and Biosignature Preservation in Jezero Crater

The Mars 2020 Perseverance rover was tasked with exploring and assessing the habitability of an astrobiologically relevant environment (Mustard et al., 2013). This assessment includes determining the origin of the rocks explored by the rover, determining the sequence of depositional, emplacement and modification events, and identifying signs of habitability and zones of enhanced biosignature preservation potential (Mustard et al., 2013).

Perseverance's exploration of the Jezero fan front unequivocally confirms the past presence of both the flow and accumulation of liquid water at the surface in Jezero crater. The preferred depositional model for the Shenandoah formation presented here includes transitions from fluvial to lacustrine to deltaic deposition, involving the steady inflow and persistence of standing water within Jezero crater. This sequence indicates habitable subaqueous depositional environments within Jezero and throughout the deposition of the Shenandoah formation. Greater availability of liquid water was likely associated with the rise in base level represented by the Hogwallow Flats and Yori Pass members, followed by progradation of the fluvial-deltaic system. Stable hydrological regimes provide clement conditions for the flourishing of numerous microbial consortia, for example, microbial mat-building ecosystems (e.g., Prieto-Barajas et al., 2018, and references therein). If such ecosystems ever emerged on Mars, their organic residues might remain preserved in rocks of the Shenandoah formation over billions of years, similar to the preservation of biogenic organic materials in siliciclastic records throughout Earth's history (Homann et al., 2015; Noffke, 2010).

While the primary sedimentology of the Shenandoah formation provides evidence for habitable subaqueous depositional environments; furthermore, the observation of diagenetic features such as sulfate-filled veins and abundant concretions within the Hogwallow Flats and Yori Pass members, in particular, also suggests the presence of sub- or near-surface fluid flow and water-rock interactions during early and late diagenesis (Kronyak et al., 2019; Sun et al., 2019). Late mobility and precipitation of sulfates and carbonates could have provided ephemeral habitable microenvironments within the sequence, extending the range and duration of habitability in the Shenandoah formation. Such rock-hosted microenvironments are particularly favorable settings for chemolithotrophic and endolithic microbiota that are widely considered plausible metabolic strategics for the putative martian biosphere (Onstott et al., 2019). Furthermore, sulfates are known to have high biosignature preservation potential and may entomb organic materials and fluid inclusions facilitating the characterization of these habitable microenvironments (Gill et al., 2023; Natalicchio et al., 2021).

The lacustrine Hogwallow Flats and Yori Pass members indicate periods of subaqueous deposition in low-energy settings ideal for the concentration and preservation of organic compounds and potential biosignatures of ancient microbial life. Although the higher energy fluvial depositional conditions of the lower Shenandoah members may be less favorable for the preservation of biosignatures, similarly coarse materials on Earth are also known to preserve small amounts of organic materials, for example, in situ and transported fragments of organic materials derived from biomass (Noffke, 2010). The prevalence of soft sediment deformation within the Shenandoah formation also suggests rapid deposition and burial of sediments and any potentially available organic material. This may have promoted anoxic paleodepositional settings with locally relatively closed diagenetic systems, which would have been conducive to the preservation of organic materials within this sequence (McMahon et al., 2018).

7.5. Implications for Returned Sample Science

The depositional model for the Shenandoah formation proposed here provides fundamental geologic context and paleoenvironmental constraints on the western fan front sample suite. RIMFAX data (Figures 4 and 5) shows an onlap relationship between the Shenandoah sedimentary sequence and the underlying igneous units of the Séítah and Máaz formations, suggesting that the fan front sample suite is younger than that collected on the crater floor (Simon et al., 2023). Using elevation as a general proxy for stratigraphic position, the Shenandoah stratigraphy suggests the following relative age sequence of the fan front samples: Shuyak/Mageik (Amalik member, oldest), Hazeltop/Bearwallow (Hogwallow Flats member), Swift Run/Skyland (Rockytop member), Kukaklek (Yori Pass member, youngest). The age relationship between Swift Run/Skyland and Kukaklek (highest elevation sample) is not well constrained. If the Rockytop member incised older strata of the Hogwallow Flats and Yori Pass members, the Swift Run and Skyland samples represent the youngest samples of the suite despite the lower elevation of lower Rockytop relative to the Yori Pass outcrop from which Kukaklek was collected. Alternatively, progradation of delta clinoforms in the Hawksbill Gap area could have been coeval with continued lacustrine deposition at

Cape Nukshak, allowing for the possibility that Kukaklek (higher elevation) does, indeed, postdate the Swift Run/Skyland samples.

Based on the depositional model proposed here, the western fan front sample suite represents a diversity of sedimentary environments, including: (a) deposition in a distal alluvial fan (Shuyak/Mageik), (b) low-energy deposition in a hypersaline lake setting (Hazeltop/Bearwallow and Kukaklek), and (c) deposition from episodic gravity flows on clinoforms of a prograding river delta system (Swift Run/Skyland). The samples also record the range of early to late diagenetic processes that occurred within the Shenandoah formation. Moreover, future analysis on Earth of Fe/Mg-sulfate (Hazeltop/Bearwallow and Kukaklek) and Fe/Mg-carbonate cements (Swift Run/Skyland) may provide records of early diagenesis and the primary aqueous geochemistry of a lake in Jezero crater (Dehouck et al., 2023; Hurowitz et al., 2023), while concretions (Hazeltop) and evaporite minerals (e.g., Ca-sulfate) in vug and fracture fills (Kukaklek and likely Hazeltop, Bearwallow) will yield knowledge of later diagenetic processes. Determining the timing and pervasiveness of fracturing and other late diagenetic processes will be key to establishing the reliability of potential biosignatures within these samples (Hays et al., 2017), and will demand high-sensitivity spatial geochemical data obtained within laboratories following sample return.

If returned to Earth, the Shenandoah formation sample suite could be used to test the depositional model proposed here. In particular, the relative and absolute ages of the members, formations, and facies associations, including the timing of fluvial and lacustrine activity, could be constrained using geochronology of cements and detrital minerals. The presence of unconformities from Séítah and Máaz formations through the Shenandoah sequence could be determined using both geochronology and observation of sharp changes in natural remanent magnetization. The origin of sulfate and carbonate minerals within the sequence as either detrital or authigenic could also be determined via laboratory analysis of their texture, composition, and magnetization. Finally, this suite of samples would facilitate detailed sedimentary petrography, petrology, and palaeoenvironmental reconstruction of habitable conditions within and outside Jezero crater (see also Simon et al., 2023).

8. Conclusions

(1) The Shenandoah formation, which crops out as the lower ~25 m of the erosional scarp of the Jezero western fan, is a clastic, sand-dominated, sedimentary succession and is the oldest sedimentary unit of Jezero's western fan to be explored by the Perseverance rover.
(2) Five main facies were identified within the Shenandoah formation: laminated mudstone, laminated sandstone, low-angle cross stratified sandstone, thin-bedded granule sandstone, and thick-bedded granule-pebble sandstone and conglomerate.
(3) These facies are organized into 3 facies associations: FA1 comprised of laminated and soft sediment-deformed sandstone interbedded with broad, unconfined coarser-grained granule and pebbly sandstone intervals, FA2 comprised predominantly of laterally extensive, soft sediment deformed laminated mudstone with occasional lenses of low-angle cross-stratified and scoured sandstone, and FA3 comprised of cross-stratified sandstone and tabular thin-bedded sand-gravel couplets.
(4) Although facies finer-grained than sandstone are generally scarce, the mudstone within FA2 of the Hogwallow Flats and Yori Pass members forms a laterally traceable marker bed. We interpret this as indicative of lower energy deposition in a lacustrine environment as a consequence of base-level rise and transgressive flooding of the lowermost alluvial succession.
(5) The depositional model favored for the Shenandoah formation involves the transition from fluvial deposition in a sand-dominated distal alluvial fan setting, to widespread lacustrine deposition within the crater, followed by the progradation of a river delta system into the lake basin.
(6) The Shenandoah formation explored and sampled by the Perseverance rover consists of a diverse set of sedimentary deposits representing distal fluvial, lacustrine, and deltaic depositional processes in a range of past habitable environments. Habitability may have endured following the deposition of the sequence during periods of water-rock interaction associated with endolithic microenvironments.
(7) Various facies in the Shenandoah formation record both early and late diagenetic processes and have variable biosignature preservation potential. The highest such potential is likely associated with the lower energy settings of the Hogwallow Flats and Yori Pass members, although organic materials including potential biosignatures may have become preserved in any of the samples collected.

Conflict of Interest

The authors declare no conflicts of interest relevant to this study.

Data Availability Statement

All Mars 2020 Perseverance rover data products and data sets used in this manuscript, including the calibrated source images from which the figures in this paper have been assembled, are archived in the Planetary Data System Imaging node (https://pds-imaging.jpl.nasa.gov/volumes/mars2020.html) and the Geosciences node (https://pds-geosciences.wustl.edu/missions/mars2020/): Navcam (Maki et al., 2020), Mastcam-Z images (Bell & Maki, 2021), Supercam RMI images (Wiens & Maurice, 2021), WATSON images (Beegle & Bhartia, 2021), RIMFAX (Hamran, 2021). The Mars 2020 Terrain Relative Navigation High Resolution Imaging Science Experiment (HiRISE) orthorectified Image Mosaic (Fergason et al., 2020a, 2020b) is available at: https://planetarymaps.usgs.gov/mosaic/mars2020_trn/HiRISE/JEZ_hirise_soc_006_orthoMosaic_25cm_Eqc_latTs0_lon0_first.tif. The HiRISE digital elevation model (Fergason et al., 2020a, 2020c) is available at: https://planetarymaps.usgs.gov/mosaic/mars2020_trn/HiRISE/JEZ_hirise_soc_006_DTM_MOLAtopography_DeltaGeoid_1m_Eqc_latTs0_lon0_blend40.tif.

Acknowledgments

This research was carried out in part at the Jet Propulsion Laboratory, California Institute of Technology under a contract with the National Aeronautics and Space Administration and with the support of NASA's Mars 2020 Project via subcontracts with the Jet Propulsion Laboratory, California Institute of Technology. This research was also supported by NASA via contract NNH15AZ241 to R. Wiens, the UK Space Agency via Grants ST/Y0001531/1 and ST/X002373/1 to S. Gupta and ST/V00560X/1 to K. Hickman-Lewis, the Royal Society via Grant SRF/R1/21000106 to S. Gupta, the Research Council of Norway via Grant 309835 to S. E. Hamran and 301238 to S.E. Hamran and H. Dypvik, the Canadian Space Agency via Grant 309835 supporting N. Randazzo, the Swedish Research Council via Grant 2022-04255 to S. Alwmark, the NASA Mars 2020 Participating Scientist Program via Grants 80NSSC21K0332 to A. Williams and 80NSSC21K0327 to L. Crumpler, and the NASA FINESST Fellowship via award 80NSSC22K1373 to O. Kanine. The authors would like to acknowledge the scientists and engineers of the Mars 2020 Perseverance and Mars Reconnaissance Orbiter missions for acquiring and providing the data used in this study. We would also like to thank Ben Cardenas and Mathieu Lapôtre for their valuable input and careful editing that improved this manuscript. Any use of trade, firm, or product names is for descriptive purposes only and does not imply endorsement by the U.S. government.

References

Amy, L., & Dorrell, R. (2022). Equilibrium sediment transport by dilute turbidity currents: Comparison of competence-based and capacity-based models. *Sedimentology*, *69*(2), 624–650. https://doi.org/10.1111/sed.12921

Arvidson, R. E., Ashley, J. W., Bell, J. F., Chojnacki, M., Cohen, J., Economou, T. E., et al. (2011). Opportunity Mars Rover mission: Overview and selected results from Purgatory ripple to traverses to Endeavour crater. *Journal of Geophysical Research*, *116*(E7), E00F15. https://doi.org/10.1029/2010JE003746

Beegle, L. W., & Bhartia, R. (2021). Mars 2020 SHERLOC bundle [Dataset]. NASA Planetary Data System. https://doi.org/10.17189/1522643

Bell, J. F., & Maki, J. (2021). Mars 2020 Mast Camera zoom bundle, from operations team, mosaic products [Dataset]. NASA Planetary Data System. https://doi.org/10.17189/bmkq-nm72

Bell, J. F., Maki, J. N., Mehall, G. L., Ravine, M. A., Caplinger, M. A., Bailey, Z. J., et al. (2021). The Mars 2020 Perseverance rover mast camera zoom (Mastcam-Z) multispectral, stereoscopic imaging investigation. *Space Science Reviews*, *217*(1), 24. https://doi.org/10.1007/s11214-020-00755-x

Best, J. L., & Bridge, J. S. (1992). The morphology and dynamics of low amplitude bedwaves upon upper stage plane beds and the preservation of planar laminae. *Sedimentology*, *39*(5), 737–752. https://doi.org/10.1111/j.1365-3091.1992.tb02150.x

Beyssac, O., Forni, O., Cousin, A., Udry, A., Kah, L. C., Mandon, L., et al. (2023). Petrological traverse of the olivine cumulate Séítah formation at Jezero crater, Mars: A perspective from SuperCam onboard Perseverance. *Journal of Geophysical Research: Planets*, *128*(7), e2022JE007638. https://doi.org/10.1029/2022JE007638

Bhartia, R., Beegle, L. W., DeFlores, L., Abbey, W., Razzell Hollis, J., Uckert, K., et al. (2021). Perseverance's scanning habitable environments with Raman and luminescence for organics and chemicals (SHERLOC) investigation. *Space Science Reviews*, *217*(4), 58. https://doi.org/10.1007/s11214-021-00812-z

Bibring, J.-P., Langevin, Y., Gendrin, A., Gondet, B., Poulet, F., Berthé, M., et al. (2005). Mars surface diversity as revealed by the OMEGA/Mars Express observations. *Science*, *307*(5715), 1576–1581. https://doi.org/10.1126/science.1108806

Bibring, J.-P., Langevin, Y., Mustard, J. F., Poulet, F., Arvidson, A., Gendrin, A., et al. (2006). Global mineralogy and aqueous Mars history derived from OMEGA/Mars Express data. *Science*, *312*(5772), 400–404. https://doi.org/10.1126/science.1122659

Blatt, H., Middleton, G., & Murray, R. (1972). *Origin of sedimentary rocks* (p. 634). Prentice-Hall.

Braat, L., Bruckner, M. Z. M., Sefton-Nash, E., & Lamb, M. P. (2023). Gravity-driven differences in fluvial sediment transport fluxes on Mars and Earth. Earth ArXiv. https://doi.org/10.31223/X5BQ0R

Broz, A. P., Horgan, B. H., Kalucha, H., Garczynski, B., Haber, J., Hurowitz, et al. (2023). Diagenetic alteration of Hogwallow flats, Jezero crater, Mars. In *Paper presented at the 54th lunar and planetary science conference 2023*. Retrieved from https://www.hou.usra.edu/meetings/lpsc2023/pdf/1845.pdf

Calef, F. J., III., Dietrich, W. E., Edgar, L., Farmer, J., Fraeman, A., Grotzinger, J., et al. (2013). Geologic mapping of the Mars science laboratory landing ellipse. In *Paper presented at the 44th lunar and planetary science conference 2013*. Retrieved from https://www.lpi.usra.edu/meetings/lpsc2013/pdf/2511.pdf

Caravaca, G., Dromart, G., Mangold, N., Gupta, S., Stack, K. M., Le Mouélic, et al. (2023). The deltaic depositional environments and stratigraphy of the Kodiak Butte (Jezero crater, Mars). In *Paper presented at the 54th lunar and planetary science conference 2023*. Retrieved from https://www.hou.usra.edu/meetings/lpsc2023/pdf/1473.pdf

Cardenas, B. T., Grotzinger, J. P., Lamb, M. P., Lewis, K., Fedo, C., Bryk, A., et al. (2022). Barform deposits of the Carolyn Shoemaker formation, Gale crater, Mars. *Journal of Sedimentary Research*, *92*(12), 1071–1092. https://doi.org/10.2110/jsr.2022.032

Carter, J., Poulet, F., Bibring, J.-P., Mangold, N., & Murchie, S. (2013). Hydrous minerals on Mars as seen by the CRISM and OMEGA imaging spectrometers: Updated global view. *Journal of Geophysical Research: Planets*, *118*(4), 831–858. https://doi.org/10.1029/2012JE004145

Crumpler, L. S., Horgan, B., Simon, J., Stack, K., Alwmark, S., Gilles, D., et al. (2023). In situ geologic context mapping transect on the floor of Jezero crater from Mars 2020 Perseverance rover observations. *Journal of Geophysical Research: Planets*, *128*(10), e2022JE007444. https://doi.org/10.1029/2022JE007444

Dehouck, E., Forni, O., Quantin-Nataf, C., Beck, P., Mangold, N., Royer, C., et al. (2023). Overview of the bedrock geochemistry and mineralogy observed by SuperCam during Perseverance's delta front campaign. In *Paper presented at the 54th lunar and planetary science conference 2023*. Retrieved from https://www.hou.usra.edu/meetings/lpsc2023/pdf/2862.pdf

Edgett, K. S., Yingst, R. A., Ravine, M. A., Caplinger, M. A., Maki, J. N., Ghaemi, F. T., et al. (2012). Curiosity's Mars hand lens imager (MAHLI) investigation. *Space Science Reviews*, *170*(1–4), 259–317. https://doi.org/10.1007/s11214-012-9910-4

Ehlmann, B. L., & Edwards, C. S. (2014). Mineralogy of the Martian surface. *Annual Review of Earth and Planetary Sciences*, *42*(1), 291–315. https://doi.org/10.1146/annurev-earth-060313-055024

Ehlmann, B. L., Mustard, J. F., Fassett, C. I., Schon, S. C., Head, J., Des Marais, D. J., et al. (2008). Clay minerals in delta deposits and organic preservation potential on Mars. *Nature Geoscience*, *1*(6), 355–358. https://doi.org/10.1038/ngeo207

Ehlmann, B. L., Mustard, J. F., Murchie, S. L., Bibring, J.-P., Meunier, A., Fraema, A. A., & Langevin, Y. (2011). Subsurface water and clay mineral formation during the early history of Mars. *Nature*, *479*(7371), 53–60. https://doi.org/10.1038/nature10582

Farley, K., & Stack, K. (2023). Mars 2020 initial reports volume 2 (samples 11-21). *Delta Front Campaign*. https://doi.org/10.17189/49zd-2k55

Farley, K. A., Stack, K. M., Shuster, D. L., Horgan, B. N., Hurowitz, J. A., Tarnas, J. D., et al. (2022). Aqueously altered igneous rocks samples on the floor of Jezero crater, Mars. *Science*, *377*(6614). https://doi.org/10.1126/science.abo2196

Farley, K. A., Williford, K. H., Stack, K. M., Bhartia, R., Chen, A., de la Torre, M., et al. (2020). Mars 2020 mission overview. *Space Science Reviews*, *216*(142), 142. https://doi.org/10.1007/s11214-020-00762-y

Fassett, C. I., & Head, J. W., III. (2005). Fluvial sedimentary deposits on Mars: Ancient deltas in a crater lake in the Nili Fossae region. *Geophysical Research Letters*, *32*, L14201. https://doi.org/10.1029/2005GL023456

Fassett, C. I., & Head, J. W., III. (2008). The timing of Martian valley network activity: Constraints from buffered crater counting. *Icarus*, *195*(1), 61–89. https://doi.org/10.1016/j.icarus.2007.12.009

Fergason, R. L., Hare, T. M., Mayer, D. P., Galuszka, D. M., Redding, B. L., Smith, E. D., et al. (2020a). Mars 2020 terrain relative navigation flight product generation: Digital terrain model and orthorectified image mosaics. In *Paper presented at the 5st lunar and planetary science conference*. Retrieved from https://www.hou.usra.edu/meetings/lpsc2020/pdf/2020.pdf

Fergason, R. L., Hare, T. M., Mayer, D. P., Galuszka, D. M., Redding, B. L., Smith, E. D., et al. (2020b). Mars 2020 terrain relative navigation HiRISE orthorectified image mosaic. https://doi.org/10.5066/P9QJDP48

Fergason, R. L., Hare, T. M., Mayer, D. P., Galuszka, D. M., Redding, B. L., Smith, E. D., et al. (2020c). Mars 2020 terrain relative navigation HiRISE DTM mosaic. https://doi.org/10.5066/P9REJ9JN

Fielding, C. R. (2006). Upper flow regime sheets, lenses and scour fills: Extending the range of architectural elements for fluvial sediment bodies. *Sedimentary Geology*, *190*(1–4), 227–240. https://doi.org/10.1016/j.sedgeo.2006.05.009

Flannery, D. T., Allwood, A. C., & Van Kranendonk, M. J. (2016). Lacustrine facies dependence of highly ^{13}C-depleted organic matter during the global age of methanotrophy. *Precambrian Research*, *285*, 216–241. https://doi.org/10.1016/j.precamres.2016.09.021

Gendrin, A., Mangold, N., Bibring, J.-P., Langevin, Y., Gondet, B., Poulet, F., et al. (2005). Sulfates in Martian layered terrains: The OMEGA/Mars Express view. *Science*, *307*(5715), 1587–1591. https://doi.org/10.1126/science.1109087

Giacomone, G., Olariu, C., Steel, R., & Shin, M. (2020). A coarse-grained basin floor turbidite system—The Jurassic Los Molles formation, Neuquen Basin, Argentina. *Sedimentology*, *67*(7), 3809–3843. https://doi.org/10.1111/sed.12771

Gill, K. K., Jagniecki, E. A., Benison, K. C., & Gibson, M. E. (2023). A Mars-analog sulfate mineral, mirabilite, preserves biosignatures. *Geology*, *51*(9), 818–822. https://doi.org/10.1130/G51256.1

Goudge, T. A., Milliken, R. E., Head, J. W., Mustard, J. F., & Fassett, C. I. (2017). Sedimentological evidence for a deltaic origin of the western fan deposit in Jezero crater, Mars and implications for future exploration. *Earth and Planetary Science Letters*, *458*, 357–365. https://doi.org/10.1016/j.epsl.2016.10.056

Goudge, T. A., Mohrig, D., Cardenas, B. T., Hughes, C. M., & Fassett, C. I. (2018). Stratigraphy and paleoohydrology of delta channel deposits, Jezero crater, Mars. *Icarus*, *301*, 58–75. https://doi.org/10.1016/j.icarus.2017.09.034

Goudge, T. A., Mustard, J. F., Head, J. W., Fassett, C. I., & Wiseman, S. M. (2015). Assessing the mineralogy of the watershed and fan deposits of the Jezero crater paleolake system, Mars. *Journal of Geophysical Research: Planets*, *120*(4), 775–808. https://doi.org/10.1002/2014JE004782

Grant, J. A., & Wilson, S. A. (2019). Evidence for late alluvial activity in Gale Crater, Mars. *Geophysical Research Letters*, *46*(13), 7287–7294. https://doi.org/10.1029/2019GL083444

Grant, J. A., Wilson, S. A., Mangold, N., Calef, F., III., & Grotzinger, J. P. (2014). The timing of alluvial activity in Gale crater, Mars. *Geophysical Research Letters*, *41*(4), 1142–1149. https://doi.org/10.1002/2013GL058909

Grotzinger, J. P., Arvidson, R., Bell, J. F., III., Calvin, W. M., Clark, B. C., Fike, D., et al. (2005). Stratigraphy and sedimentology of a dry to wet eolian depositional system, Burns Formation, Meridiani Planum, Mars. *Earth and Planetary Science Letters*, *240*(1), 11–72. https://doi.org/10.1016/j.epsl.2005.09.039

Grotzinger, J. P., Gupta, S., Malin, M. C., Rubin, D. M., Schieber, J., Siebach, K., et al. (2015). Deposition, exhumation, and paleoclimate of an ancient lake deposit, Gale crater, Mars. *Science*, *350*(6257). https://doi.org/10.1126/science.aac7575

Grotzinger, J. P., & Milliken, R. E. (2012). *The sedimentary rock record of Mars: Distribution, origins, and global stratigraphy* (Vol. 102, pp. 1–48). SEPM Special Publications. https://doi.org/10.2110/pec.12.102.0001

Grotzinger, J. P., Sumner, D. Y., Kah, L. C., Stack, K., Gupta, S., Edgar, L., et al. (2014). A habitable fluvio-lacustrine environment at Yellowknife Bay, Gale crater Mars. *Science*, *343*(6169). https://doi.org/10.1126/science.1242777

Grundvåg, S.-A., Helland-Hansen, W., Johannessen, E. P., Eggenhuisen, J., Pohl, F., & Spychala, Y. (2023). Deep-water sand transfer by hyperpycnal flows, the Eocene of Spitsbergen, Arctic Norway. *Sedimentology*, *70*(7), 2057–2107. https://doi.org/10.1111/sed.13105

Gupta, S., Bell, J. F., Caravaca, G., Mangold, N., Stack, K., Kanine, O. A., et al. (2023). Fine-scale sedimentary architecture of the upper part of the Jezero western delta front. In *Paper presented at the 54th lunar and planetary science conference 2023*. Retrieved from https://www.hou.usra.edu/meetings/lpsc2023/pdf/2953.pdf

Hamran, S.-E. (2021). Mars 2020 RIMFAX bundle, calibrated data collection [Dataset]. NASA Planetary Data System. https://doi.org/10.17189/1522644

Hamran, S.-E., Paige, D. A., Amundsen, H. E. F., Berger, T., Brovoll, S., Carter, L., et al. (2020). Radar imager for Mars' subsurface experiment–RIMFAX. *Space Science Reviews*, *216*(128), 128. https://doi.org/10.1007/s11214-020-00740-4

Harrel, J. (1984). A visual comparator for degree of sorting in thin and plane sections. *Journal of Sedimentary Research*, *54*(2), 646–650. https://doi.org/10.2110/jsr.54.646

Hays, L. E., Graham, H. V., Des Marais, D. J., Hausrath, E. M., Horgan, B., McCollom, T. M., et al. (2017). Biosignature preservation and detection in Mars analog environments. *Astrobiology*, *17*(4), 363–400. https://doi.org/10.1089/ast.2016.1627

Homann, M., Heubeck, C., Airo, A., & Tice, M. (2015). Morphological adaptations of 3.22 Ga-old tufted microbial mats to Archean coastal habitats (Moodies Group, Barberton Greenstone Belt, South Africa). *Precambrian Research*, *266*, 47–64. https://doi.org/10.1016/j.precamres.2015.04.018

Horgan, B., Duflot, L., Garczynski, B., Gupta, S., Johnson, J. R., & Kathir, B. (2023). Provenance of sediments in the Jezero delta from Perseverance rover and orbital observations. In *Paper presented at the 54th lunar and planetary science conference 2023*. Retrieved from https://www.hou.usra.edu/meetings/lpsc2023/pdf/3022.pdf

Horgan, B., Udry, A., Rice, M., Alwmark, A., Amundsen, H. E. F., Bell, J. F., III., et al. (2023). Mineralogy, morphology, and emplacement history of the Maaz formation on the Jezero crater floor from orbital and rover observations. *Journal of Geophysical Research: Planets*, *128*(8), e2022JE007612. https://doi.org/10.1029/2022JE007612

Hurowitz, J. A., Tice, M. M., Allwood, A. A., Cable, M. L., Bosak, T., Broz, A., et al. (2023). The petrogenetic history of the Jezero crater delta front from microscale observations by the Mars 2020 PIXL instrument. In *Paper presented at the 54th lunar and planetary science conference 2023*. Retrieved from https://www.hou.usra.edu/meetings/lpsc2023/pdf/2301.pdf

Ives, L., Stack, K., Gupta, S., Grotzinger, J. P., Lamb, M. P., Barnes, et al. (2023). Reassessing the sedimentary depositional origin of the Jezero crater western fan's curvilinear unit: Reconciling orbital and rover observations. In *Paper presented at the 2023 annual meeting of the American geophysical union*.

Jackson, C. A.-L., & Johnson, H. D. (2009). Sustained turbidity currents and their interaction with debrite-related topography; Labuan Island, offshore NW Borneo, Malaysia. *Sedimentary Geology*, *219*(1–4), 77–96. https://doi.org/10.1016/j.sedgeo.2009.04.008

Jodhukupar, J., Bell, J. F., III., & Gupta, S. (2023). Characterizing the northern fan deposits in Jezero crater, Mars. In *Paper presented at the 54th lunar and planetary science conference 2023*. Retrieved from https://www.hou.usra.edu/meetings/lpsc2023/pdf/2977.pdf

Kneller, B. C., & Branney, M. J. (1995). Sustained high-density turbidity currents and the deposition of thick massive sands. *Sedimentology*, *42*(4), 607–616. https://doi.org/10.1111/j.1365-3091.1995.tb00395.x

Kronyak, R. E., Kah, L. C., Edgett, K. S., VanBommel, S. J., Thompson, L. M., Wiens, R. C., et al. (2019). Mineral-filled fractures as indicators of multigenerational fluid flow in the Pahrump Hills member of the Murray formation, Gale crater, Mars. *Earth and Space Science*, *6*(2), 238–265. https://doi.org/10.1029/2018EA000482

Lamb, M. P., Grotzinger, J., Southard, J. B., & Tosca, N. (2012). Were ripples on Mars formed by flowing brines? In J. Grotzinger, & R. Milliken (Eds.), *Sedimentary geology on Mars* (Vol. 102, pp. 139–150). SEPM Special Publication. https://doi.org/10.2110/pec.12.102.0139

Lamb, M. P., Hickson, T., Marr, J. G., Sheets, B., Paola, C., & Parker, G. (2004). Surging versus continuous turbidity currents: Flow dynamics and deposits in an experimental intraslope basin. *Journal of Sedimentary Research*, *74*(1), 148–155. https://doi.org/10.1306/062103740148

Lamb, M. P., McElroy, B., Kopriva, B., Shaw, J., & Mohrig, D. (2010). Linking river-flood dynamics to hyperpycnal-plume deposits: Experiments, theory, and geological implications. *Geological Society of America Bulletin*, *122*(9/10), 1389–1400. https://doi.org/10.1130/B30125.1

Lanza, N., Gasda, P., Ollila, A., Chide, B., Garzczynski, B., Johnson, J., et al. (2023). A varnish-like high-manganese rock coating in Jezero crater, Mars. In *Paper presented at the EGU general assembly 2023*. https://doi.org/10.5194/egusphere-egu23-10757

Lapôtre, M. G. A., Bishop, J. L., Ielpi, A., Lowe, D. R., Siebach, K. L., Sleep, N. H., & Tikoo, S. M. (2022). Mars as a time machine to Precambrian Earth. *Journal of the Geological Society*, *179*(5). https://doi.org/10.1144/jgs2022-047

Lapôtre, M. G. A., & Ielpi, A. (2020). The pace of fluvial meanders on Mars and implications for the western delta deposits of Jezero crater. *AGU Advances*, *1*(2), e2019AV000141. https://doi.org/10.1029/2019AV000141

Lazar, O. R., Bohacs, K., Macquaker, J., Schieber, J., & Demko, T. (2015). Capturing key attributes of fine-grained sedimentary rocks in outcrops, cores, and thin sections: Nomenclature and description guidelines. *Journal of Sedimentary Research*, *85*(3), 230–246. https://doi.org/10.2110/jsr.2015.11

Le Deit, L., Hauber, E., Fueten, F., Pondrelli, M., Pio Rossi, A., & Jaumann, R. (2013). Sequence of infilling events in Gale crater, Mars: Results from morphology, stratigraphy, and mineralogy. *Journal of Geophysical Research: Planets*, *118*(12), 2439–2473. https://doi.org/10.1002/2012JE004322

Liu, Y., Tice, M. M., Schmidt, M. E., Treiman, A. H., Kizovski, T. V., Hurowitz, J. A., et al. (2021). An olivine cumulate outcrop on the floor of Jezero crater, Mars. *Science*, *377*(6614), 1513–1519. https://doi.org/10.1126/science.abo2756

Lopez-Reyes, G., Nachon, M., Veneranda, M., Beyssac, O., Madariaga, J. M., Manrique, J. A., et al. (2023). Anhydrite detections by Raman spectroscopy with Supercam at the Jezero Delta, Mars. In *Paper presented at the 54th lunar and planetary science conference*. Retrieved from https://www.hou.usra.edu/meetings/lpsc2023/pdf/1721.pdf

Maki, J. N., Gruel, D., McKinney, C., Ravine, M. A., Morales, M., Lee, D., et al. (2020). The Mars 2020 engineering cameras and microphone on the Perseverance rover: A next-generation imaging system for Mars exploration. *Space Science Reviews*, *216*(8), 137. https://doi.org/10.1007/s11214-020-00765-9

Malin, M. C., & Edgett, K. S. (2000). Sedimentary rocks of early Mars. *Science*, *290*(5498), 1927–1937. https://doi.org/10.1126/science.290.5498.1927

Mandon, L., Ehlmann, B. L., Wiens, R. C., Horgan, B., Garczynski, B. J., Johnson, J. R., et al. (2023). Variable past-redox conditions at Jezero crater, Mars. In *Paper presented at the 54th lunar and planetary science conference*.

Mangold, N., Dromart, G., Ansan, V., Salese, F., Kleinhans, M. G., Massé, M., et al. (2020). Fluvial regimes, morphometry, and age of Jezero crater paleolake inlet valleys and their exobiological significance for the 2020 rover mission landing site. *Astrobiology*, *20*(8), 994–1013. https://doi.org/10.1089/ast.2019.2132

Mangold, N., Gupta, S., Caravaca, G., Dromart, G., Gasnault, O., Le Mouélic, S., et al. (2023). From lake deposits to fluvial floods at the eastern delta front of Jezero crater, Mars. In *Paper presented at the 54th lunar and planetary science conference 2023*. Retrieved from https://www.hou.usra.edu/meetings/lpsc2023/pdf/2140.pdf

Mangold, N., Gupta, S., Gasnault, O., Dromart, G., Tarnas, J. D., Sholes, S. F., et al. (2021). Perseverance rover reveals an ancient delta-lake system and flood deposits at Jezero crater, Mars. *Science*, *374*(6568), 711–717. https://doi.org/10.1126/science.abl4051

Marconato, A., de Almeida, R. P., Janikian, L., Carrera, S. C., Turra, B. B., dos Santos, M. G. M., et al. (2022). Floodplain record of channelized and unconfined flow in a pre-vegetation setting in the Early Cambrian, Southern Brazil. *Journal of South American Earth Sciences*, *114*, 103707. https://doi.org/10.1016/j.jsames.2021.103707

Maurice, S., Wiens, R. C., Bernardi, P., Caïs, P., Robinson, S., Nelson, T., et al. (2021). The SuperCam instrument suite on the Mars 2020 rover: Science objectives and mast-unit description. *Space Science Reviews*, *217*(47), 47. https://doi.org/10.1007/s11214-021-00807-w

McEwen, A. S., Eliason, E. M., Bergstrom, J. W., Bridges, N. T., Hansen, C. J., Alan Delamere, W., et al. (2007). Mars reconnaissance orbiter's high resolution imaging science experiment (HiRISE). https://doi.org/10.1029/2005JE002605

McLennan, S. M., Grotzinger, J. P., Hurowitz, J. A., & Tosca, N. J. (2019). The sedimentary cycle on early Mars. *Annual Review of Earth and Planetary Sciences*, *47*(1), 91–118. https://doi.org/10.1146/annurev-earth-053018-060332

McMahon, S., Bosak, T., Grotzinger, J. P., Milliken, R. E., Summons, R. E., Daye, M., et al. (2018). A field guide to finding fossils on Mars. *Journal of Geophysical Research- Planets*, *123*(5), 1012–1040. https://doi.org/10.1029/2017JE005478

Mustard, J. F., Adler, M., Allwood, A., Bass, D. S., Beaty, D. W., Bell, J. F., III., et al. (2013). Report of the Mars 2020 science definition team (p. 154). posted July 2013 by the Mars Exploration Program Analysis Group (MEPAG) at Retrieved from http://mepag.jpl.nasa.gov/reports/MEP/Mars_2020_SDT_Report_Final.pdf

Mustard, J. F., Murchie, S. L., Pelkey, S. M., Ehlmann, B. L., Milliken, R. E., Grant, J. A., et al. (2008). Hydrated silicate minerals on Mars observed by the Mars Reconnaissance Orbiter CRISM instrument. *Nature*, *454*(7202), 305–309. https://doi.org/10.1038/nature07097

Nachon, M., Lopez-Reyes, G., Meslin, P.-Y., Ollila, A., Mandon, L., Clavé, E., et al. (2023). Light-toned veins and material in Jezero crater, Mars, as seen in-situ via NASA'S Perseverance rover (Mars 2020 mission): Stratigraphic distribution and compositional results from the SuperCam instrument. In *Paper presented at the 54th lunar and planetary science conference 2023*. Retrieved from https://www.hou.usra.edu/meetings/lpsc2023/pdf/2673.pdf

Natalicchio, M., Birgel, D., Dela Pierre, F., Ziegenbalg, S., Hoffmann-Sell, L., Gier, S., & Peckmann, J. (2021). Messinian bottom-grown selenitic gypsum: An archive of microbial life. *Geobiology*, *20*(1), 3–21. https://doi.org/10.1111/gbi.12464

Nichols, G. (2007). Fluvial systems in desiccating endorheic basins. In G. Nichols, E. Williams, & C. Paola (Eds.), *Sedimentary processes, environments and basins: A tribute to peter friend* (pp. 569–589). https://doi.org/10.1002/9781444304411.ch23

Noffke, N. (2010). *Geobiology: Microbial mats in sandy deposits from the Archean Era to today*. Springer Berlin. https://doi.org/10.1007/978-3-642-12772-4

North, C. P., & Davidson, S. K. (2012). Unconfined alluvial flow processes: Recognition and interpretation of their deposits, and the significance for palaeogeographic reconstruction. *Earth-Science Reviews*, *111*(1–2), 199–223. https://doi.org/10.1016/j.earscirev.2011.11.008

Onstott, T. C., Ehlmann, B. L., Sapers, H., Coleman, M., Ivarsson, M., Marlow, J. J., et al. (2019). Paleo-rock-hosted life on Earth and the search on Mars: A review and strategy for exploration. *Astrobiology*, *19*(10), 1230–1262. https://doi.org/10.1089/ast.2018.1960

Paige, D. A., Hamran, S.-E., Amundsen, H. E. F., Berger, T., Russell, P., Kakria, R., et al. (2024). Ground penetrating radar observations of the contact between the western delta and the crater floor of Jezero crater, Mars. *Science Advances*, *10*, eadi8339. https://doi.org/10.1126/sciadv.adi8339

Palucis, M. C., Dietrich, W. E., Williams, R. M. E., Hayes, A. G., Parker, T., Sumner, D. Y., et al. (2016). Sequence and relative timing of large lakes in Gale crater (Mars) after the formation of Mount Sharp. *Journal of Geophysical Research: Planets*, *121*(3), 472–496. https://doi.org/10.1002/2015JE004905

Plink-Björklund, P., & Steel, R. J. (2004). Initiation of turbidity currents: Outcrop evidence for Eocene hyperpycnal flow turbidites. *Sedimentary Geology*, *165*(1–2), 29–52. https://doi.org/10.1016/j.sedgeo.2003.10.013

Poulet, F., Bibring, J.-P., Mustard, J. F., Gendrin, A., Mangold, N., Langevin, Y., et al. (2005). Phyllosiciliates on Mars and implications for early Martian climate. *Nature*, *438*(7068), 623–627. https://doi.org/10.1038/nature04274

Powers, M. C. (1953). A new roundness scale for sedimentary particles. *Journal of Sedimentary Petrology*, *23*(2), 117–119. https://doi.org/10.1306/D4269567-2B26-11D7-8648000102C1865D

Prieto-Barajas, C. M., Valencia-Cantero, E., & Santoyo, G. (2018). Microbial mat ecosystems: Structure types, functional diversity, and biotechnological application. *Electronic Journal of Biotechnology*, *31*, 48–56. https://doi.org/10.1016/j.ejbt.2017.11.001

Roppel, R. D., Abbey, W. J., Asher, S. A., Bhartia, R., Bykov, S. V., Conrad, P., et al. (2023). Investigation of mineralogies during the delta front campaign by SHERLOC. In *Paper presented at the 54th lunar and planetary science conference 2023*. Retrieved from https://www.hou.usra.edu/meetings/lpsc2023/pdf/2761.pdf

Salese, F., Kleinhans, M. G., Mangold, N., Ansan, V., McMahon, W., De Haas, T., & Dromart, G. (2020). Estimated minimum life span of the Jezero fluvial delta (Mars). *Astrobiology*, *20*(8), 977–993. https://doi.org/10.1089/ast.2020.2228

Schneider, C. A., Rasband, W., & Eliceiri, K. W. (2012). NIH image to ImageJ: 25 years of image analysis. *Nature Methods*, *9*(7), 671–675. https://doi.org/10.1038/nmeth.2089

Schon, S. C., Head, J. W., & Fassett, C. I. (2012). An overfilled lacustrine system and progradational delta in Jezero crater, Mars: Implications for Noachian climate. *Planetary and Space Science*, *67*(1), 28–45. https://doi.org/10.1016/j.pss.2012.02.003

Simon, J. I., Hickman-Lewis, K., Cohen, B. A., Mayhew, L. E., Shuster, D. L., Debaille, W., et al. (2023). Samples collected from the floor of Jezero crater with the Mars 2020 Perseverance rover. *Journal of Geophysical Research- Planets*, *128*(6), e2022JE007474. https://doi.org/10.1029/2022JE007474

Southard, J. B., & Boguchwal, L. A. (2023). Bed configuration in steady unidirectional water flows; Part 2, Synthesis of flume data. *Journal of Sedimentary Research*, *60*(5), 658–679. https://doi.org/10.1306/212F9241-2B24-11D7-86448000102C1865D

Squyres, S. W., Grotzinger, J. P., Arvidson, R. E., Bell, J. F., III., Calvin, W., Christensen, P. R., et al. (2004). In situ evidence for an ancient aqueous environment at Meridiani Planum, Mars. *Science*, *306*(5702), 1709–1714. https://doi.org/10.1126/science.1104559

Stack, K. M., Williams, N. R., Calef, F., III., Sun, V. Z., Williford, K. H., Farley, K. A., et al. (2020). Photogeologic map of the Perseverance rover field site in Jezero crater constructed by the Mars 2020 science team. *Space Science Reviews*, *216*(127), 127. https://doi.org/10.1007/s11214-020-00739-x

Stow, D., & Smillie, Z. (2020). Distinguishing between deep-water sediment facies: Turbidites, contourites and hemipelagites. *Geosciences*, *10*(2), 68. https://doi.org/10.3390/geosciences10020068

Sun, V. Z., Hand, K. P., Stack, K. M., Farley, K. A., Simon, J. I., Newman, C., et al. (2023). Overview and results from the Mars 2020 Perseverance rover's first science campaign on the Jezero crater floor. *Journal of Geophysical Research: Planets*, *128*(6), e2022JE007613. https://doi.org/10.1029/2022JE007613

Sun, V. Z., Stack, K. M., Kah, L. C., Thompson, L., Fischer, W., Williams, A. J., et al. (2019). Late-stage diagenetic concretions in the Murray formation, Gale crater, Mars. *Icarus*, *321*, 866–890. https://doi.org/10.1016/j.icarus.2018.12.030

Talling, P. J., Masson, D. G., Sumner, E. J., & Malgesini, G. (2012). Subaqueous sediment density flows: Depositional processes and deposit types. *Sedimentology*, *59*(7), 1937–2003. https://doi.org/10.1111/j.1365-3091.2012.01353.x

Thomson, B. J., Bridges, N. T., Milliken, R., Baldridge, A., Hook, S. J., Crowley, J. K., et al. (2011). Constraints on the origin and evolution of the layered mound in Gale crater, Mars using Mars Reconnaissance Orbiter data. *Icraus*, *214*(2), 413–432. https://doi.org/10.1016/j.icarus.2011.05.002

Tooth, S. (1999). Downstream changes in floodplain character on the northern plains of arid Central Australia. In N. D. Smith, & J. Rogers (Eds.), *Fluvial sedimentology VI*. https://doi.org/10.1002/9781444304213.ch8

Udry, A., Ostwald, A., Sautter, V., Cousin, A., Beyssac, O., Forni, O., et al. (2023). A Mars 2020 Perseverance SuperCam perspective on the igneous nature of the Máaz formation at Jezero crater an dLink with Séítah, Mars. *Journal of Geophysical Research: Planets*, *128*(7), e2022JE007440. https://doi.org/10.1029/2022/JE007440

van Loon, A. J. (2006). Deformation of a modern alluvial plain. *Geomorphology*, *78*(3–4), 351–358. https://doi.org/10.1016/j.geomorph.2006.02.004

van Loon, A. J. (2009). Soft-sediment deformation structures in siliciclastic sediments: An overview. *Geologos*, *15*(1), 3–55.

Vasavada, A. R. (2022). Mission overview and scientific contributions from the Mars science laboratory curiosity rover after eight years of surface operations. *Space Science Reviews*, *218*(3), 14. https://doi.org/10.1007/s11214-022-00882-7

Vasavada, A. R., Grotzinger, J. P., Arvidson, R. E., Calef, F. J., Crisp, J. A., Gupta, S., et al. (2014). Overview of the Mars science laboratory mission: Bradbury landing to Yellowknife Bay and beyond. *Journal of Geophysical Research: Planets*, *119*(6), 1134–1161. https://doi.org/10.1002/2014JE004622

Ventra, D., & Nicholas, G. J. (2014). Autogenic dynamics of alluvial fans in endorheic basins: Outcrop examples and stratigraphic significance. *Sedimentology*, *61*(3), 767–791. https://doi.org/10.1111/sed.12077

Weitz, C. M., Sullivan, R. J., Lapotre, M. G. A., Rowland, S. K., Grant, J. A., Baker, M., & Yingst, R. A. (2018). Sand grain sizes and shapes in eolian bedforms at Gale crater, Mars. *Geophysical Research Letters*, *45*(18), 9471–9479. https://doi.org/10.1029/2018GL078972

Wentworth, C. K. (1922). A scale of grade and class terms for clastic sediments. *The Journal of Geology*, *30*(5), 377–392. https://doi.org/10.1086/622910

Werner, S. C. (2008). The early Martian evolution–Constraints from basin formation ages. *Icarus*, *195*(1), 45–60. https://doi.org/10.1016/j.icarus.2007.12.008

Wiens, R. C., & Maurice, S. A. (2021). Mars 2020 SuperCam bundle [Dataset]. NASA Planetary Data System. https://doi.org/10.17189/1522646

Wiens, R. C., Udry, A., Beyssac, O., Quantin-Nataf, C., Mangold, M., Cousin, A., et al. (2022). Compositionally and density stratified igneous terrain in Jezero crater, Mars. *Science Advances*, *8*(34). https://doi.org/10.1126/sciadv.abo3399

Williams, R. M. E., Grotzinger, J. P., Dietrich, W. E., Gupta, S., Sumner, D. Y., Wiens, R. C., et al. (2013). Martian fluvial conglomerates at Gale crater. *Science*, *340*, 1068–1072. https://doi.org/10.1126/science.1237317

Yingst, R. A., Edgett, K. S., Kennedy, M. R., Krezoski, G. M., McBride, M. J., Minitti, M. E., et al. (2016). MAHLI on Mars: Lessons learned operating a geoscience camera on a landed payload robotic arm. *Geoscientific Instrumentation, Methods and Data Systems*, *5*(1), 205–217. https://doi.org/10.5194/gi-5-205-2016

Zavala, C. (2020). Hyperpycnal (over density) flows and deposits. *Journal of Palaeogeography*, *9*(17), 17. https://doi.org/10.1186/s42501-020-00065-x